Università degli Studi di Pisa

Facoltà di Scienze Matematiche, Fisiche e Naturali

Corso di Dottorato in Fisica Applicata

XVII ciclo

Tesi di Dottorato

Star formation rate in the solar neighborhood

Candidato

Michele Cignoni

Relatore

Prof. Scilla Degl'Innocenti

Correlatore

Prof. Steven N. Shore

Contents

Summary

The project, described in this thesis, explores new methods to extract information through the use of color-magnitude diagrams (CMDs). In particular, the purpose of this thesis is to provide insight into the star formation rate in the solar neighborhood, analyzing the observations of the Hipparcos satellite.

An original technique of comparison has been devised:

- We employ the Bayesian Richardson-Lucy algorithm to the analysis of the observational errors in the CMDs by converting the CMD into an image (in effect, a CMD is an image, the intensity being the number of stars in a bin of effective temperature and luminosity, affected by a point spread function that originates from the error distributions of the parallaxes and photometry) and using a restoring point spread function derived from the known sources of error. The resulting reconstructions should be the best cleaned data set with which to perform analyses of the star formation rates;

- A synthetic population is built via Monte Carlo extractions of masses and ages, according the assumed initial mass function (IMF) and the star formation rate (SFR). Then, a suitable age-metallicity relation (AMR) gives the metallicity. The extracted synthetic stars are placed in the CMD by interpolations on the adopted stellar evolution tracks. In order to take into account the presence of binary stars, a chosen fraction of stars are assumed as binaries and coupled with a companion star. Once the number of objects populating the artificial CMD equals that of the observed one, the procedure is stopped;

- To evaluate the goodness of the assumed model, we transform the theoretical and the observational CMDs in two dimensional histograms, choosing bin sizes in color

and in absolute magnitude. Once the number of theoretical and observational objects is known in each bin, we implement a norma (a function of the residuals, as a χ^2 or a Poissonian-χ^2) to quantify the differences between the two histograms. Then, one searches for the best set of parameters in the parameter space (through a simplex algorithm). Finally, the confidence limit of the results are evaluated through a bootstrap technique;

- In order to check the sensitivity of the recovered SFR to the different parametrical inputs (IMF, binaries, AMR), the algorithm is tested on artificial "Hipparcos" CMD;

- After fixing the less important parametrical inputs, the analysis is repeated on the real Hipparcos data, previously "cleaned" by the Richardson-Lucy algorithm.

Brief summary of chapters 1 - 6:

Chapter 1 gives an overview on the Galaxy and the solar neighborhood characteristics. Chapter 2 reviews the statistical basis that will be applied in the following chapters. Chapter 3 describes the observational data. In chapter 4 we apply the principles of stellar evolution to explain the Hipparcos CMD morphology. In chapter 5 we examine the qualitative and quantitative application of the Richardson-Lucy algorithm, in order to obtain an Hipparcos CMD cleaned from the observational errors. In chapter 6 we apply the method both to artificial CMDs, showing which parameters are critical for recovering the star formation rate, and to real Hipparcos data. In the last sections we test the recovered star formation against kinematic selection. Finally our results are compared with the ones of recent papers available in literature.

1

Stellar populations

1.1 Large scale structures of the Galaxy

In the past, the objects in the galaxies have been grouped in two distinct broad groups. According to Baade (1944) prescription, “population I” are the objects found in disks of spiral galaxies, usually characterized by a wide variety of ages and a chemical composition almost solar. Typical examples are the bright and hot stars (O-B), clouds, Cepheids variables and clusters stars (as the open clusters of our Galaxy). “Population II” are the stars found in the field or in cluster (like the globular clusters of our Galaxy) in the spheroidal components of the galaxies: old stars, with ages close to the Hubble time, and metal poor compared to the solar composition. Then, with the developments of observational techniques and the updates of the theoretical predictions, the concept of stellar population was enriched of further meanings. It became evident, that, in our Galaxy, instead a clear dichotomy among stars of different populations it is present a gradual variation from the characteristics typical of “population II” to the ones typical of “population I”. It is also known that the evolutionary history of stars in the external galaxies can be different from the one of the Milky Way, thus that the classification in populations as done for our Galaxy could be meaningless for the other galaxies.

Regarding the Milky Way, beyond the mentioned differences in age and chemical composition, observations of the kinematical properties have shown that among high velocity stars (referred to the Sun), there aren't O-B stars and Cepheids, while the majority of RR Lyrae stars are high velocity stars. As the astronomers presently understand, this situation is due to the position in the Galaxy of these stars: the Sun, O-B stars and Cepheids share the rotation in a disk like distribution, following near circular orbits. In contrast, very far from the Galactic plane, in the halo, the only stars are population II objects and they do not share the rotation. These stars, as a reflection of the Sun's motion around the Galactic center, appear very fast.

However, further investigations have shown that the four features just mentioned, metallicity, age, kinematics and spatial position in the Galaxy do not allow always to decide the ownership to a specific population. For example, in the bulge the stars are metal rich, but they belong to population II according to the other three criterions or, a small fraction of RR Lyrae and long period Mira variables have a chemical composition that is intermediate between the two populations, but kinematic and spatial distribution typical of the population I.

In the last 20 years, another observational evidence has faced against the division in two discrete populations: in 1983 Gilmore & Reid found a population with chemical, kinematical and photometric characteristic intermediate between "population I" and "population II". This "thick disk" population seems to be old and to form an extended system around the Galactic plane. These stars partially share the disk rotation and have metallicities of about 25 percent of the solar metallicity.

This scenario destroyed the idea that the "population II", old and metal poor, and the "population I", young and metal rich, are simply steps of the Galactic formation. In other words, a monolithic collapse from a spherical halo, with following chemical enrichment in a disk, could be partially false.

Today, with the increased number of observations, we know that the Galaxy is far from a closed-box system. The role of infalls is essential, as demonstrated e.g. by the Sagittarius dwarf galaxy merger. In this picture, the same population I (disk) was not only formed from gas shed from the halo (see e.g. Tinsley 1975), but it was formed mainly from extra-galactic gas.

Table 1.1: Mean velocities and velocity dispersion of the Galactic disk.

	$\sigma_{\rm U}$	$\sigma_{\rm V}$	$\sigma_{\rm W}$	$< U >$	$< V >$	$< W >$
	———- [km s^{-1}] ———-					
Wielen (1997)	34	21	21			
Dehnen/Binney (1998)	38	25	20	-10	-22	-7
Nordström et al. (2004)	38.8	31	17.7	-9.6	-20.2	-7.6
Allende Prieto et al. (2004)	27.5	15.6	10.6	-10.6	-12.7	-7.4
Fuhrman et al. (2004)	42.6	22.6	24.1	7.7	-18.1	0.7

1.1.1 The disk

The disk stars move around the Galactic center on orbits close to circular orbits. Defining the Local Standard of Rest (LSR) as the point that is instantaneously centered on the solar location and which orbits on a perfectly circular orbit around the Galactic center confined in directions parallel to the galactic plane, the bulk of disk stars show a net rotational lag of about $15 - 20$ km/s behind the LSR.

Table 1.1 lists mean Galactic velocities and dispersions for disk stars, as recovered from different authors (all values are referred to the LSR).

The density distribution is generally modeled as a double exponential, radially from the Galactic center and perpendicular to the plane. Estimates of the radial scale length vary from 2.25 to 4 kpc, while the vertical scale height vary from 50 pc (for the youngest stars) to about 325 pc (see e.g. Siegel et al. 2002).

The age of the disk has been estimated using several methods:

1. From the white dwarf luminosity function: its cutoff gives an estimate of the disk age; the results range from about 8 to about 10 Gyr in dependence of the adopted white dwarf models and observational data (see e.g. Legget et al. 1998, Fontaine et al. 2001, Hansen 2002);

2. By using the color-magnitude diagram of the local subgiants: the lower envelope of the subgiant region gives information on the beginning of the star formation. The maximum age of the field stars in the solar neighborhood is found to be 7.9 ± 0.7

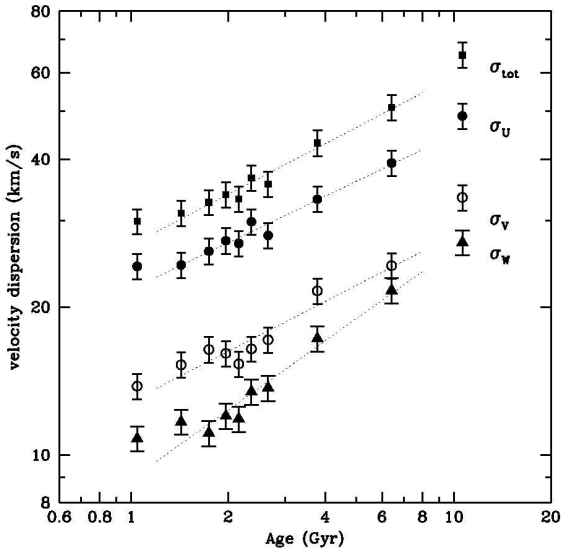

Figure 1.1: Variation of the velocity dispersions with age for solar neighborhood stars (data from Nordström et al. 2004).

Gyr (Sandage et al. 2003);

3. From the analysis of main sequence turn-off stars in the Hipparcos data, the best fit age for the oldest disk stars is about 11 Gyr (Binney et al. 2000);

4. From the analysis of the full color-magnitude diagram of the nearby stars. In particular, Hernandez et al. (2000) finds that the local star formation (over the last 3 Gyr) shows a cyclic pattern with a period of about 0.5 Gyr, while Vergely et al. (2002) and Bertelli & Nasi (2001) recover a local star formation that monotonically decreases with age;

5. From the chromospheric activity, Rocha-Pinto et al. (2000) find evidence for an irregular trend (no periodicity or monotonic trend are recognized) over 14 Gyr.

A striking feature of disk stars is the increase of the velocity dispersions with the age (see figure 1.1). There are two types of explanations for this phenomenon: one hypothesis is that the stars were born with differing kinematic properties and they preserved this status up to now. According to the alternative solution (e.g. Spitzer & Schwarzschild 1951), the velocity dispersion-age relation provides evidence that disk stars were perturbed from their circular orbits by encounters with gas clouds. In this way, the old stars had more

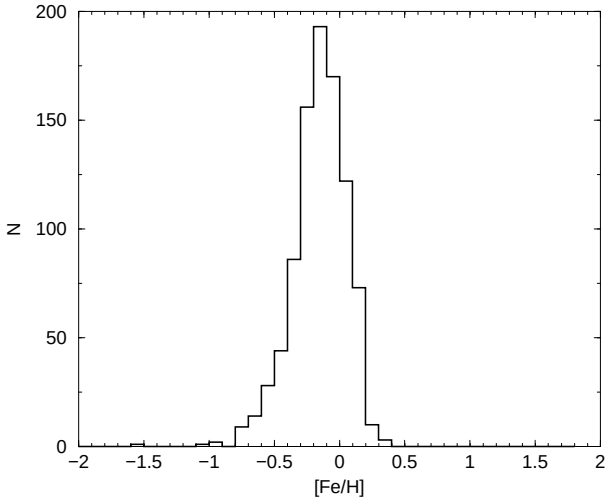

Figure 1.2: $[Fe/H]$ distribution for solar neighborhood stars (data from Nordström et al. 2004).

Table 1.2: As in table 1.1, but for thick disk stars.

	$\sigma_{\rm U}$	$\sigma_{\rm V}$	$\sigma_{\rm W}$	$< U >$	$< V >$	$< W >$
	——— [km s^{-1}] ———					
Soubiran et al. (2003)	63	39	39		-51	
Chiba & Beers (2000)	50	56	34	2	-30	-5
Fuhrmann (2004)	58	41	27	-18	-63	-19

time to increase their velocity dispersion.

The metallicity distribution of disk stars shows a large spread (see figure 1.2). The existence of an age-metallicity relation is still debated.

1.1.2 The thick disk

This population accounts for $2 - 15\,\%$ (Gilmore & Reid 1983 and Chen 1997 claim 2%, Robin et al. 1996 find 6%, Soubiran et al. 2003 find 15%) of the stars in the vicinity of the Sun. The orbital properties of the thick disk stars indicate a scale height of approximately 700 pc to about 1500 pc (Du et al. 2003, Ng et al. 1997, Larsen & Humphreys 2003, Spagna et al. 1996, Reid & Majewski 1993). Table 1.2 sums up the kinematic properties of the thick disk.

Metallicity distributions of the thick disk and disk reveal considerable overlap. How-

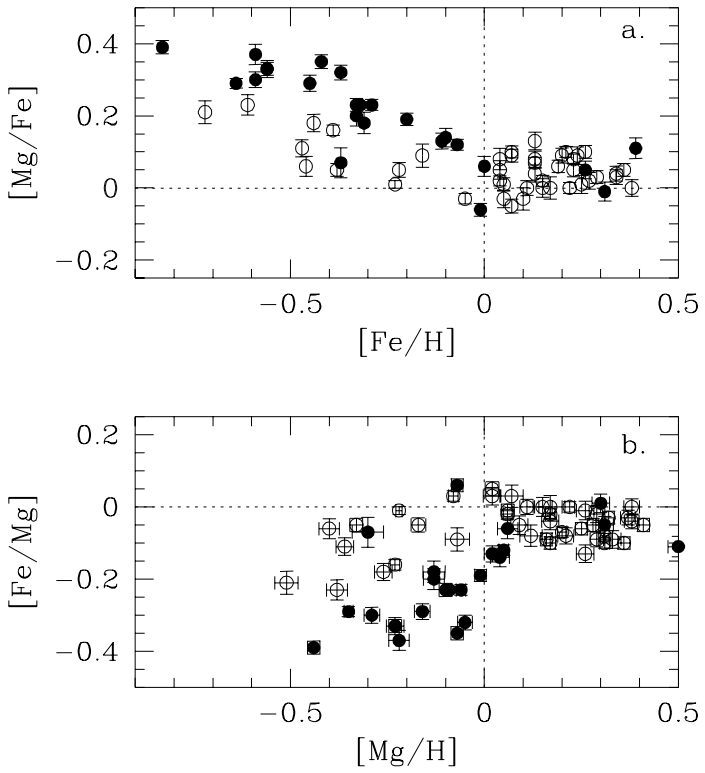

Figure 1.3: Filled symbols are stars whose kinematics fi t the thick disk properties, while open symbols represent disk stars. The high level of $[Mg/Fe]$ at a given $[Fe/H]$ for thick disk stars is a useful tool to distinguish this population by disk stars (Figure taken by Feltzing et al. 2003).

ever, the thick disk seems distinguishable from the disk in kinematics (see table 1.2, it's noteworthy the rotational lag of about $-30 \div -60$ km/s). When a kinematical selection is done, the average $[Fe/H]$ is found about -0.6 (the metallicity of the Galactic cluster 47 Tucanae) and the average age is larger than 10 Gyr (see e.g. Edvardsson et al. 1993, Quillen & Garnett 2001, Liu & Chaboyer 2000)

Moreover, thick disk stars show enhanced levels of $[Mg/Fe]$ (see figure 1.3). Due to the fact that Type Ia supernovae (that involves deflagration of white dwarfs in binary systems, therefore on time scales larger than 1 Gyr) produce mainly Fe-group elements, while Type II supernovae produce significant abundance of α elements (O, Ca, Mg, etc.) as well as some Fe-group and heavier elements, the enhanced level of $[\alpha/Fe]$ would imply a short and old star formation before that Type Ia supernovae could raise the iron abundance.

The origin of the thick disk is debated: according to a family of theoretical models,

the thick disk developed through a dissipative collapse, after the halo and before the disk was completely collapsed. In this scenario, the thick disk formed during the last phases of the collapse, meaning a slow collapse or an high star formation in those phases. However, a slow collapse generates chemical and kinematical gradients that would have let clear tracks. In contrast, an high star formation regime offers a gradient free scenario, but such a mechanism able to enhance the star formation is not still defined. Another problem of this scenario is the difficulty to produce the observed discontinuity in the stellar density between disk and thick disk: if an high star formation phase is postulated, an ad-hoc mechanism is needed to switch off the star formation.

The second family of models deals with the thick disk formation after the gas was completely collapsed in the disk. In this case, the possible physical processes are two: 1) The diffusion of disk stars: probably, the first generation of disk stars had very chaotic motions, as a memory of the gas turbulence. The final equilibrium of these objects could have a thicker distribution. In this case, the thick disk is an extension of the disk. 2) A violent shock due to the merging between our Galaxy and a satellite galaxy. For example, Quinn, Henquist & Fullagart (1993) estimated that a merging with a satellite object with 10% of the disk mass and a 75% of the disk density, can produce a thick disk with 1 kpc of scale height. The discovery of Sagittarius spheroidal galaxy (Ibata, Gilmore & Irwin 1994) suggests that these events are not so rear.

1.1.3 The halo

The halo contribution to the stars within a few hundred parsecs of the Sun accounts for only 0.1 and 0.2 percent. The available evidence on the shape of the stellar halo suggests that it forms a nearly spherical system, whose flattening vary from axial ratio 0.55 (inner regions) to 0.85 (outer halo). The spatial distribution is usually modeled by a power law $\rho(r) \propto r^{-n}$ with exponent n between 2.5 (Robin et al. 2000) to 3.3 (Sommer-Larsen & Zhen 1990), or with a de Vaucouleurs law. Moreover, the outer regions of the halo (at Galactocentric distances greater than 15 kpc) shows stellar streams, remnants of tidally-disrupted satellite galaxies. The table 1.3 shows the halo kinematics: the high dispersions in all three velocity components and the rotational lag implies that this Galactic component shows little net rotation around the Galactic center.

Table 1.3: As in table 1.2 but for halo stars.

	$\sigma_{\rm U}$	$\sigma_{\rm V}$	$\sigma_{\rm W}$	$< U >$	$< V >$	$< W >$
	——— [km s^{-1}] ———					
Chiba & Beers (2000)	141	106	94		-180	
Norris (1986)	131	106	85		-183	

Metallicities are between 1 to 10 percent of the solar one. The peak of the halo metallicity distribution is at about $[Fe/H] \sim -1.6$ (see e.g. Ryan & Norris 1991). The halo is the oldest Galactic structure: age estimations for globular clusters indicate values between about 11 Gyr (Chaboyer et al. 1998) and 13 Gyr (Hansen et al. 2002). The halo stars in the solar neighborhood exhibit high values of the $[\alpha/Fe]$ ratio, suggesting a very rapid star formation.

1.1.4 The bulge

The bulge population lies at the center of the Galaxy, with most of the star within 2-3 kpc of the Galactic center. This Galactic component rotates at roughly 100 Km/s, while the metallicity distribution covers the range $-3 < [Fe/H] < 0.3$ (Searle & Zinn 1978), with a peak at $[Fe/H] \sim -0.3$ (Zoccali et al. 2003). Different studies on the color-magnitude diagrams for bulge stars agree to attribute to it an age larger than 10 Gyr (Feltzing & Gilmore 2000). The enhanced $[\alpha/Fe]$ ratio suggests a rapid star formation. The origin of this structure is debated: one hypothesis indicate the bulge as the result of a merging with a massive satellite; on the other side, an alternative scenario involves an instability at the disk formation epoch (see e.g. Raha et al. 1991).

1.2 The disk luminosity function

A usual way to infer the history of a Galactic population is the analysis of its luminosity function (LF), that is the luminosity distribution of stars. There are two main methods to obtain the LF for a population: the former requires high-quality trigonometric parallax measurements and it is confined to the solar neighborhood; the latter extends to

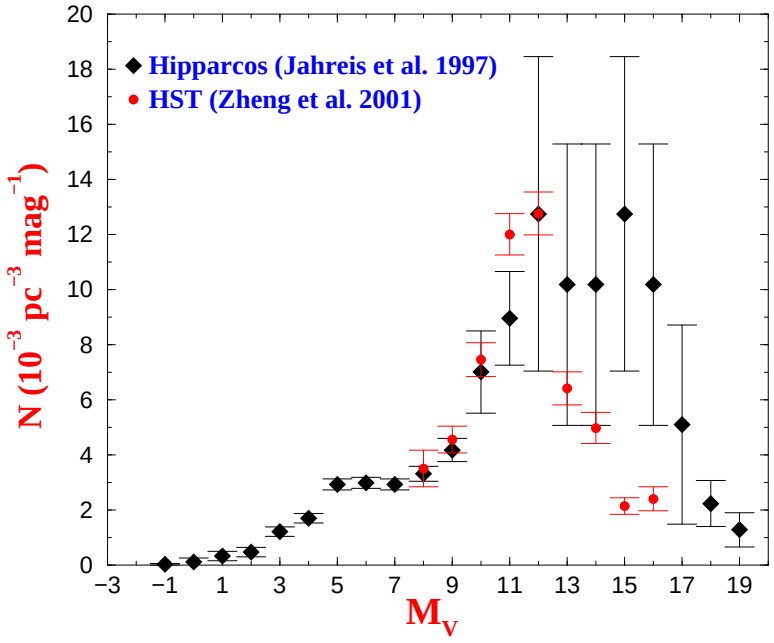

Figure 1.4: Comparison between the luminosity function as obtained with the photometric method (data HST; result taken by Zheng et al. 2001) and with the trigonometric parallax (Hipparcos data; result taken by Jahreiss et al. 1997).

much more larger volume and it is based on the photometric parallax (this method uses the colors of the stars to obtain the spectral type, then, through a color-magnitude diagram calibrated on the nearby stars, a intrinsic luminosity is recovered). Recent disk LFs obtained with these two methods are plotted in figure 1.4: the two slopes agree for magnitudes brighter than $M_V \sim 11$, while, at faint magnitude, the parallax estimated LF shows much more stars than the photometric one.

The trigonometric parallax method (from space) gives accurate estimates of the absolute magnitudes and it allows to resolve the binary stars within $\sim$ 10 pc. However, within this distance, the Hipparcos sample is complete only for $M_V \lesssim 7.3$: beyond this value, the trigonometric luminosity function is deeply incomplete. Another problem of the trigonometric method is the Lutz-Kelker bias (see paragraph 2.5.2), that push the LF towards too faint values.

The photometric parallax method allows to obtain a much more deeper sample and to explore larger volumes. However, it does not resolve the field binaries and it could suffer of systematic errors, because the color - absolute magnitude relation is calibrated on the solar vicinity and it could fail for different places of the Galaxy.

The observed difference between the stars in the sample within 10 pc and in the photometric parallax sample cannot be a local overdensity. A most appealing explanation is that the two methods are looking two different populations: the former is observing mainly disk stars, the latter is observing a large contamination of thick disk stars, but the problem is still open.

1.3 The initial mass function

A basic quantity to study the Galactic formation and evolution is the initial mass function (IMF), that specifies the mass distribution of a newborn stellar population. It is well known that the stars can exist only in a limited range of masses: objects with masses lower than $\approx 0.08\ M_{\odot}$ (the precise value depends on the chemical composition) cannot ignite the hydrogen and their destiny is to cool as brown dwarfs. Regarding the superior limit, the theory is much more uncertain: some calculations (see e.g. Wolfire & Cassinelli 1987) suggest that the formation of stars over $\approx 100\ M_{\odot}$ (the exact result depends on the size distribution of dust grains as well as on the proto-star geometry) should prevented by the radiation pressure on the infalling material.

To obtain information about the local IMF we start from the observations of the local luminosity function. Then, the absolute magnitudes (obtained through distance estimations) are converted in masses by means of a theoretical mass-luminosity relation calibrated for main sequence stars (for giant stars it is not possible to obtain a similar law). In other words, the number of stars in the absolute magnitude (in a given photometric band) interval $M + dM$ to M and in the mass interval m to $m + dm$ is:

$$dN = -\psi\ dM = \phi(m)\, dm \tag{1.1}$$

where $\phi(m)$ is the present day mass function (PDMF), that is how the masses are distributed now, and $\psi(M)$ is the main sequence stellar luminosity function. Rewriting equation 1.1:

$$\psi(M) = -\phi(m)\frac{dm}{dM} \tag{1.2}$$

we obtain that the luminosity function is proportional to the first derivative of the mass-luminosity relation $m(M)$. A thorough understanding of the mass-luminosity relation is

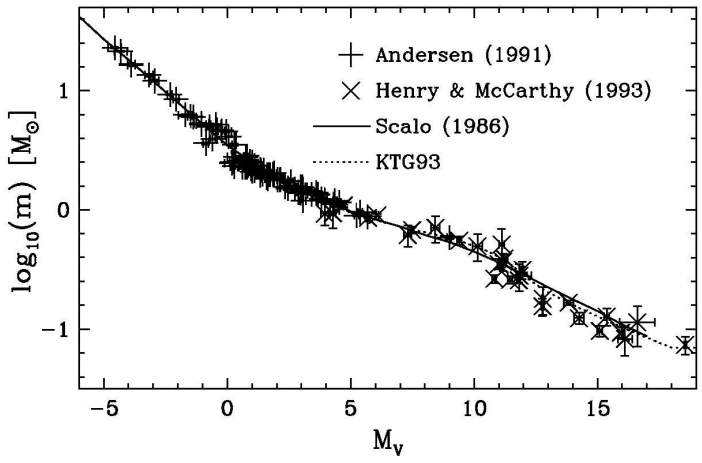

Figure 1.5: The mass-M_V relation: observational data from Henry & McCarthy (1993) and Andersen (1991). The solid curve is the $m(M_V)$ relation by Scalo (1986) and the dotted curve is the semi-empirical relation from Kroupa, Tout & Gilmore (1993). (Figure taken from Kroupa 2001).

thus very important. The observational data plotted in figure 1.5 show that the $\log m(M_V)$ is linear for $m > 2M_\odot$. Then, in the interval $3 < M_V < 8$, the $\log m(M_V)$ becomes less steep: this effect is due to the abundant formation of H^- that increases the mean opacity, reducing the luminosity for intermediate and low-mass stars. In the interval $10 < M_V < 13$ it steepens again because the formation of H_2 in the outers shells of main sequence stars: in this way, the increased molecular weight lead to core contraction and the star is brighter.

From the knowledge of the mass-luminosity relation and the observational luminosity function is possible to recover the PDMF. The next step is to extract the IMF, taking into account the stellar evolution corrections.

Call m the mass of a given star, $\tau(m)$ the time spent by the star in main sequence, T_0 the age of the Galaxy. From stellar evolution we know that an increase of m means a decrease of $\tau(m)$, thus a critical mass m_0 must exist for which $\tau(m_0) = T_0$. As a consequence, all the stars with mass lower than m_0 have a main sequence life exceeding the Galaxy age and these stars are still in main sequence, independently the birth age.

In contrast, if a star has mass greater than m_0, its life is shorter than the Galaxy age: therefore, it is still in main sequence only if it was born between $T_0 - \tau(m)$ and T_0.

In order to extract the IMF from the PDMF it is useful to define a stellar creation

function $C(m,t)$, in a way that $C(m,t)dm$ is the the star number for mass and time unit (see Scalo 1986). Following this notation, the PDMF is:

$$PDMF = \begin{cases} \int_0^{T_0} C(m,t)\,dt & \text{for} \quad \tau(m) \geqslant T_0 \\ \int_{T_0-\tau(m)}^{T_0} C(m,t)\,dt & \text{for} \quad \tau(m) < T_0 \end{cases} \tag{1.3}$$

If we assume that $C(m,t)$ is a separable function of mass and time, that is:

$$C(m,t) = f(m) \cdot G(t) \tag{1.4}$$

where $G(t)$ assumes the meaning of star forming rate and $f(m)$ is the IMF. It is worth to underline that the hypothesis of time independence is only an approximation (the construction of Galactic models with IMF dependent by the chemical composition involves too many parameters and, usually, it is assumed a number of IMF equals to the number of Galactic populations). Factors as the metallicity can influence the process of cloud fragmentation. The stars themself modify the interstellar medium and the final result is highly not-linear. However, from the observational point of view, a systematic variation of the IMF with star-forming conditions has not yet been found (see figure 1.6).
Calling $\overline{G(t)}$ the temporal average of $G(t)$ on the Galaxy age and replacing in 1.3 we obtain:

$$PDMF = \begin{cases} IMF \cdot T_0 \cdot \overline{G} & \text{for} \quad \tau(m) \geqslant T_0 \\ IMF \cdot T_0 \cdot \int_{T_0-\tau(m)}^{T_0} G(t)\,dt & \text{for} \quad \tau(m) < T_0 \end{cases} \tag{1.5}$$

For $\tau(m) \lll T_0$ (in practice masses over $2\ M_\odot$), the second equation can be approximated with:

$$PDMF = IMF \cdot T_0 \cdot G(T_0) \cdot \tau(m) \tag{1.6}$$

Thus, while for low mass stars the IMF identification must follow the preliminary determination of the *average* star formation rate, the IMF for massive stars is highly dependent by the *recent* star formation.

In 1955 Salpeter published the first paper on the IMF and showed that for masses $0.4\ M_\odot \leq m \leq 10\ M_\odot$ it can be approximated by a power law

$$dN = f(m)dm = m^{-\alpha}dm \tag{1.7}$$

with $\alpha = 2.35$. Recent IMF determinations have essentially confirmed a power law for masses above $1\ M_\odot$, with an exponent larger than the Salpeter value for $m > 2 - 3\, M_\odot$. However, the power law parameterization seems not apply at all masses and for $m < 0.5\, M_\odot$ the IMF should be shallower. On pure theoretical basis, there are many arguments that give support for a different mechanism about the formation of stars below or above $1\ M_\odot$.

The tendency of stars to form in groups and in particular, the tendency of more massive stars to develop in larger groups, must play some role to the origin of the upper IMF.

The birth of a massive star through gas accumulation can explain the power low above $1\ M_\odot$. A massive star accumulates gas as long as the birth cloud has this fuel. Only the limited gas amount, the competition with others stars and the interplay with stellar winds can limit the final mass. In fact, there is observational evidence that:

- the stars weren't born uniformally distributed within a cloud, but they coagulate in groups;
- in the star formation regions, the most massive star increases with the total mass of the group;
- often, close to massive stars, small stars are found

Only as an example, we show how a power law IMF can be theoretical justified. Larson et al. 1992 developed a model for the IMF in a hierarchical cloud; if it is hypothized that the most massive star in a stellar system ($m_{\,Max}$) increases with a power $n < 1$ of the total mass of the system ($m_{\,system}$), that is

$$m_{\,Max} \propto m_{system}^{n} \tag{1.8}$$

and also the other stars belong to a hierarchy where the most massive star of a subsystem is linked following the equation 1.8 to the total mass of the subsystem, then each star of mass m will be the most massive of a subsystem of mass $m^{\frac{1}{n}}$. Given that the number of subsystems is inversely proportional to their mass, also the number of stars with mass m will result inversely proportional to the total mass of the subsystem. Finally, we'll have:

$$N_{stars}(m) \propto\ m^{-\frac{1}{n}}. \tag{1.9}$$

On the other side of the mass spectrum (masses below $0.5\ M_{\odot}$), the observed IMF flattening could mean a change in the physical process. For a partial explanation is usually invocated to the concept of Jeans mass, the critical mass for which the thermal energy is equals to the gravitational energy (that is the minimum mass that collapses; for a recent discussion see Herrera et al. 1995). Neglecting magnetic fields, this mass depends by the density and the temperature:

$$m_{Jeans} \propto T^{\frac{3}{2}} \rho^{-\frac{1}{2}}. \tag{1.10}$$

The m_{Jeans} decreases if the density ρ is increased. This implies that a collapsing cloud can fragment in smaller objects, producing a wide mass spectrum.

Adopting the typical values of a molecular cloud, $T = 10\ K$ and $\rho = 10^{-24}\ g/cm^3$, a Jeans mass of $\sim 1\ M_{\odot}$ is obtained (typically the mass where the IMF flattens).

The limits of this argument comes from the assumption of thermodynamic equilibrium of the protostar in the surrounding medium. In reality, molecular clouds are not equilibrium configurations and many random factors enter the game, for example:

- Turbulence;
- Stellar winds from young stars, $\mathrm{H_{II}}$ zones, supernovae;
- Magnetic fields.

Another issue concerns if the IMF is an universal function, independent by the birth place of the stars. It seems obvious to expect different IMFs for zones with different chemical composition (the metallicity changes the way a protostar dissipates the internal energy). The same density should play a role: beyond a critical density the collapsing time for the single fragments becomes larger than the collision time, giving chance for the interaction among collapsing gas masses. However, even if variability of the IMF has often been suggested, a conclusive proof must be still found.

Observations in our Galaxy and in the Large Magellanic Cloud clusters and OB associations have not evidenced systematic differences, but only a large scatter, in particular over $1\ M_{\odot}$ (see figure 1.6, from Kroupa et al. 2001b). These data are well reproduced by the multiple-part power-law IMF shown in table 1.3 (by Kroupa et al. 2001b).

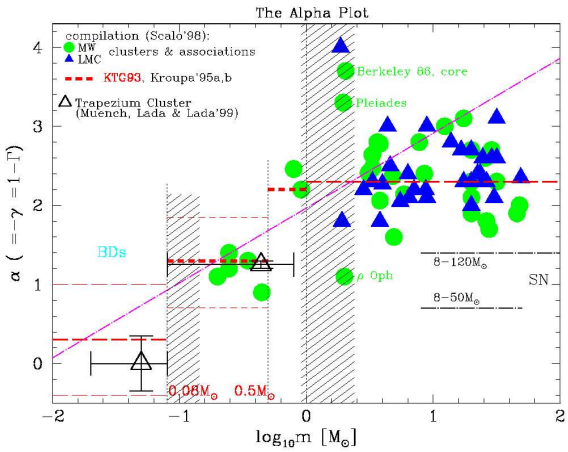

Figure 1.6: IMF exponent α in different mass intervals for our Galaxy, LMC clusters and various OB associations (fi gure from Kroupa et al. 2001b).

Table 1.4: Multiple-part power-law IMF ($m^{-\alpha}$) by Kroupa et al. 2001b.

$\alpha =$	$+0.3 \pm 0.7$	$0.01 \leq m/M_\odot < 0.08$
	$+1.3 \pm 0.5$	$0.08 \leq m/M_\odot < 0.50$
	$+2.3 \pm 0.3$	$0.50 \leq m/M_\odot < 1.00$
	$+2.3 \pm 0.7$	$1.00 \leq m/M_\odot$

1.4 Star formation rate

The present properties of the Galaxy depend on the rate at which gas has been converted into stars during its formation and evolution. Star formation is observed to take place in giant molecular clouds. Thus, the formation of molecular clouds is essential to understand the star formation rate. In particular, we do not observe star forming regions where the stars have more than 10 Myr (Larson 1981). Moreover, star forming regions with more than 5 Myr show signs of disruption, suggesting that clouds forming star clusters are destroyed by them. From the consideration that there are not large numbers of giant clouds without any star formation, the star formation rate should be proportional to the cloud formation rate. If the prerequisite for molecular cloud formation is the formation of large gas complexes by gravitational instability, it is possible to give an estimate of this

time scale (τ). Assuming a disk symmetry, it is found

$$\tau \sim v/\pi G\mu \tag{1.11}$$

where v and μ are the velocity dispersion and the surface density of the cloud. Observations for velocity dispersion of the gas in galaxies suggest a quite constant value between 4 and 10 Km/s (Kennicutt 1990). Thus, the time scale for cloud formation would depend primarily by the surface density.

The star formation rate (SFR) per unit area in a Galactic disk is equal to the gas surface density divided by the timescale for converting the gas into stars; thus in this case it is approximately proportional to μ^2. This relation is close to the well known Schmidt law (Schmidt 1959), except that this SFR depends on the surface density instead of the volume density.

In order to check if a similar SFR leads to a realistic chemical history, it is necessary to implement this gas dependence in a chemical model for our Galaxy. In the simplest model for our Galaxy, the solar neighborhood is treated as a "closed box model" (CBM) in which the initial gas is converted into stars following a given star formation rate (SFR) as a function of gas content. In this paradigm, the usual assumptions are:

1. The IMF is an universal function and it does not vary with time (as natural consequence the gas consumption rate is proportional to the SFR itself);

2. The system has zero initial metallicity;

3. The system is chemically homogeneous (there is no intrinsic scatter in the chemical enrichment of the interstellar medium).

A comparison between the CBM output and the age distribution of nearby stars shows that:

1. The model predicts an excess of metal-poor stars in the solar neighborhood ("G-dwarf" problem);

2. Because the hypothesis of homogeneity, the model predicts a one-to-one relation between age and metallicity, while the observed age-metallicity relation shows a large spread.

If the second puzzle is a proof that gas flows and inhomogeneities are natural features in a real Galaxy, the first undermines the concept of closed box system. Many alternative solution has been proposed to solve the "G-dwarf" problem. The most important are: 1) Gas infall (replenishing of primordial gas), 2) Time dependent IMF; 3) Galactic pre-enrichment". This last one is probably to rule out, because the efficency of chemical enrichment in the halo seems insufficient to reproduce observational values (Hartwick 1976).

Martinelli & Matteucci (2000) and Chiappini, Matteucci & Padoan (2000) explored the effects of an IMF variable in time: this possibility helps to reproduce the G-dwarf metallicity, but it worsens the agreement with other observational constraints (it predicts radial profiles at variance with observations).

A constant IMF with a continuous infall onto the Galactic disk seems the best way to explain the observational constraints, including the "G-dwarf" metallicity distribution. Supporting this scenario, cosmological simulations indicate that primordial gas may continue to rain into galaxies for a long time following their formation. From the observational point of view, there is evidence for an inflow of gas into our Galaxy in the form of high-velocity clouds raining into the Galactic disk (see e.g. Wakker 1991). The different formulations of the SFR as obtained from the analysis of the local field are discussed in paragraph 6.15.

1.5 The solar neighborhood

Stellar evolution is generally tested in star clusters: conglomerates of stars close together in few tenth of parsecs, formed from the same interstellar cloud (and thus with about the same chemical composition) in a time short with respect to the age of the cluster. Star clusters, which due to these characteristics are called "simple" stellar populations, represent a natural laboratory for astronomers. Unfortunately, just these features indicate that star clusters are peculiar loci and they could not reflect either the overall structure of the disk or the global star formation rate.

However, although the clusters that we observe now do not represent a direct test for the global properties of our Galaxy (star formation rate and initial mass distribution), it

is important to notice that the most of the stars was born in clusters and thus, at least originally, belonged to a cluster. In fact, the majority of stars are not formed in isolation, but they develop from large clouds of molecular gas which evolves in stellar clusters and associations. A given cloud produces stars with an efficiency depending on the chemical composition and on the thermodynamic of the cloud, moreover, the star formation process is in general a non linear process, because of the interplay between stars and medium. When a fraction of the original gas ends up creating stars, the residual gas is shot out of the cluster by young massive stars: they heat the gas, causing big portions of it to be blowed away.

At this stage, lost the gas able to bind the system, the stars gradually drift away from each other. Clusters that produce stars with a very high efficency, for example globular clusters in our Galaxy, have a chance to remain gravitationally bound. Another way to avoid the cluster destruction is that the original mass from which the cluster originates is very low (less than $10^4\,M_\odot$; see e.g. Elmegreen 1993): in this case, due to the fact that more massive stars have a lower probability to be formed, there are few O-B stars (the cause for which the cloud breaks apart). The Pleiades association is a typical small mass bound cluster with these features.

From a most general point of view, massive stars are not the only reason for which a cluster should return stars to the medium. Different mechanisms like disk shocking and evaporation (see e.g. Gnedin & Ostriker 1997) cause that also bound clusters can loose stars (on time-scales longer than the destruction by O-B stars). A first evidence of this phenomena is the depletion of low mass stars in globular cluster (see e.g. Elmegreen & Efremov 1997).

When a cluster is destroyed, it returns stars to the Galactic field; if we look at field stars, we are seeing an over-position of many similar events: the solar neighborhood is a “blend of different star clusters”, a mixture of stars with different compositions, ages, masses and distances from us.

Thus the study of field stars compared to the study of star clusters is much difficult but the goal is much more high: there is the possibility to infer the star formation rate, the initial mass function and the chemical composition, not for a simple population, but for the whole Galactic disk.

We could ask why stars were born in distant associations are so close to the Sun. The answer comes from the dynamics of the Galactic disk. If we identify as the solar neighborhood a sphere of 100 pc around the Sun, considering the disk rotation (with a period of ~ 250 Myr at the solar position), we discover that in few Gyr the solar neighborhood experienced many revolution around the Galactic center. This rotation is not itself the cause of the mixing, because the nearby stars co-move with the Sun. There is another feature: the disk has a random motion, over-imposed to the mean rotation, of about 30 Km/s (this velocity dispersion depends on the direction and it increases with time).

Wielen (1977) studied the orbit diffusion by random gravitational encounters with massive clouds on the Galactic plane. The global effect is that, in 5 Gyr, the nearby stars could drift of ~ 200 pc from the Galactic plane and 2 kpc in the radial direction.

This mixing condition falls when we consider stars in high main sequence. For instance, a star of $3\,M_{\odot}$ and solar composition has a life time of about 300 Myr (for a lower metallicity, this time is shorter). This kind of stars maps only the local star formation (they give informations about the nearby OB associations).

If one analyses the color magnitude diagram for nearby stars as a combination of star clusters CMDs, for the low main sequence one should use clusters of whatever age, while for stars progressively brighter one should select only young clusters.

The color magnitude diagram itself, the primary tool of this work, can show very well the composite morphology of the solar neighborhood. Figure 1.7 shows the CMD for a set of clusters and for the Hipparcos stars. It is evident how the stars in the cluster CMDs follow narrow stripes instead of nearby stars that fill up wide regions of the CMD.

1.5.1 An age-metallicity relation for the disk?

The solar neighborhood is the natural place to study the progressive chemical enrichment of the interstellar medium. Stars during their life pollute the medium, so we may expect that the more recently formed stars have an higher metallicity and helium abundance, with respect to the ones formed at an earlier epoch.

In the literature many works approached the problem to derive an age-metallicity relation by a representative local stellar sample. The progressive chemical enrichment with time reflects the star formation rate, the gas infall and outflows, the mixing among dif-

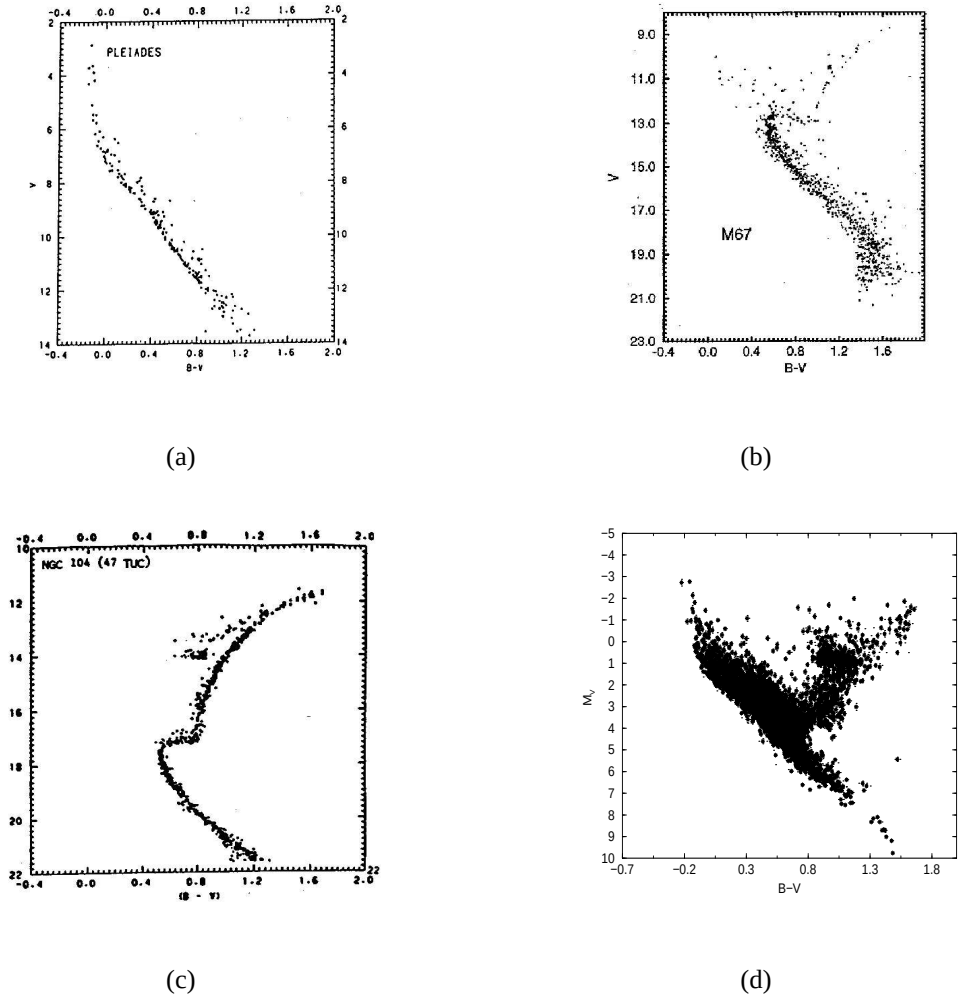

(a) (b)

(c) (d)

Figure 1.7: Color-magnitude diagrams for three stellar clusters of different ages and chemical composition: (a) Pleiades ($Z \sim 0.024$ age ~ 150 Myr), (b) the open cluster M67 ($Z \sim 0.015$, age ~ 3 Gyr), (c) the globular cluster 47 Tucanae ($Z \sim 0.006$, age ~ 10 Gyr). The figure (d) shows the CMD for the Hipparcos field stars which are a mixing of stars of different ages and chemical compositions.

ferent regions of the Galaxy, thus to predict it theoretically it is a difficult task affected by several uncertainties. An observational relation would provide a strong constraint on any model of Galactic chemical evolution. However, recent and old observational studies make in evidence a metallicity spread in the local sample at each given age which is not explained in the framework of standard models of chemical evolution. Is there a real intrinsic scatter in the enrichment history of the ISM?

The studies by Rocha-Pinto et al. (2000) and Twarog (1980) find good correlations between age and metallicity for dwarf stars in the local Galactic disk. In particular Twarog

(1980) found a dispersion of $\sigma_{[Fe/H]} = 0.12\,\mathrm{dex}$, nearly in agreement with the expected uncertainty of the abundance determination.

However, the analysis in Rocha-Pinto et al. (2000) was based on stellar ages derived from the chromospheric emission and more recently, Pace & Pasquini (2004) has shown that the chromospheric emission decreases as the age increases, and for stars older than ~ 4 Gyr it is no more observable.

A larger dispersion in the age-metallicity relation was obtained by Meusinger et al. (1991), ranging from 0.13 dex for stars younger than 2 Gyr to 0.24 dex for the oldest stars. Large abundance variations are also indicated by open clusters with similar ages (Carraro & Chiosi 1994; Piatti et al. 1995).

Moreover several recent investigations appear to indicate that in fact the picture can be even more complicated with metal-rich stars being both young and old (see e.g. Edvardsson et al. 1993 and Feltzing & Gonzalez 2001).

Edvardsson et al. (1993) derived elemental abundances of O, Na, Mg, Al, Si, Ca, Ti, Fe, Ni, Y, Zr, Ba, and Nd for 189 nearby long-lived disk dwarfs by using high resolution, high S/N, spectroscopic data. Individual ages were derived photometrically from fits in the $\log T_{\mathrm{eff}} - \log g$ plane of the isochrones with an estimated uncertainty in the relative ages of about 25 %. The high precision measurements by Edvardsson et.al.1993 greatly improved the AMR, but the resulting AMR clearly indicated a considerable scatter ($\sigma \sim 0.25$ dex) in the metallicities of disk stars formed at any given time, implying that there is only a very weak correlation between age and metallicity. The scatter seems to be too much large to be explained by observational errors ($\sigma \sim 0.05\,\mathrm{dex}$). If the scatter is real, it would cause a serious difficulty for Galactic chemical evolution models.

Very recently, Pont et al. 2004 applied a Bayesian method to compute age estimates to the Edvardsson sample, showing that most of the observed scatter in the AMR is caused by the interplay between the systematic biases affecting the traditional age determination.

From the theoretical point of view, the observed metallicity dispersion has been interpreted by Wielen et al. (1996) as a confirmation of the hypothesis of stellar orbital diffusion, already predicted already by Wielen (1977), while Van den Hoek & de Jong (1997) have argued that diffusion of stellar orbits is probably insufficient to explain the observed abundance scatter. Alternative ideas include the presence of chemical inhomo-

geneities that should able to avoid remixing as long as star formation took place in both the enriched and un-enriched parts, for irregular infall of primordial gas onto the disk (Pilyugin & Edmunds 1996), but the discussion is still open.

However, we point out that most of the studies mentioned above include small numbers of stars, ranging from a few (Feltzing & Gonzalez 2001) to ~ 200 Edvardsson et al. (1993), moreover several samples were selected in order to study a specific type of stars and are therefore not completely representative of the solar neighborhood (see Edvardsson et al. 1993).

The analysis of the AMR has been done also for disk stellar clusters, for example Chen et al. 2003 analyzed 118 open clusters finding no significant evidence for an age-metallicity correlation.

The large database of stellar parallaxes presented in the Hipparcos Catalogue provided the first true possibility to investigate the age-metallicity plot using a larger number of stars. Nordström et al. 2004 selected F and G stars and using Strömgren photometry* determined the effective temperature and $[Fe/H]$ for about 16,000 stars. So, exploiting the absolute magnitude as measured by Hipparcos, the authors estimated the individual ages by isochrones interpolation. One of the weak point of this type of analysis is in the isochrone interpolation, in fact this method gives results progressively worse going closer and closer to main sequence (that means un-evolved stars). This could be a problem when masses above $1.5\,M_{\odot}$ are considered, but it certainly becomes a true limit for low masses when the tracks melt together: small displacements in the CMD correspond to long evolutionary times, so the observational error could arise in a large uncertainty in the age determination.

Another weak point is the possible presence of bias due to the F-G stellar type selection (these long-lived stars are the best tracers of the disk) via cuts in color. The same authors warning about the lack of very young and metal poor stars in diagram of figure 1.8(a): the blue cut could have swept away part of the F-G metal poor stars.

*The uvby and H photometric systems, defined by Strömgren (1966), were studied to measure spectral signatures in early and intermediate type stars. The passband of each filter was chosen to correspond to a particular spectroscopic effect. The u filter relates to the Balmer discontinuity while v was chosen to coincide with that section of the spectrum that shows metal excess. The wavelength of the b and y filters were chosen to correspond to that section of the spectrum almost purely determined by stellar temperature.

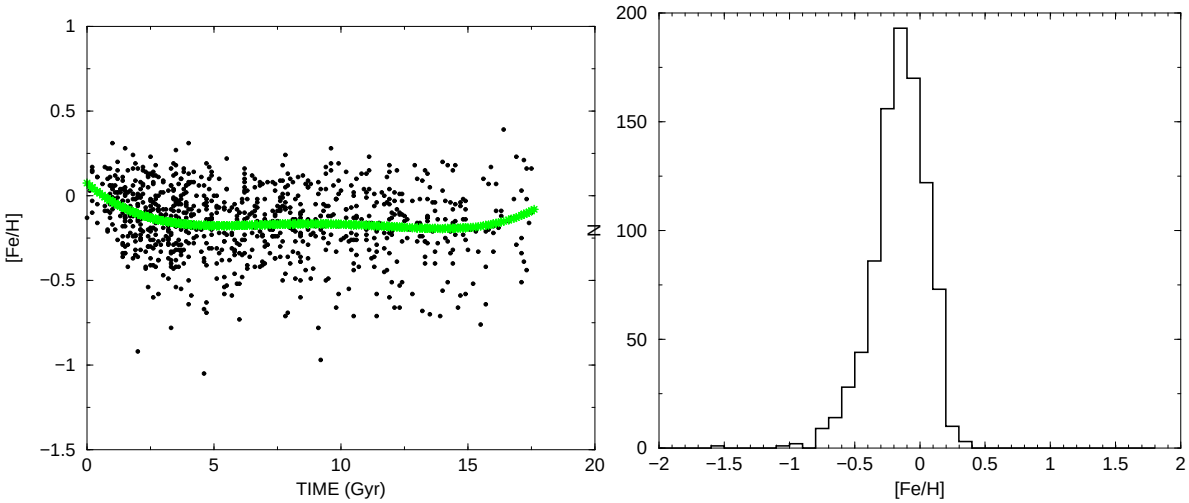

(a) (b)

Figure 1.8: (a) Age-metallicity diagram for single stars (within 40 pc from Sun) with age determination better than 25% (from Nordström et al. 2004). The line is fiducial curve obtained by polynomial interpolation. (b) The distribution of $[Fe/H]$ for the same sample.

The figure 1.8(a) shows the age-metallicity relation found by the authors. A strong scatter is still present: the claimed formal error of ~ 0.1 dex on the $[Fe/H]$ determination cannot account for the observed spread in $[Fe/H]$. It is noteworthy that the mean $[Fe/H]$ value is below solar (figure 1.8(b)).

2

Statistical basis

In this chapter I will review the statistical basis of the Bayesian and the frequentist approach (the formalism is provided in Appendix A), focusing on the application to various astrophysical problems (comparison data-observations, Malmquist and Lutz-Kelker biases, Richardson-Lucy algorithm). In the next chapters, these concepts will be implemented in the Hipparcos data analysis.

2.1 Bayesian framework

Bayes's theorem defines the probability of a set of hypothesis H_J (unobservables quantities) given a set of N observations $E = E_1, E_2, .., E_N$. The fundamental idea of the Bayesian approach is that hypothesis and data are treated in the same way. In order to infer which of the hypothesis has the highest probability of resulting in the observation E, we need to define the joint probability (the probability of both events together) to obtain E given H_J:

$$P(E \cap H_J) = P(E|H_J)P(H_J) = P(H_J|E)P(E) \tag{2.1}$$

where $P(E|H_J)$ is the chance to observe E given the hypothesis H_J, while $P(H_J)$ is the independent probability of H_J.

Rearranging equation 2.1, if a data set E is observed, the probability of the model H_J is

$$P(H_j|E) = \frac{P(E|H_j)P(H_j)}{P(E)}. \tag{2.2}$$

that is the classical formulation of the Bayes's theorem. In case of exclusive and exhaustive hypothesis, the denominator $P(E)$ is simply a normalization factor, therefore:

$$P(H_j|E) \propto P(E|H_j)P(H_j) \tag{2.3}$$

otherwise

$$posterior \propto likelihood \times prior \tag{2.4}$$

In this equation, the *prior* probability is the initial assignment of the probability of any hypothesis being true before experimental evidence is considered (what matters is that the initial beliefs should be based on general arguments about the plausibility of each model and on agreement with other experimental information). It summarizes our initial state of knowledge.

The *likelihood* is the chance of the observation E_i given the hypothesis H_j and it tells us how we must modify our beliefs of the different values H_j (in other words, with a result E_i, what models are avaible and how probable is any one of them). Notice that in this application we think about this as a function of H_i for a fixed observation E_i.

The *posterior* distribution represents our revised belief and is calculated by combining data and prior knowledge (H_j). It tells us what we know about H_j after making the observation (how likely, given the observations, our model explains the data).

2.2 Bayesian vs Frequentist Frameworks

Thus far we have described hypotheses (H_J) without internal parameters, while physical models depend on internal parameters (θ). The Bayesian approach treats unknown parameters as they were random variables: the prior information on the parameters is modified from the data information, giving an updated probability density of parameters (feedback mechanism). The Bayesian view the plausibility of a proposition is produced by combining the data with information from past experience and prior constraints. This was

considered too subjective by the early probability theorists (Fisher, Neyman, Pearson..). In order to remove the subjectivity, the frequentists used the probability with the relative frequency of an outcome in an infinite number of identical experiment. In the frequentist approach, the data are the only source of information. From this point of view, the probability of a hypothesis becomes a meaningless concept because a certain hypothesis is true or false in every repetition of an experiment (the hypothesis is not a random variable); in contrast with data, it does not fluctuate. In other words, they claim it is not possible to talk about the probability of the hypothesis H given the data D, but we should consider the probability of the data given the hypothesis. Therefore, frequentist statistics search for alternative data, while Bayesian inference search for alternative hypotheses: in mathematical terms, frequentists' target is to find an expression for $P(D|H)$, not the Bayesian's $P(H|D)$.

A *non-informative prior* is assigned to the parameters if the investigator does not have information on the parameter or does not want to use the prior information. Since we are assuming ignorance about the values of the unknown parameters, the posterior function in this case will be proportional to the likelihood function and will have the form

$$P(\theta|D) \propto P(D|\theta) \tag{2.5}$$

The set of θ that is most likely is the one maximizing $P(D|\theta)$, a result known as the *maximum likelihood principle* (MLE).

The MLE is the core of the fequentist approach. However, the abolition of the prior is not the main difference from the Bayesian paradigm: the power of the Bayesian approach is not the prior information (that doesn't make sense in the frequentist domain) but the possibility to *update the prior through the data* (feedback).

Both methods search for parameters that give the maximum probability to have the data (one maximizes the likelihood, the other maximizes the posterior probability), but:

- the Bayesian view is an iterative process (the density distribution of the parameters is updated at each iteration, the data is fixed);

- the frequentist approach *must* update the data (new observations or bootstrapped copies of the data) to improve the knowledge on the parameters.

2.3 Maximum Likelihood

The probability density function for a random sample $y_1, y_2, ..., y_N$, governed by an unknown set of parameters, θ, is defined $f(y|\theta)$. This expression is called the likelihood of the sample*. Because θ is generally unknown, it must be estimated from the data. As an estimate of θ we select the value $\tilde{\theta}$ at which the expression for the likelihood of the sample reaches a maximum. This process of finding estimated values of unknown parameters is called maximum likelihood estimation.

2.3.1 General theory

The likelihood function yields a value that is proportional to the likelihood of obtaining the particular data that are actually observed. Assuming independent observations, the individual components of the likelihood function can be multiplied using the general rule for joint probabilities of independent events (see Appendix A):

$$f(y_1, ..., y_N|\theta) = \prod_{i=1}^{N} f(y_i|\theta) = L(\theta|y) \tag{2.6}$$

for the unknown parameter vector, θ, where y indicates the sample dataset (in order to highlight our interest in the parameters and the information about them that is contained in the data, we write the likelihood function as a function of the parameters conditioned on the data).

Instead of maximizing the likelihood function, it is often more convenient to maximize the log-likelihood function, because the logarithm is monotonic. The set of values that maximize L will also maximize $\ln$ L:

$$\ln L = \sum_{i=1}^{N} \ln f(y_i|\theta). \tag{2.7}$$

so that

$$\lim_{\theta \to \tilde{\theta}} \frac{\partial \ln L}{\partial \theta} = 0 \tag{2.8}$$

*Most of the calculations in this section are taken from William Greene book "Econometric Analysis"

This condition is referred to as a first order condition. To ensure that $\ln \mathrm{L}$ is maximized when solving for θ, it must be the case that the slope of $\ln \mathrm{L}$ is decreasing near the MLE. This condition is called the second order condition, given by the expression for the second partial derivative of $\ln \mathrm{L}$ with respect to θ:

$$\frac{\partial^2 \ln L}{\partial \theta^2} < 0 \tag{2.9}$$

As the sample size increases, the likelihood function divided by the sample size tends to stabilise, converging to a constant function. In fact, assuming that the elements of $y = y_1, y_2, ..., y_N$ form a random sample, from equation (2.6) one obtains:

$$\frac{1}{N} \ln L(\theta|y) = \frac{1}{N} \sum_{i=1}^{N} \ln f(y_i|\theta). \tag{2.10}$$

This equation represents a sum of independently and identically distributed random variables, thus, the law of large numbers guarantees that:

$$\lim_{N \to \infty} \frac{1}{N} \ln L(\theta|y) = E[\ln f(y_i|\theta)] \tag{2.11}$$

where $E[\,]$ is the mean operator. In order to demonstrate that $E[\ln L(\theta_0|y)] \geq E[\ln L(\theta|y)]$ (that is, the expected log-likelihood function is maximized by the true parameter value θ_0) we need the first derivative of the log-likelihood function:

$$\frac{d \ln L(\theta|y)}{d\theta} = \frac{1}{L(\theta|y)} \frac{dL(\theta|y)}{d\theta}. \tag{2.12}$$

Calling $A(\theta_0) \leq y \leq B(\theta_0)$ the range of y, for a fixed θ:

$$\int_{A(\theta_0)}^{B(\theta_0)} L(\theta_0|y) dy = 1 \tag{2.13}$$

then, if we differentiate this equation with respect to θ_0, Leibnitz s theorem gives

$$\frac{\partial \int_{A(\theta_0)}^{B(\theta_0)} L(\theta_0|y) dy}{\partial \theta_0} = \int_{A(\theta_0)}^{B(\theta_0)} \frac{\partial L(\theta_0|y)}{\partial \theta_0} dy + L(\theta_0|B(\theta_0)) \frac{\partial B(\theta_0)}{\partial \theta_0} \tag{2.14}$$

$$-L(\theta_0|A(\theta_0)) \frac{\partial A(\theta_0)}{\partial \theta_0} = \tag{2.15}$$

$$= 0 \tag{2.16}$$

In general, it is assumed that the range of the observed random variable y does not depend on the parameters (that is $\partial A(\theta_0)/\partial \theta_0 = \partial B(\theta_0)/\partial \theta_0 = 0$). In this case, the derivative

and the integral commute and the derivative of the expectation is the expectation of the derivative. Thus, from equation 2.12 follows

$$\frac{d}{d\theta}E[\ln L(\theta|y)] = \int_y \left\{ \frac{1}{L(\theta|y)} \frac{dL(\theta|y)}{d\theta} \right\} L(\theta_0|y)dy. \tag{2.17}$$

where $L(\theta_0|y)$ is the probability density of y.

When the right side of the equation 2.17 is evaluated at $\theta = \theta_0$, the expression becomes:

$$\int_y \frac{dL(\theta_0|y)}{d\theta}dy = \frac{d}{d\theta}\int_y L(\theta_0|y)dy = 0. \tag{2.18}$$

where the final equality follows from the fact that the integral is unity (the derivative is zero). Finally

$$\frac{d}{d\theta}E[\ln L(\theta_0|y)] = E\left[\frac{d\ln L(\theta_0|y)}{d\theta}\right] = 0. \tag{2.19}$$

which means that $E[\ln L(\theta|y)]$ is maximized by θ_0. Moreover, from the limit of equation 2.11, we have seen that $\frac{1}{N}\ln L(\theta|y)$ converges to $E[\ln L(\theta|y)]$. Therefore, if the likelihood is continuous and twice differentiable, it follows that the maximizing value of $\ln L(\theta|y)$ (the θ value we called $\tilde{\theta}$ in equation 2.8) must converge to θ_0. In other words, the θ value that maximizes the likelihood is the best estimate of θ_0 (the parameter value that maximizes the likelihood after an infinite number of data).

2.3.2 Example one: Mean and Variance of a Normal Random Variable

Suppose we observe N normally distributed random variables drawn from a population with mean μ and variance σ^2. The likelihood of a single observation is given by

$$L(\mu|y) = \frac{1}{\sqrt{2\pi\sigma^2}}\exp\left(-\frac{(y-\mu)^2}{2\sigma^2}\right) \tag{2.20}$$

Considered as a function of the two parameters, μ and σ this is the likelihood:

$$\ln L(\mu,\sigma^2) = -\frac{N}{2}\ln 2\pi - \frac{N}{2}\ln\sigma^2 - \frac{1}{2}\sum_{i=1}^{N}[\frac{(y_i-\mu)^2}{\sigma^2} \tag{2.21}$$

$$\frac{\partial \ln L}{\partial \mu} = \frac{1}{\sigma^2}\sum_{i=1}^{N}(y_i-\mu) \tag{2.22}$$

$$\frac{\partial \ln L}{\partial \sigma^2} = -\frac{N}{2\sigma^2} + \frac{1}{2\sigma^4}\sum_{i=1}^{N}(y_i-\mu)^2 \tag{2.23}$$

Hence taking the unknown values $\tilde{\mu}$ and $\tilde{\sigma}^2$ for the parameters,

$$\begin{aligned} \frac{\sum (y_i - \tilde{\mu})}{\tilde{\sigma}^2} &= 0 \\ -\frac{N}{2\tilde{\sigma}^2} + \frac{\sum (y_i - \tilde{\mu})^2}{2\tilde{\sigma}^4} &= 0 \end{aligned} \tag{2.24}$$

yields the MLE for the parameters

$$\begin{aligned} \tilde{\mu} &= \sum_{i=1}^{N} y_i/N \\ \tilde{\sigma}^2 &= \frac{1}{N}\sum_{i=1}^{N}(y_i - \tilde{\mu})^2 \end{aligned}$$

which are the sample average and the variance, respectively.

2.3.3 Example two: Poissonian random variable

The probability of observing a particular sample y, assuming that a Poisson distribution with as yet unknown parameter θ generated the data

$$L(\theta|y) = \frac{\theta^y e^{-\theta}}{y!} \tag{2.25}$$

Consider maximizing $\ln L(y|\theta)$ with respect to θ and using Stirling's approximation

$$\ln L(\theta|y) = -N\theta + \ln\theta \sum_{i=1}^{N} y_i - \sum_{i=1}^{N} \ln(y_i!) \tag{2.26}$$

$$\frac{\partial \ln L}{\partial \theta} = -N + \frac{1}{\theta}\sum_{i=1}^{N} y_i \rightarrow \tilde{\theta}_{ML} = \sum_{i=1}^{N} y_i/N \tag{2.27}$$

Taking the second derivative gives

$$\frac{\partial^2 \ln L}{\partial \theta^2} = -\theta^{-2}\sum_{i=1}^{N} y_i < 0 \tag{2.28}$$

Thus there is a local maximum at $\theta = \tilde{\theta}_{ML}$. We note that as $\theta \rightarrow 0$ or $\theta \rightarrow -\infty$, the log-likelihood $L(\theta|y)$ approaches $-\infty$. Thus $\theta = \theta_{ML}$ ia a global maximum.

2.3.4 ML and histograms

In our problem, the color magnitude diagram (CMD) plane is divided in subregions (bins), and the number of stars present in each subregion of both the observed and synthetic CMDs are recorded. If we call n the counts number in the ith bin n_i

$$\overrightarrow{n} = (n_1, n_2, .., n_k) \tag{2.29}$$

What we then want to do is fit the probability distribution to the contents of each bin. The distribution gives us the expected number of events in each bin. The actual number of events, n_i , is then distributed with expectation value m_i for each bin i.

In case of data with Gaussian errors and known uncertainties at each point, the probability that the observation n is drawn from model m is:

$$P(n_i, m_i) = \sqrt{\frac{1}{2\pi\sigma_{mi}^2}} e^{-0.5(n_i - m_i)^2/\sigma_{mi}^2} \tag{2.30}$$

and the log likelihood function:

$$\ln L = -\frac{1}{2}\sum_i \ln \sigma_{mi}^2 - \frac{1}{2}\sum_i \frac{(n_i - m_i)^2}{\sigma_{mi}^2} \tag{2.31}$$

in another form:

$$-2\ln L = \chi^2 + \sum_i \ln \sigma_{mi}^2 \tag{2.32}$$

So, if the observational error distribution is a Gaussian, and the error σ_i doesn't change, minimizing the χ^2 is equivalent to find the most probable model producing the data.
However, none of these assumptions is true in CMDs. The real distribution is Poissonian, where $\sigma_{mi}^2 = m_i$. We can show the maximum likelihood calculation for this case:

$$P(n_i, m_i) = \frac{m_i^{n_i}\, e^{m_i}}{n_i!} \tag{2.33}$$

and the log likelihood function is then:

$$\ln L = \sum_{i=1}^{Nbin} \ln(\frac{m_i^{n_i}\, e^{m_i}}{n_i!}) \tag{2.34}$$

$$= \sum_{i=1}^{Nbin} [n_i \ln m_i - m_i - \ln(n_i!)] \tag{2.35}$$

The equation is also valid for very small intervals or when there are only a small number or no entries in a bin. We can also subtract a constant to the whole equation if we want:

$$= \sum_{i=1}^{Nbin} [n_i \ln n_i - n_i - \ln(n_i!)] \tag{2.36}$$

So the log likelihood is given by:

$$\ln L \quad = \sum_{i=1}^{Nbin} [n_i \ln \frac{m_i}{n_i} - (m_i - n_i)] + constant \tag{2.37}$$

and the Poisson equivalent of the χ^2 is

$$-2 \ln L \quad = 2 \sum_{i=1}^{Nbin} [n_i \ln \frac{n_i}{m_i} - (n_i - m_i)] + constant \tag{2.38}$$

This is very nice form for performing numerical maximization. An examination of this function indicates that it shares many of the features as χ^2, namely it's zero when $n_i = m_i$ and the expectation value and variance are, respectively, 1 and 2, at large values of m_i.

2.4 Richardson-Lucy algorithm

The previous discussion has involved the comparison between theoretical and observational histograms taking account only statistical errors, without considering the incompleteness and observational errors typical of real data. If we grid a color magnitude diagram, building a two dimensional histogram, it could be useful to think of the data as a blurred image where the blurring function consist of the matrix of observational errors and the analysis becomes a deconvolution problem. Thus, although we lose information about the single stars, we gain the opportunity to analyze the sample data in a statistical sense using the knowledge about imaging methods.

A huge number of image deconvolution algorithms exist in the literature. Their popularity derive from their simplicity and ease of use and the sophisticated manner in which they balance a fit to raw data with prior knowledge and expectations. The most promising of these algorithms have a nonlinear nature, and as such they tend to improve the sensitivity and resolution of the reconstructed image in rather subtle ways. The procedure we'll follow here can be seen in the fashion of the Bayesian framework.

If we call the function of interest $f(s)$ the true distribution, and the function we can detect through observations $g(t)$, they are linearly related by a Fredholm integral equation of the first kind,

$$g(t) = \int_a^b ds\, K(t,s) f(s) \tag{2.39}$$

where the integral kernel $K(t,s)$ (the point spread function or psf) reflects the measurement process. In general, $g(t)$ and $f(t)$ represent probability density functions, which implies that they and the kernel $K(t,s)$ obey normalization and non-negativity constraints. $K(t,s)$ is the probability that t' will fall in the interval $(t, t+dt)$ when it is known that $s' = s$.

Often the inversion of the equation 2.39 is mathematically impossible and the problem is called "ill-conditioned". However, even if it can be done, it may be incorrect because of the measurement errors in the data $g(t)$: *there are many possible solution $f(s)$ that, convolved with the psf, satisfy the constraints posed by data*.

The right way to challenge the problem is to understand that the problem is statistical in nature. In this fashion, the new question should be: what's the most likely function $f(s)$ able to satisfy the constraints posed by data and possibly some other constraint "a-priori"?

Richardson (1972) and Lucy (1974, 1994) proposed an iterative inversion algorithm. The starting point is now Bayes theorem for conditional probabilities,

$$P(A|B) \;=\; P(B|A)\frac{P(A)}{P(B)}. \tag{2.40}$$

In order to follow Lucy's notation, we call the conditional probability $P(B|A)$ (or $K(t,s)$) with $P(x|\zeta)$, $P(A)$ (or $f(s)$) with $\psi(\zeta)$, $P(B)$ (or $g(t)$) with $\phi(x)$, $P(A|B)$ with $Q(\zeta|x)$.

The equation 2.39 and the Bayes theorem becomes respectively:

$$\begin{aligned} \phi(x) &= \int \psi(\zeta) P(x|\zeta) d\zeta \\ Q(\zeta|x) &= \psi(\zeta) P(x|\zeta)/\phi(x) \end{aligned} \tag{2.41}$$

The second equation can be re-write using the property of normalization of P:

$$\psi(\zeta) \;= \int \phi(x) Q(\zeta|x) dx \tag{2.42}$$

This equation is in reality only an apparent inversion of the 2.41, in fact the Q function depends implicitly of $\psi(\zeta)$. The advantage to have written the equation in this form is that

it gives the opportunity, together with the equations 2.41, to build an iterative algorithm. Initializing the function ψ with a guess ψ^0, successive ψ^n are computed with the following steps:

$$\phi^n(x) = \int \psi^n(\zeta) P(x|\zeta) d\zeta \tag{2.43}$$

$$Q^n(\zeta|x) = \psi^n(\zeta) P(x|\zeta) / \phi^n(x) \tag{2.44}$$

$$\psi^{n+1}(\zeta) = \int \overline{\phi(x)} Q^n(\zeta|x) dx \tag{2.45}$$

where $\overline{\phi}$ is the measured quantity having sampling errors.

Eliminating Q, these equations can be also expressed in a compact version:

$$\psi_{n+1}(\zeta) = \psi_n(\zeta) \int \frac{\overline{\phi}(x)}{\phi_n(x)} P(x|\zeta) dx \tag{2.46}$$

This iterative equation is called Richardson-Lucy (RL) method and it is a nonlinear iterative deconvolution technique for de-blurring an image when the psf of the imaging system that generated the image is known in advance.

The positivity of the solution, an important constraint for astronomical images, is guaranteed: from (2.46) is evident that if the guess ψ_0 is positive, every ψ_n has the same feature.

Moreover, the algorithm conserves the flux: integrating equation (2.45) with respect to ζ and exploiting the normalization of the probability $Q^n(\zeta|x)$ we find that $\psi^{n+1}(\zeta)$ and the data have the same flux.

Thanks to the psf width, deviations of $\overline{\phi}(x)/\phi_n(x)$ from unity on a length scale large compared to that of $P(x|\zeta)$ will be removed in essentially one iteration. On the other hand, deviations on a small length scale (random deviations) will be averaged out when integrated with $P(x|\zeta)$ and their contribution to change ψ_n will be minimum. Thus, after a few iterations we expect the algorithm will have corrected our initial guess of ψ_0 extracting the coarse information contained in the data while, successive estimates of ψ_n, will make only small changes, until the difference between ϕ_n and $\tilde{\phi}$ will be within the statistical fluctuations. To underline the discrete nature of our data (2-dimensional array of pixels), it's useful to re-write the algorithm in a discrete form. The equation (2.39) becomes a discrete sum of the form

$$\phi_p = \sum_q h_{pq} \psi_q \tag{2.47}$$

where the symbols p, q label two-dimensional position vectors, measured in units of pixel spacing, and h_{pq} is the psf. The unit normalization that we assume for the psf now reduces to the discrete sum formula

$$\sum_p \quad h_{pq} = 1 \tag{2.48}$$

and the RL algorithm is:

$$\psi_p^{(n+1)} \quad = \psi_p^{(n)} \sum_q \left(\frac{h_{qp}\phi_q}{\sum_r h_{qr}\phi_r^{(n)}} \right) \tag{2.49}$$

where the symbol $\phi_p^{(n)}$ denotes the value of the reconstructed map at pixel p at the $n\mathrm{th}$ iteration.

2.5 Astrophysical biases

Absolute magnitudes of stars (M) can be derived from samples of stars defined either by limits in apparent magnitude (m) or by limits in distance (r). Both the selection criteria make the mean absolute magnitude of the sample non-representative ("biased") of the underlying parent distribution. In order to remove the bias there are two alternative solutions: one is applying an a posteriori correction (which assumes generic spatial stellar densities or luminosity functions that may not be realistic), the other is avoiding the bias (for example, in case of Malmquist bias, selecting only bright stars).

2.5.1 Malmquist bias

If we have a sample of stars with an intrinsic spread in absolute magnitude M, and we select only stars with apparent magnitude m, then that sample is likely to be more luminous than it should be. Malmquist (1920) derived the correction to the mean observed M as function of the intrinsic spread in M and the observed distribution of m. In Bayesian framework, the effect can be understood as the difference between the prior distribution of M, and the posterior distribution of M for given m.

For simplicity we assume that the intrinsic distribution of M (luminosity function) is $\phi(M) = \exp\left[-[(M - M_0)^2/2\sigma^2\right]$.

Case of uniform spatial distribution

Let $x = m - M = 5\log(r/10pc)$ denotes the distance modulus. Under the assumption of uniform spatial distribution the distance module has a distribution $f(x) \propto 10^{\,0.6\,x}$. Thus:

$$f(m|M) = f(m-M) \propto 10^{0.6\,(m-M)} = \exp\left[\gamma(m-M)\right] \tag{2.50}$$

where $\gamma = 0.6\ln 10 \sim 1.38$.

According to Bayes theorem:

$$f(M|m) \propto f(m|M)\phi(M) \tag{2.51}$$

So, putting together equation (2.51) and the Gaussian hypothesis for $\phi(M)$, we obtain:

$$\begin{aligned} f(M|m) &\propto \exp\left[\gamma(m-M)\right] \times \exp\left[-[(M-M_0)^2/2\sigma^2\right] \\ &= \exp[\gamma(m-M) - [(M-M_0)^2/2\sigma^2] \\ &= \exp\left[\gamma(m-M_0) + \gamma^2\sigma^2/2\right] \times \exp\left[-(M-M_0+\gamma\sigma^2)^2/2\sigma^2\right] \end{aligned} \tag{2.52}$$

thus $f(M|m) \sim N(M_0 - \gamma\sigma^2, \sigma^2)$ so the mean absolute magnitude of the stars with apparent magnitude m is $\overline{M}_m = M_0 - \gamma\sigma^2$. This result shows that in case of a homogeneously distributed population there bias in the mean absolute magnitude doesn't depend upon m.

Generic spatial distribution

Denoting $a(m)$ the frequency function of m and

$$\int_{-\infty}^{+\infty} a(m)dm = N \tag{2.53}$$

with N the total number of stars, if we assume a general spatial distribution $D(r)$ it follows that

$$a(m) = \omega \int_0^{+\infty} dr\, r^2 D(r)\, \phi(m - 5\log r). \tag{2.54}$$

with ω the solid angle. According to the definition of a mean value we get for the mean absolute magnitude $\overline{M}_m$

$$a(m)\,\overline{M}_m = \omega \int_0^{+\infty} dr\, r^2 D(r)\, M\, \phi(m - 5\log r). \tag{2.55}$$

Differentiating with respect to m we obtain

$$\frac{da(m)}{dm} = -\omega \int_0^{+\infty} dr\, r^2\, D(r)\, \frac{(M - M_0)}{\sigma^2}\, \phi(m - 5\log r) \tag{2.56}$$

from which we get

$$\omega \int_0^{+\infty} dr\, r^2 D(r)\, M\, \phi(m - 5\log r) = M_0\, a(m) - \sigma^2\, \frac{da(m)}{dm} \tag{2.57}$$

and finally

$$\overline{M}_m = M_0 - \sigma^2 \frac{d\ln a(m)}{dm} \tag{2.58}$$

Since the number of stars in a magnitude limited survey usually increases towards fainter apparent magnitude, $da/dm > 0$. Consequently, equation (2.58) implies that the stars in the survey that have any a given apparent magnitude m, will, on the average, have a higher luminosity than the mean luminosity of the population as a whole.

Similar computation gives an expression for the σ_m standard deviation. Differentiating equation (2.56) with respect to m we find

$$\frac{1}{a}\frac{d^2a(m)}{d^2m} = \left\langle \left(\frac{(M - M_0)}{\sigma^2}\right)^2 - \frac{1}{\sigma^2} \right\rangle_m^2 \tag{2.59}$$

thus

$$\begin{aligned}
\frac{1}{\sigma^4}\left\langle (M - M_0)^2 \right\rangle^2 - \frac{1}{\sigma^2} &= \frac{1}{a}\frac{d^2a(m)}{d^2m} && (2.60)\\
&= \frac{d^2\ln a(m)}{d^2m} + \left(\frac{1}{a}\frac{da(m)}{dm}\right)^2 && (2.61)\\
&= \frac{d^2\ln a(m)}{d^2m} + \left(\frac{\langle M\rangle_m - M_0}{\sigma^2}\right)^2 && (2.62)
\end{aligned}$$

so

$$\begin{aligned}
\sigma^4 \frac{d^2\ln a(m)}{d^2m} &= \langle (M - M_0)^2\rangle_m - (\langle M\rangle_m - M_0)^2 - \sigma^2 && (2.63)\\
&= \langle M^2\rangle_m - \langle M\rangle_m^2 - \sigma^2 && (2.64)
\end{aligned}$$

and from equation (2.64) we obtain

$$\sigma_m^2 - \sigma^2 = \sigma^4 \frac{d^2 \ln a(m)}{d^2 m}. \tag{2.65}$$

This means, for example, that if it happens that the population falls with distance, the star count function $a(m)$ will increase with m less rapidly with the result that $\frac{d^2 \ln a(m)}{d^2 m} < 0$ and the equation (2.65) implies that the sample variance will be smaller than population's variance.

2.5.2 Lutz-Kelker bias

In a given solid angle of observation, we'll observe more stars at greater distances than stars close to us. Since it has the same probability that a parallax measurement is larger or smaller than the true distance, and there are more distant stars than close stars, it follows that parallax measurements tend to underestimate distance (Lutz & Kelker (1973) derived a systematic correction as a function of the parallax error (σ/π).). Another point of view to understand the Lutz-Kelker bias is that it is more likely that we find a star slightly farther away with a negative error that brings it closer in to the observed distance, than that we have observed a slightly nearer star with a positive error that pushes it out to the observed distance, because the number of stars increases with distance. In the Bayesian framework we can say that it is more likely a priori that a star of unknown distance is farther away than that it is nearer, which bring us to use of a prior that increases with distance.

Let us assume

1. that the errors measurements of a trigonometric parallax are such that the distribution of observed parallaxes about the true parallax can be expressed by a Gaussian distribution. Thus the distribution of π, the observed parallax, about π_0, the true parallax, is

$$f(\pi|\pi_0) = \frac{1}{\sqrt{2\,pi\,\sigma^2}} \exp\left(-\frac{(\pi_0 - \pi)^2}{2\sigma^2}\right). \tag{2.66}$$

2. that the stars are uniformly distributed in space

We want to know the distribution of true parallaxes about π. Bayes theorem tells us that this distribution is given by

$$f(\pi_0|\pi) \propto f(\pi|\pi_0)f(\pi_0) \tag{2.67}$$

where $f(\pi_0|\pi)$ is the probability that the observational error cause to obtain π_0 when the true parallax is π, while $f(\pi)$ is the a priori distribution of π.

If the stars are uniformly distributed in space, then the number of them at distances between r and $r + dr$ is given by

$$D(r)dr \sim 4\,pi\,r^2 dr \tag{2.68}$$

The number between π_0 and $\pi_0 + d\pi_0$ is

$$D(\pi_0)d\pi_0 \sim \frac{4\,pi\,d\pi_0}{\pi_0^4} \tag{2.69}$$

When we take this into account, we find that the distribution of π_0 about π has this form

$$f(\pi_0|\pi) \propto \frac{1}{\pi_0^4} \exp\left(-\frac{(\pi - \pi_0)^2}{2\sigma^2}\right) \tag{2.70}$$

The important feature of equation (2.70) is the factor $1/\pi_0^4$, which strongly biases the probability $f(\pi_0|\pi)$ that the star has the true parallax π_0 towards small values of π_0. Multiplying for π_0 and using a dimensionless parameter Z defined

$$Z = \frac{\pi_0}{\pi} \tag{2.71}$$

then

$$g(Z) = \frac{1}{Z^4} \exp\left(-\frac{(Z-1)^2}{2\,(\sigma/\pi)^2}\right) \tag{2.72}$$

This represents in dimensionless form the distribution of true parallaxes for a particular value of observed parallax. Figure 2.1 shows a family of curves of this distribution for three values of the parameter σ/π.

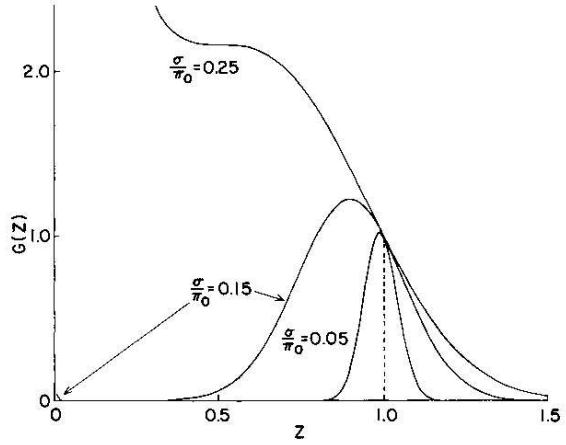

Figure 2.1: Families of curves with parameter σ/π (from Lutz T. E. & Kelker D. H. (1973)).

For accurate parallaxes (σ/π small) there is a small shift of the mean parallax toward a smaller value. The third curve shown is the distribution of true parallaxes for the case $\sigma/\pi = 0.25$. Physically, this result implies that if a parallax measurement has an error greater than 4σ result, we cannot say anything because it is probable to have a close to zero true parallax as a value close the measured value.

3

The solar neighborhood

3.1 Hipparcos mission: an introduction

The trigonometric parallax is the only method to determine directly the distance of a star. The ground based parallax observations allow to achieve high precision parallaxes (sub-milliarcsecond), but they are essentially bound to the presence of a reference star (of well known parallax) within the small field of view allowed by the CCDs (usually within 10-20 arcmin); the inestimability of absolute parallaxes in a small field depends on the possibility that the parallax factor k, proportional to the sine of the angle from the Sun to the star, is nearly constant in the narrow field. The relative displacement of a couple of stars with parallaxes π_1 and π_2 is given by $k \cdot (\pi_1 - \pi_2)$: measuring at different times of the year (thus at different k) one can obtain $\pi_1 - \pi_2$ (but not π_1 and π_2). In conclusion, even if narrow field astrometry allow to measure, with high precision, the parallax of a target star with respect to a reference star, the final measure is dependent by the parallax precision of the reference star. In this sense, all the ground based measures are only "relative" parallaxes.

The ESA Hipparcos satellite was built to fill this gap. The design of this instrument involves two 13-cm diameter telescopes able to focalize two fields of view, separated by $58°$, on the same focal plane. In this way, this instrument was able to measure the

separation between stars with *very different parallax*, giving the possibility, for the first time, to determine absolute parallaxes. The relative displacement must now be written $(k_1 \cdot \pi_1 - k_2 \cdot \pi_2)$ where in general, for stars separated by a large angle (~ 1 rad), k_1 and k_2 are different. Mapping this displacement at different times allow to measure π_1 and π_2 individually, obtaining absolute parallaxes.

The Hipparcos mission provided precise parallaxes and proper motions for about 118,000 stars. The astrometric median accuracy is about 1 mas for parallaxes and 1 mas per yr for proper motions. After Hipparcos, about 5200 stars have a parallax with a measured precision σ_π/π better than 5%, 20853 between 10% and 20%, 49333 have σ_π/π worse than 20%. The final catalogue includes also detailed photometric data, as result of a mean number of 110 observations for each star. The instrument filter (H_P magnitude) covers wave lengths between 350 - 800 nm, with a median precision of 0.0015 mag for $H_P < 9$. The Johnson V magnitude is derived by a combination of observations from ground based telescopes-satellite and it has a mean precision of 0.01 mag.

Moreover, the star mapper on board the ESA Hipparcos satellite allowed to collect observations in two filter passbands that were similar to B and V (Tycho Catalog; Høg et al. 2000), with a median precision of 0.01 mag for a 7th magnitude star and 0.04 mag for a 10th magnitude star.

The impact of such amount of data was huge. Before Hipparcos, the local stellar population of bright stars, in main sequence or in red giant phase, was poorly represented; moreover, the uncertainties on the distances were such to destroy the fine structure of the color-magnitude diagrams, limiting the available informations from nearby stars. After Hipparcos, it was possible to study the color-magnitude diagram in a statistical sense, beyond the simple comparison between evolutionary tracks and single stars. In other words, the first sample of disk stars statistically significant was available, giving the possibility to study the initial mass function, the star formation rate and the metallicity distribution with unseen accuracy. The figure 3.1(a) shows the color-magnitude diagram for a selection of Hipparcos stars (objects within 100 pc and brighter than $V = 7.3$), while the figure 3.1(b) represents stars with different tangential velocities, as obtained from the Hipparcos data.

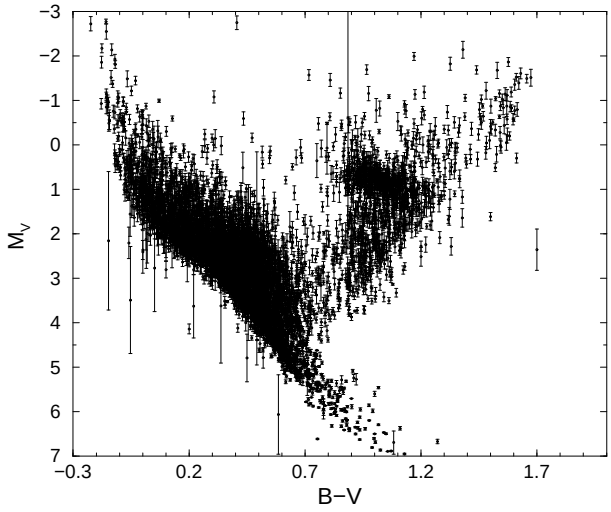

(a)

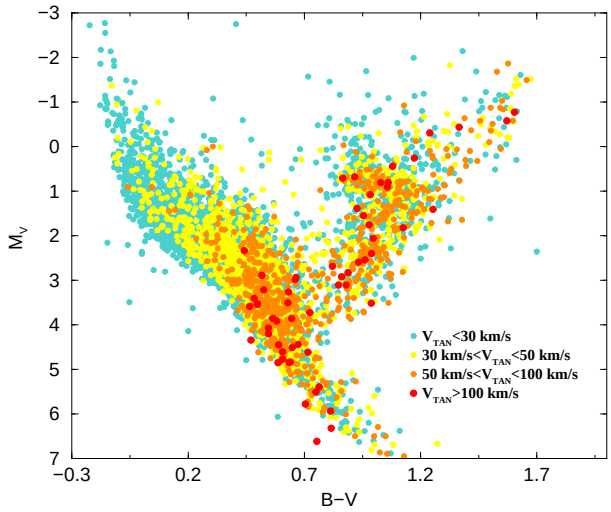

(b)

Figure 3.1: (a) Stars within 100 pc and with visual apparent magnitude less than 7.3 (from Hipparcos catalogue); (b) Same selection as in fi gure (a), but different tangential velocities are emphasized with different colors.

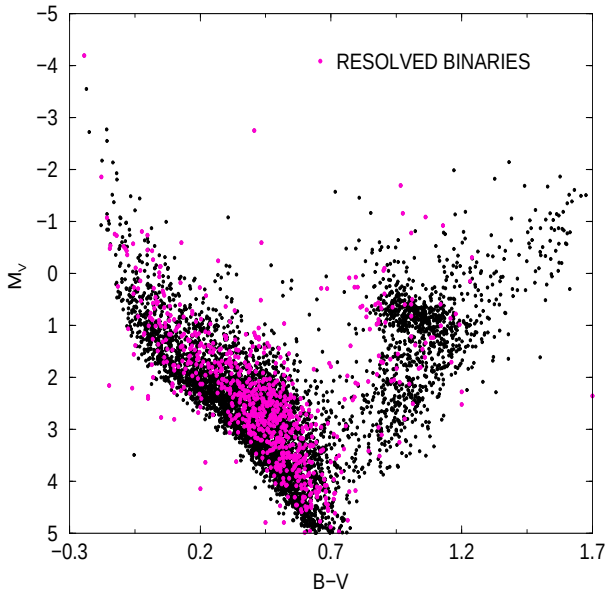

Figure 3.2: Black dots: Hipparcos stars within 100 pc and V magnitude less than 7.3. Magenta dots: Hipparcos resolved binaries.

3.2 Multiple stellar systems in the Hipparcos catalogue

The Hipparcos mission was carried out for 3.4 years and it allowed to identify new multiple system (especially binaries) in the solar neighborhood. Figure 3.2 shows the color-magnitude diagram for the components of the visual multiple stellar systems (within 100 pc and brighter than $V = 7.3$) resolved by Hipparcos mission. However, it is also estimated that Hipparcos does not resolve a fraction of the binaries present in its field of observation, mainly because of the small Hipparcos mirror and the lack of spectroscopic measures (the Hipparcos mission was not planned to study the multiple systems). In particular, Hipparcos lost:

a) binaries with angular separation below 2 mas (corresponding to the final astrometric precision of the satellite): in this case, the instrument was totally insensitive to the photocenter motion. The object was erroneously identified as single star;

b)binaries with separation between 2 and 440 mas: in this case, the motion of the photocenter was identified but a separation in components was impossible (the star has a variability flag);

c)binaries with one component much more bright than the other.

3.3 Hipparcos parallaxes: accuracy

Before analysing the Hipparcos CMD, it is needed to discuss the goodness of the parallaxes provided by Hipparcos mission. In literature there are two main methods followed to check this:
1) Comparing the parallaxes with independent measures (ground-based) of the same stars;
2) Analyzing the observed parallaxes from a statistical point of view (and comparing with the parallax error distribution provided by Hipparcos catalogue).

For the first approach, Arenau et al. (1995) claimed that the distribution of parallaxes differences (Hipparcos - photometric) does not present systematic shifts from a Gaussian: using a Kolmogorov Smirnov test, they found that the hypothesis of Gaussian distribution is not rejected at the 5%-significance level. Their result suggested that the Hipparcos parallax errors are normally distributed with mean 0 and variance equal to the square of the formal error.

Lindegren (1995) followed the second way using a Bayesian procedure. Following the notation of the previous chapter, the true parallaxes π_0 and the observative ones π can be thought as realizations of two probability density function (pdf), $f(\pi_0)$ and $f(\pi)$. Calling the conditional probability $F(X)$ with $X = \pi - \pi_0$, if π and X can be considered independent, the probability to observe π given the real value π_0 is:

$$f(\pi, \pi_0) = f(\pi_0)\, F(\pi - \pi_0) \tag{3.1}$$

So, the probability to observe π coming from whatever π_0 is:

$$f(\pi) = \int_{-\infty}^{+\infty} f(\pi_0)\, F(\pi - \pi_0)\, d\pi_0 \tag{3.2}$$

that is the convolution integral.

If one knows the distribution of true parallaxes, by deconvolution it would be possible to recover the conditional probability $F(X)$ (that is the error distribution). Vice versa, knowing the $F(X)$, one could use the distribution of true parallaxes as a kernel and performing another deconvolution to recover $f(\pi_0)$ from data.

Lindegren (1995) assumed a normal distribution for $F(X)$, with an unknown standard deviation σ (he considered also a mixture of Gaussians with different standard deviations,

so the σ parameter is the standard deviation of this pseudo-Gaussian). The distribution of observed parallaxes is de-convolved according this error distribution and imposing that no true parallaxes can be negative (positivity constraint). Then, the estimated true distribution is convolved again with the hypothized error distribution and compared with the data. The method is repeated changing the parameter σ until the best fit with data is obtained (the fit goodness is checked with a Kolmogorov Smirnov test).

For the deconvolution process the author used the Richardson Lucy algorithm. The goal was to gain informations on the error distribution and not on the distribution of true parallaxes. He found a ratio σ/σ_{INT} (with σ_{INT} the standard deviation derived by the Hipparcos reduction consortia) equals to 0.99 ± 0.02, confirming that the distribution of parallax errors is unbiased.

3.4 From parallaxes to magnitudes

However, the information of the parallax is not the final product to compare with the stellar evolution: transforming the trigonometric parallax in absolute magnitude implies a non linear transformation, that is, even if the individual parallaxes are unbiased (that is there is equality between expectation values $E[\pi] = E[\pi_0]$), in general $E[h(\pi)] \neq E[h(\pi_0)]$ (with h a generic non linear transformation). This effect is discussed in Arenau & Luri (1999), which shows that, even if the error law for the parallaxes is symmetric, the derived quantities could loose this feature. In other words, assuming a Gaussian law for parallax error $\pi \sim N(\pi, \sigma)$, a "true" distance $\frac{1}{\pi_0}$ and an observed distance $d = \frac{1}{\pi}$, the authors obtain a bias

$$E[d|\pi_0] - \frac{1}{\pi} = \frac{1}{\pi}\frac{1}{\sqrt{pi}}\int_{-\infty}^{+\infty}\left(\frac{1}{1+u\frac{\sigma}{\pi_0}}\right)e^{-\frac{u^2}{2}}du \tag{3.3}$$

where $E[d|\pi_0]$ is the expectation value of the observed distance distribution (given π_0).

The same equation corresponds, in terms of magnitude (M)

$$E[M|\pi_0] - M = 5\frac{1}{\sqrt{pi}}\int_{-\infty}^{+\infty}\log\left(1+u\frac{\sigma}{\pi_0}\right)e^{-\frac{u^2}{2}}du \tag{3.4}$$

It is interesting to notice that the bias depends on the therm $\frac{\sigma}{\pi_0}$, that involves the unknown real parallax. This occurrence implies an intrinsic difficulty to correct this bias, because we should know the underlying true distribution of parallaxes. The same feature gives also a possible solution. From equation 3.4 we understand that selecting stars with small relative error the bias is attenuated. In particular, considering only precisions $\frac{\sigma}{\pi_0} < 0.1$, this bias is negligible.

3.5 Completeness

The Hipparcos mission observed objects down to a limiting magnitude of about $V = 12.5$ mag, with a completeness limit depending on the galactic latitude b and on the spectral type (Perryman et al. 1995): $V < 7.9 + 1.1 \sin b$ for spectral type earlier or equal to G5, $V < 7.3 + 1.1 \sin b$ for spectral types later than G5.

In order to simplify the analyses of the Hipparcos sample, it is useful to choose a cutoff in visual apparent magnitude, independently by galactic latitude and spectral type, and to check if the sample is still complete against Malmquist bias (in a magnitude limited sample, the brighter stars are statistically over-represented; see section 2.5.1). It is adopted a cutoff at $V = 8$. Comparing the luminosity functions for subsamples with similar distance from the Sun, the bias can be quantified. Figure 3.3 shows the luminosity functions for stars between d_i (distance from Sun) and $d_i + 10\,\mathrm{pc}$. Using a Kolmogorov-Smirnov test, the hypothesis that the luminosity functions are realizations of the same distribution (for the range $-1 < M_V < 3.5$) is not rejected at the 10%-significance level. Thus, the sample selected at $V = 8$ should be complete at least up to 80 pc and $M_V = 3.5$.

3.6 Selecting a volume limited sample from Hipparcos catalogue

For our analysis I will use stars from the Hipparcos catalogue:

1. brighter than $V = 8$
2. within 80 pc from the Sun.

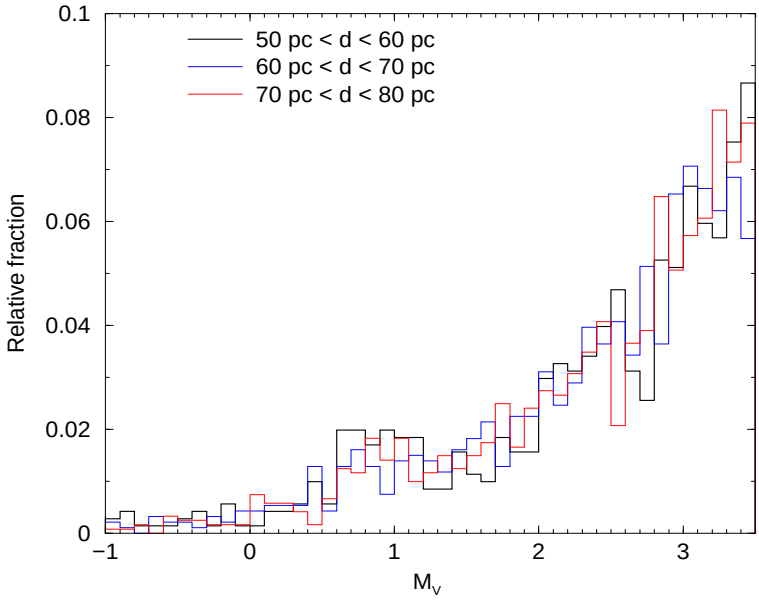

Figure 3.3: The luminosity function for stars selected in distance (the interval is labeled). All the stars are brighter than $V = 8$.

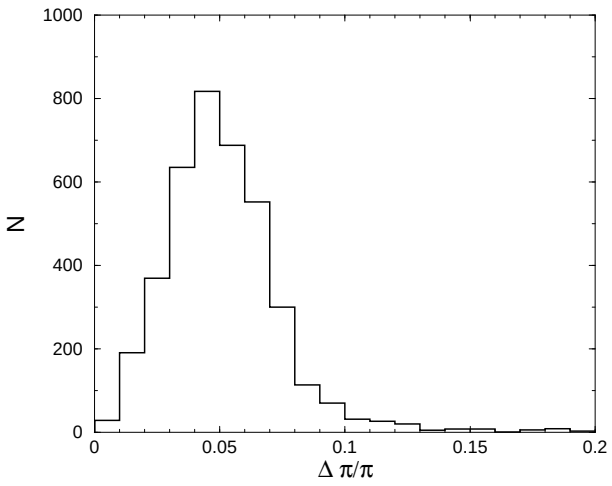

Figure 3.4: Distribution of the parallax precision for Hipparcos stars within 80 pc and brighter than $V = 8$.

The result is a sample of about 4000 stars brighter than $M_V = 3.5$ mag. The parallax error is generally better than 10% (see figure 3.6), thus the non-linearity bias can be assumed very small (see equation 3.4).

If we build the absolute magnitude error distribution for the selected sample (by error propagation from the parallax errors, see fig. 3.5(a)), it is found a mean value of about 0.10 mag, with a standard deviation around 0.05 mag. We could ask if this distribution

changes going through the color-magnitude diagram. The figure 3.5(b) shows the absolute magnitude error distribution for stars in three different intervals of absolute visual magnitude, respectively $2-2.5, 2.5-3, 3-3.5$ mag. The distributions for stars with $2 < M_V < 2.5$ and $2.5 < M_V < 3$ are within the Poissonian fluctuations (the error bars are indicated in the figure), while the distribution $M_V = 3 - 3.5$ presents a very slightly systematic shift (about $0.01 - 0.02$ mag) towards larger errors. The explanation for this effect should be the photon noise that, for faint magnitudes, increases the standard errors on the parallaxes. However, it is a small displacement and can be neglected: the distribution for the absolute magnitude errors can be considered independent by the position in the CMD.

Consider now the photometric error in $B - V$. Figure 3.6 shows two curves: one indicate the distribution of Hipparcos stars with only ground based photometry, the other is composed by Hipparcos stars with Tycho photometry. Independently by the source, that bulk (at least for stars brighter than 3.5) of objects have $B - V$ errors less than 0.015 mag. There is also an high error tail ($B - V$ uncertainties greater than 0.02) composed essentially by giant and clump stars, but only the $1 - 2\%$ of the total sample populate this tail.

In conclusion, the most important uncertainty for the selected sample is certainly the parallax error. How we will see better in chapter 5, the useful feature that the relative distribution of uncertainties is independent (at least for our sample) by the position in the CMD gives the possibility to "clean" the CMD by using a deconvolution algorithm.

3.7 Clusters contamination

Before closing this chapter, it is performed another selection looking for contaminations by clusters or associations. Figure 3.7 shows the identified associations members within 80 pc and brighter than $V = 8$. The most significative contamination is by the Hyades cluster with about 120 identified members.

Thereinafter, we will identify as the Hipparcos sample the selection as defined in the previous where the identified cluster members are eliminated.

In fact, the goal of this work is to test the possibility to extract the galactic star forma-

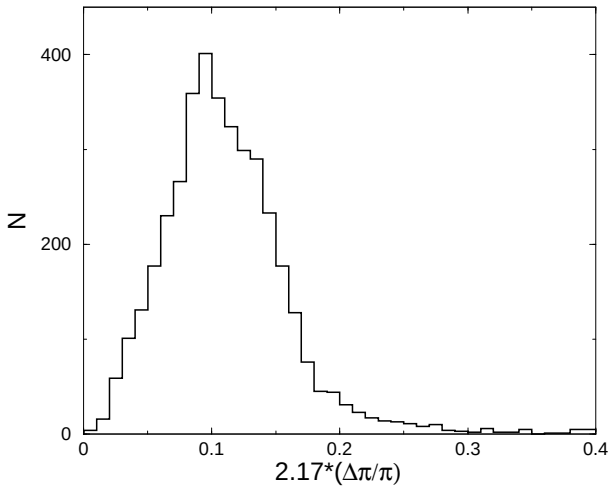

(a)

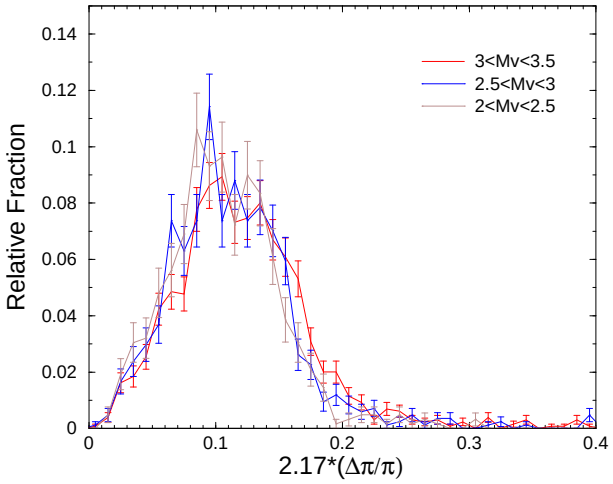

(b)

Figure 3.5: (a) Hipparcos stars: the absolute magnitude error distribution for stars brighter than 3.5 and nearer than 80 pc. (b) as for (a), but for different intervals of absolute magnitude. The error bar is Poissonian: the fi gure shows the general agreement among the curves.

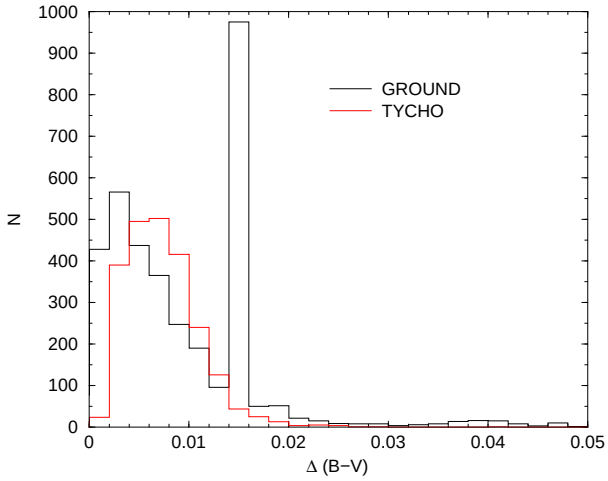

Figure 3.6: Distribution of uncertainties in $B-V$: the red curve represents the errors in $B-V$ as measured by the Hipparcos star mapper (Tycho catalogue). In black the distribution of $B-V$ errors for stars for which the Tycho $B-V$ was not available, so the uncertainty in $B-V$ comes from ground base telescopes.

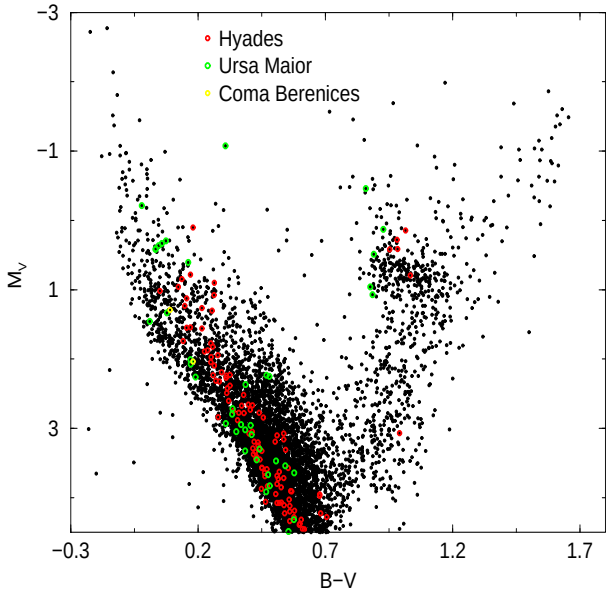

Figure 3.7: Members of associations within 80 pc and brighter than $V = 8$.

tion history, while the associations are example of local evolution.

4

Interpreting the Hipparcos CMD

4.1 The theoretical inputs

To understand the star formation history behind the observational CMD we need to model a synthetic population with various theoretical ingredients (and after to quantify the match between theoretical and observational CMD).

Following a Montecarlo technique, each theoretical CMD is populated with a large number of stars randomly built by a set of theoretical ingredients governed by the corresponding parameters:

- the initial mass function (IMF) gives the number N of stars in each generation per unit interval in stellar mass M. A generally used form is a power-law:

$$dN \sim M^{-s} dM \tag{4.1}$$

  As usual, it is assumed to be independent of time (see discussion in paragraph 1.3;

- The star formation rate (SFR) determines the number of stars of all masses born at each epoque;

- The age-metallicity relation (AMR) Z(t). Due to the galactic evolution, the chemical composition of the gas from which stars were born changes with time.

Table 4.1: Chemical composition of the stellar tracks.

Z	Y
0.04	0.29
0.03	0.29
0.02	0.27
0.015	0.27
0.01	0.27
0.008	0.25
0.004	0.23
0.001	0.23
0.0006	0.23
0.0002	0.23

- the binary population (characterized by a specific distribution of mass ratios);

The code relies on a set of homogeneous evolutionary computations covering with a fine grid the mass range $\approx\ 0.1$ to $\approx\ 7M_{\odot}$ for the chemical compositions shown in Tab. 4.1. The history of the Galaxy matter is characterized by a continuous enrichment of helium and heavy elements following the generation of stars and their emissions of produced elements in the interstellar medium. The amount of original helium has been evaluated by assuming a primordial helium abundance $Y_P = 0.23$ and $\Delta Y/\Delta Z \sim 2$ (see e.g. Pagel & Portinari 1998, Castellani, Degl'Innocenti, Marconi 1999a).

For masses higher than 0.5 $M_{\odot}$ we use the Cariulo et al. (2004), Castellani et al. (2003), Castellani, Degl'Innocenti, Marconi (1999) evolutionary tracks, partially available at the URL: http://astro.df.unipi.it/SAA/PEL/Z0.html.

All the models with evolutionary times smaller than the Hubble time have been followed from the Main Sequence through the H and He burning phases, until the C core ignition or the onset of thermal pulses in the advanced AGB phase. In the case of low mass stars undergoing violent He flashes, stellar structures at the Red Giant Branch (RGB) tip have been used to produce the corresponding Zero Age Horizontal Branch (ZAHB) mod-

els, further evolving these models until the onset of thermal pulses. Less massive stars (0.5 $M_\odot$ <M<0.7 $M_\odot$), whose evolutionary times are longer than the Hubble time, have been evolved up to central H exhaustion. For very low mass stars (M<0.5 $M_\odot$) we used the Zero Age Main Sequence positions by Baraffe et al. (1997,1998).

The input physics adopted in the models are described in Cariulo et al. (2004). We only point out here that the models take into account atomic diffusion, including the effects of gravitational settling, and thermal diffusion with diffusion coefficients given by Thoul, Bahcall & Loebe (1994). Effects of rotation are not included.

Convective regions, identified following the Schwarzschild criterion, are treated with the mixing length formalism in which the mixing length parameter α defines the ratio between the mixing length and the local pressure scale height: α = l/H_p. The models have been satisfactorily tested relative to Solar Standard Models (see e.g. Degl'Innocenti et al. 1997), young metal-rich galactic clusters with Hipparcos parallaxes (Castellani, Degl'Innocenti, Prada Moroni 2001, Castellani et al. 2002) and moderately metal-rich galactic globulars (Castellani et al. 2003). We have adopted – in all cases – α =1.9 which has been calibrated in a way to reproduce, with the adopted color transformations, the observed RG branch color of the galactic globular clusters and young globulars in the LMC (Cariulo et al. 2004, Castellani et al. 2003, Brocato et al. 2003).

The solar mixture adopted for the calculations is $(Z/X)_\odot$=0.0245 (Grevesse & Noels 1993). Recently new evaluations for the solar mixture have been made available; however numerical simulations show that the effect, at fixed metallicity, of the change of the solar mixture on the evolutionary results is negligible for our purposes (Degl'Innocenti, Prada Moroni, Ricci 2005).

We use throughout the canonical assumption of inefficient overshooting and the He burning structures are calculated according to the prescriptions of canonical semiconvection induced by the penetration of convective elements in the radiative region (Castellani et al. 1985).

Each star evolved beyond the AGB phase and less massive than the lower mass limit for supernovae ($M_{UP} \sim 7\,M_\odot$) is assumed to be a white dwarf. However, to predict the CMD location of WDs, one needs further theoretical ingredients, as given by (i) a white dwarf mass-progenitor mass relation (taking into account the mass loss during the

asymptotic giant branch phase), (ii) theoretical WD models giving the luminosity and temperature of a WD as a function of mass and age (Salaris et al. 2000), and (iii) suitable color transformations. The WD cooling age (i.e., the time spent on the cooling curve) is simply given by the difference between the age associated with the star and the age of the WD progenitor at the end of the AGB. For $T_{eff} < 4000K$ we adopt the color relations by Saumon & Jacobson (1999), which include a detailed treatment of collision induced absorption of H2, whereas for higher temperatures the results of Bergeron, Wesemael & Beauchamp (1995) were used. For the white dwarf mass-progenitor mass relation we adopted Weidemann (2000).

4.2 Building an artificial CMD

In order to give an interpretation of the data for the nearby stars, we must check that the features of the CMD are not artifacts due to photometric or parallax errors, but they are connected to stellar and galactic evolution. For this analysis I selected from Hipparcos sample (objects closer than 80 pc and brighter than $V = 8$) only stars with parallax precision better than 10% and photometric error smaller than 0.2 mag.

The figure (4.1, left panel) shows how the CMD of Hipparcos stars look likes after this selection. For comparison I built an artificial CMD (figure 4.1, right panel) with solar metallicity, flat star formation rate, no binaries and the Salpeter IMF (thereinafter, simply indicated as “artificial CMD”). As well known, the places where the stars gather identify different stellar evolutionary phases. In particular we can recognize stars in the main sequence, in sub giant, in red giant and in the clump phase. Another striking feature is the overall enlargement we observe in the data CMD compared with the artificial CMD.

The selection on the observational error allows to conclude that the spread of the data CMD cannot be due to observational uncertainties. How we will show in details in the next sections, this spread is due to both the presence of stars with different chemical composition and to evolutionary effects in the sample.

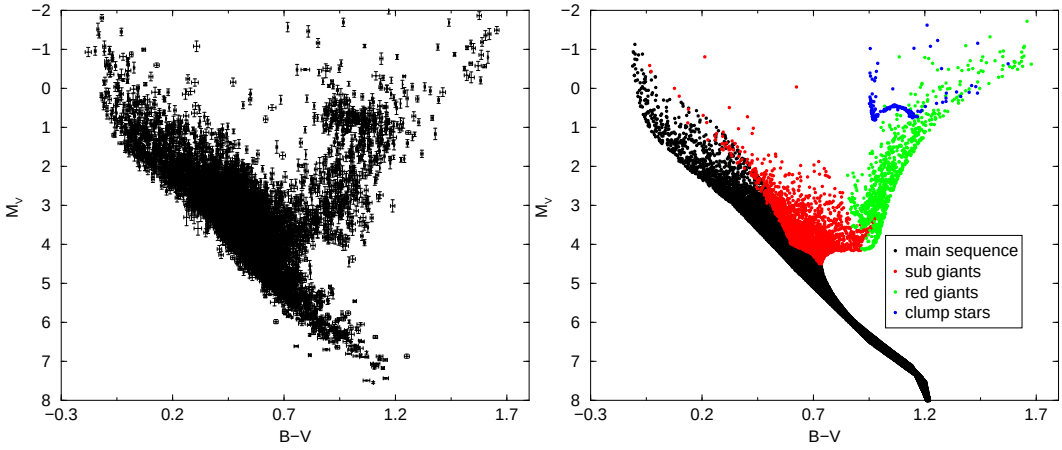

Figure 4.1: Left panel: CMD of the Hipparcos observational sample. Only stars with relative parallax error less than 0.1 and $B-V$ error less than 0.02 mag are shown. Right panel: artificial CMD generated with a solar metallicity, flat star formation rate, no binaries and a Salpeter IMF. The different color represent stars in different stellar phases.

4.2.1 Chemical composition

In spite of the global morphology of the CMD does not change with changes in metallicity, the precise position of a star on the CMD depends on the chemical composition namely the mass fraction of hydrogen, helium and metals (X, Y, Z respectively). The abundance of He and metallicity influence the stellar structure in two different ways. The Y content mainly acts on the molecular weight μ and the Z content mainly changes the radiative opacity and the CNO burning efficency.

Increasing Y means to increase μ and this influences the hydrostatic equilibrium. The pressure decreases and the star shrinks (producing heat), reaching a new equilibrium characterized by a smaller radius and higher central temperature. As a consequence, the efficiency of the central burning increases and this brings the star to be brighter and hotter. This phenomena is exemplified in figure 4.2, where two stellar tracks ($m = 1.2\,M_{\odot}$) with same metallicity but different helium content are shown.

Regarding the variation of Z, we know that as long as bound-free processes dominate, the opacity is proportional to Z (this relation falls when the metallicity is lowered below $0.1\,Z_{\odot}$ and the free-free transitions dominate). So an increase of Z leads to an increase of the opacity. The effect is that, at first approximation, the radius is unchanged while the flux is modified bringing a decrease of the surface luminosity. If we add that the radius is

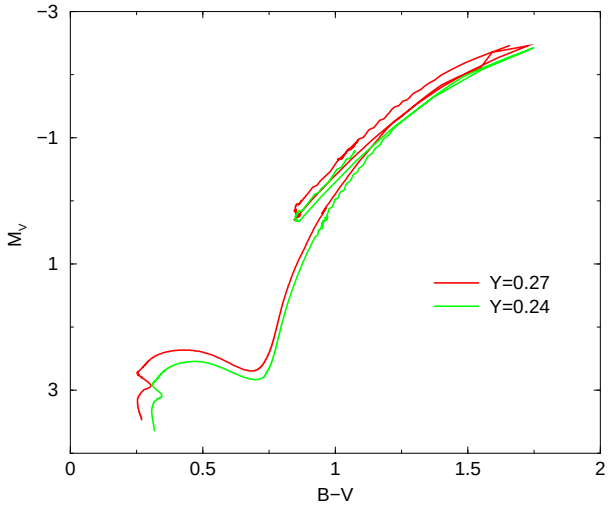

Figure 4.2: The evolutionary tracks for two stars of same mass ($m = 1.2\,M_{\odot}$), same metallicity (Z=0.004) but two different helium abundances.

remained the same, we find that the surface temperature decreases too.

Another effect connected with a Z variation and relevant for stars more massive than $1.1\,M_{\odot}$ in main sequence is the CNO burning rate ϵ: increasing Z the CNO energy production increases and the star can produce the same luminosity with a lower central density and temperature; consequently the luminosity and the surface temperature drop off.

Taking into account both the opacity and the burning efficency changes, the global effect of a Z decreasing is to increase surface temperature and luminosity. This phenomena is exemplified in figure 4.3, where two stellar tracks of the same mass, same helium content but different metallicity are drawn.

Thus the variation of Z and Y parameters in the same direction causes opposite effects on the stars. However, as long as we consider sub-solar metallicities, the main effect of a metallicity variation is to modify the opacity. Over the solar value the μ effect begins to be competitive with the opacity effect, as long as, for $Z > 0.05$, the μ effect dominates (see Mowlavi et al. 1998).

As an example, in figure (4.4) we have drawn stellar tracks with same masses ($1\,M_{\odot}$), but three different chemical compositions superimposed to the Hipparcos CMD.

If one looks at the starting point of the tracks at the beginning of the central H burning (zero age main sequence points, ZAMS) in fig. 4.3 one can see that they cover about 0.3 mag in color, a displacement equal or even higher than the observed main sequence

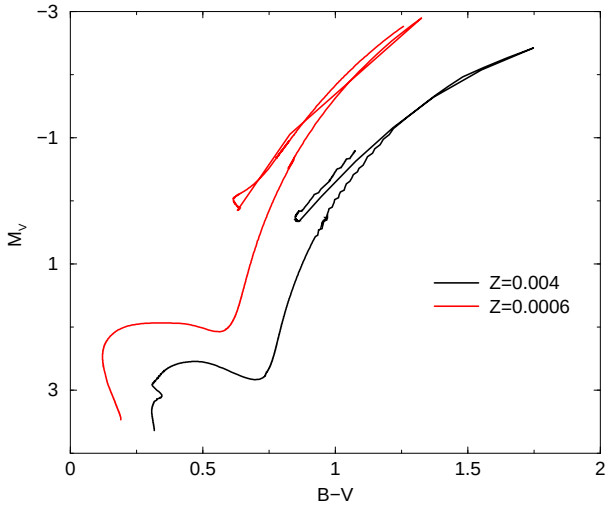

Figure 4.3: The evolutionary tracks for two stars of same mass ($m = 1.2\,M_\odot$), same helium content (Y=0.23) but with the indicated metallicities.

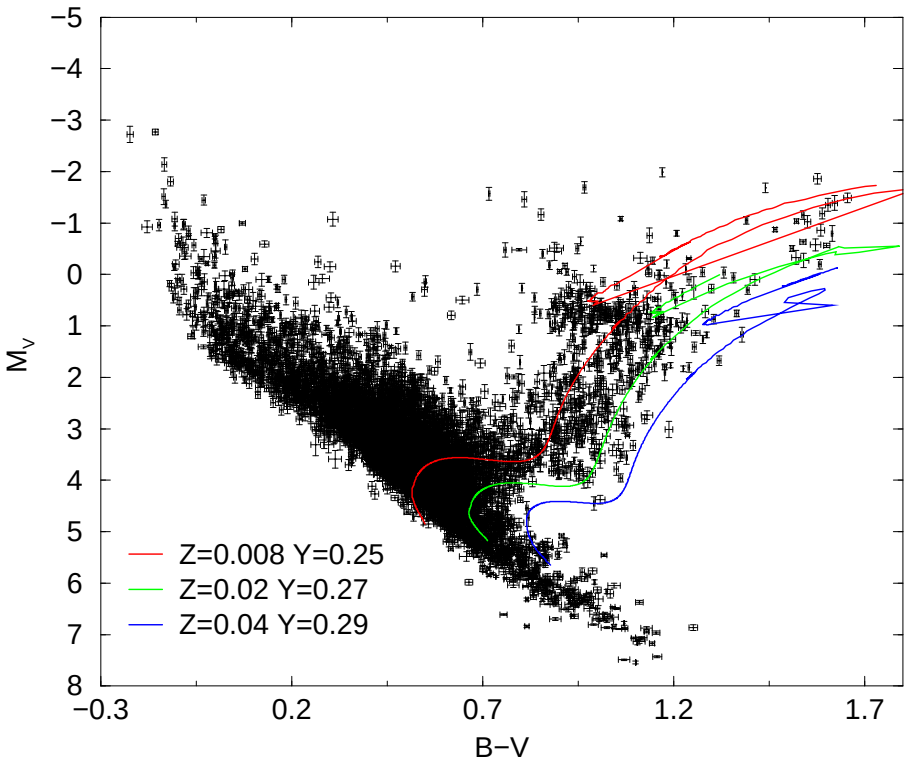

Figure 4.4: Dots: Hipparcos sample. The lines are stellar tracks (same mass, $1M_\odot$) for the labeled chemical compositions.

broadening in the Hipparcos field (see fig. 4.4). Thus, the presence of stars with different chemical composition is the main reason for the observed spread.

4.2.2 Evolutionary effects

In this section I will give a short overview on the different stellar evolutionary phases in order to find a correspondence with the Hipparcos CMD features (for major details see e.g. Kippenhahn and Weigert, 1990).

There is another reason that can account for the main sequence broadening: the stars spend most of their time on the main sequence slightly changing luminosity and temperature from the ZAMS position to the central H exaustion and then they fast evolve off, varying luminosity and temperature by a relevant amount. However, the displacement in luminosity and temperature covered by a star of given mass during the main sequence phase is not negligible (see figure 4.5).

As well known, the time spent on the main sequence depends on its mass. In fact, the time scale is

$$\tau_H = \frac{E_H}{L} \tag{4.2}$$

where E_H is the amount on nuclear energy available for the star during central H burning and L is the stellar luminosity. A first estimate can be found realizing that $E_H \propto M$ (the total mass), while L for a zero age main sequence is proportional to M^n, where n varies from 3 to 4. Adopting a mean value, we obtain

$$\tau_H \sim M^{-2.5} \tag{4.3}$$

so, the time scale for central hydrogen burning is very mass dependent. The numerical results are shown in figure 4.5.

Moreover, the evolutionary times depend on the chemical composition, as a direct result of the previously mentioned dependence of the luminosity by metallicity and Y abundance. From stellar evolution theory, it is known that in main sequence phase, stars with $M < 1.1 M_\odot$ burns H in the center mainly through the proton-proton chain while higher mass burns H mainly through the CNO cycle. As a consequence, stars with masses $M > 1.1 M_\odot$ have a convective core (which size grows up with the mass of the star), due to the higher energy fluxes in the central region, while lower masses have a radiative core. This difference is also reflected in the trajectory they follow during the core hydrogen burning on the main sequence: stars below $1.1\, M_\odot$ move upwards in L and slightly to higher surface temperatures, while higher mass stars also increase their luminosity but

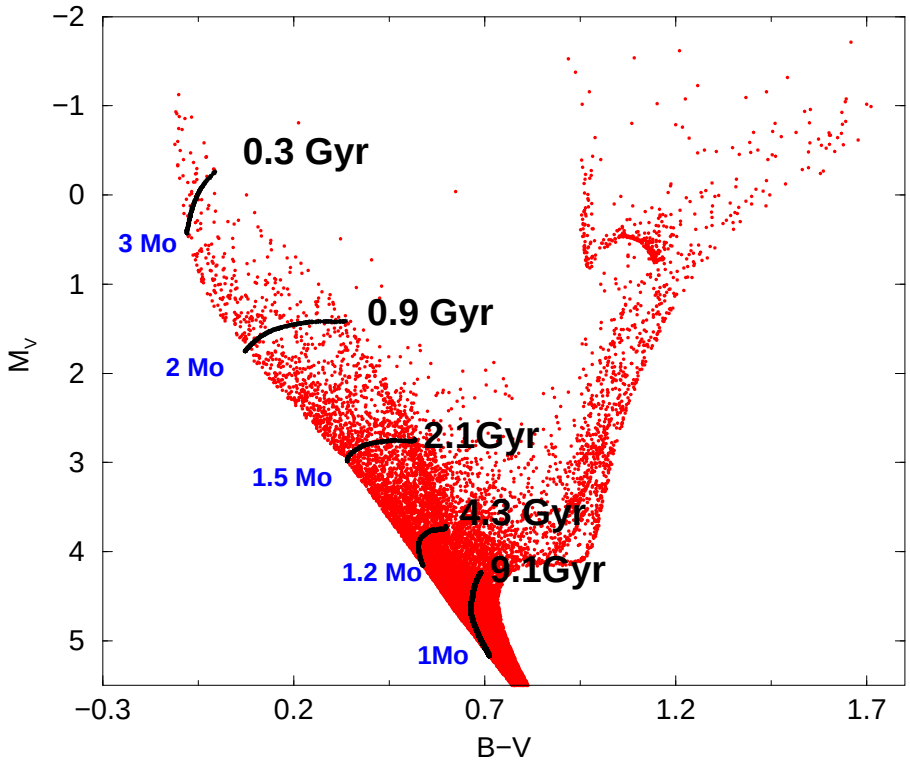

Figure 4.5: Main sequence evolution for masses of solar composition superimposed to the artificial CMD. The age on the tracks shows the relative lifetime.

toward a region of lower temperature. Exactly for this reason, the main sequence evolution for low mass stars is quite vertical (see the $1\,M_{\odot}$ track in figure 4.5). If we add that the evolutionary times increase abruptly lowering the stellar mass (so the displacement in the color magnitude diagram is slower), this endorses our idea that, at least for the lower main sequence, the observed spread in the Hipparcos stars is mainly a metallicity effect. The simulations seems to confirm this result: in figure 4.6 we compare a simple simulation of the solar neighborhood, done with a flat star formation rate (from 10 Gyr ago up to now) and solar composition, with the Hipparcos observations: it is impossible to explain, with evolutionary effects only, the broadening for stars with absolute magnitude greater than 4. For solar metallicity, this limit in magnitude corresponds to a mass of about $\sim 1.2\,M_{\odot}$: during the central hydrogen burning these objects evolve very close to the main sequence and this determines the narrow appearance of the artificial color-magnitude diagram.

The main sequence evolution ends when the star has exhausted the hydrogen content in the core. To understand the following evolution, we have to introduce the concept of critical mass known Schonberg-Chandrasekhar limit. After central hydrogen burning, the

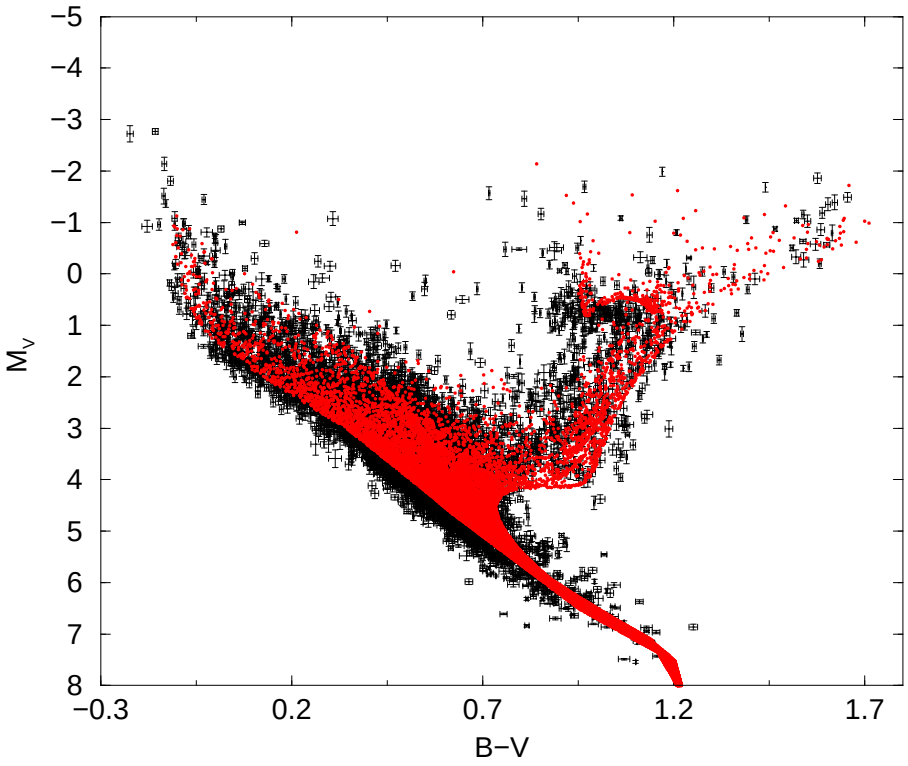

Figure 4.6: The Hipparcos observational sample (black dots) and the artificial data (red dots) of fig. 4.5 superimposed.

helium core, without an internal energy source, tends to be isothermal (without energy sources, the luminosity of the core drops off and the temperature gradient follows it). All around this core, at the bottom of a hydrogen rich envelope, the burning goes on in a thin shell. The structure formed by an isothermal core with an envelope could be unstable, with the weight of the envelope overcoming the interior pressure of the core. From theoretical computations we know that it exists a maximum ratio between the core mass and the total mass of a star:

$$M_{core}/M_{TOT} = 0.37(\mu_{envelope}/\mu_{core})^2 \tag{4.4}$$

where $\mu_{envelope}/\mu_{core}$ is the ration between the molecular weights. For a helium core surrounded by hydrogen this value is close to 0.09. This limit is exceeded by helium core after central hydrogen burning for masses over about $1\,M_\odot$ (we remind that masses of about $\sim\ 1\,M_\odot$ and solar composition have a MS lifetime of $\sim\ 10$ Gyr and thus reach the RGB in a time less than the Hubble time). These stars burn hydrogen in a shell and they rest close to the main sequence until a further increase of the core mass overcome

the SC limit, leading the inner region toward a rapid contraction (on thermal time scale). At the same time, the layers above the shell source expand: the star cools abruptly until it reaches a new equilibrium configuration, characterized by a large radius (red giant). The phases between the main sequence and the new equilibrium are so fast (thermodynamic evolution) that the probability to observe stars is low (compared to the nuclear phases). This causes the well-known Hertzsprung gap.

The masses below $1\,M_{\odot}$ do not follow the same history, because there is another factor to take into account, that is the electronic degeneracy in the interior. If we increase the total mass of a star, the central temperature increases while the central density decreases. For masses below $1M_{\odot}$ the values of central temperature and density leads the stellar cores in a state of electronic degeneracy (that vanish completely only for masses above $\sim 2.5\,M_{\odot}$). In consequence of this, the post main sequence evolution for these stars is not so dramatic as for higher mass stars. The degeneracy makes the SC limit no more efficient, because the degeneracy pressure avoids the star rapid core contraction. The time scale between the main sequence and the red giant solution is now nuclear, making high the chance to find stars in this phase. The numerical calculations give the time scales shown in figure 4.7.

The now discussed difference between low and high mass post-main-sequence evolution is evident in the artificial CMD of figure 4.7: for stars above $M_V \sim 3$ (masses above $1.4\,M_{\odot}$), the number of objects between main sequence and red giants branch is low. This number increases approaching to $M_V \sim 4$, where a maximum is reached for masses between 1 and $1.4\,M_{\odot}$. Going deeper, we are looking stars not evolved again from main sequence, so the number drops off.

When the star has exhausted the central hydrogen, the burning zone moves to a shell. Without an energy source, the helium core starts to contract under its own gravity. The energy arising from the core contraction and the shell H burning is transferred to the envelope which expands and cools, even while the core is collapsing. The process goes on until the temperature gradient overcome the adiabatic gradient and the entire envelope becomes convective (red giant). This phenomena is hurried up by the increased size of the envelope that lowers the surface temperature: the first consequence is an increased opacity that decreases the radiative flux (promoting the convection).

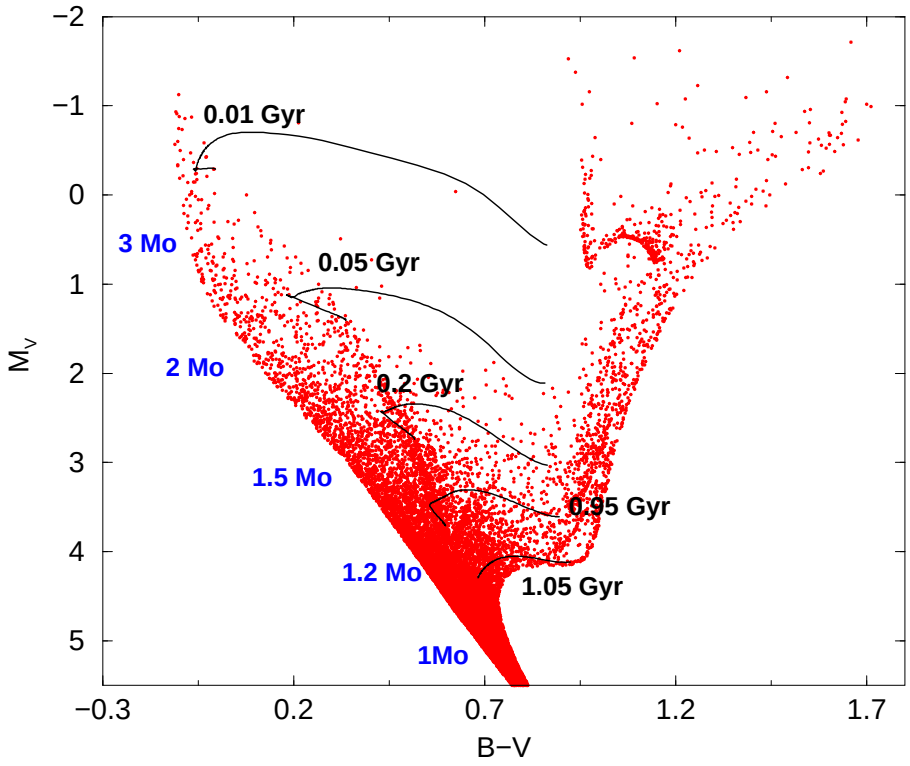

Figure 4.7: Red dots: artifi cial CMD for solar metallicity. Black lines: sub giant evolution for stars of different masses from which the artifi cial CMD is calculated; the corresponding timescales are reported. It is clear how the lower probability to fi nd massive stars in sub giant phase is due to the shorter evolutionary times.

The star ascends the giant branch, burning hydrogen in a shell and increasing the mass of the helium core.

For low mass stars ($M < 1.2\,M_{\odot}$), H shell burning increases the degenerate He core mass. It keeps contracting as pressure depends only on density (a completely degenerate gas has a polytropic equation of state). The released potential energy increases the temperature up to 10^8 K and He burning starts. The structure starts to ignite helium off center because neutrino cooling is more efficient where the density is higher, so the center of the structure results cooler than the upper layers. Due to the degeneracy, this causes the burning rate to increase following a runaway process. This is called core helium flash. A stable configuration is reached when the degeneracy is removed and the core expands. After He flash star is hotter, smaller and less luminous.

Masses above $2 - 2.5\,M_{\odot}$ (the exact value depends on the initial chemical composition) have not a degenerate core, so the contraction leads to direct heating. Reached 10^8

K the helium core burning starts quietly in the center of the structure. This different evolution between masses below and above $2 - 2.5\,M_{\odot}$ corresponds to different lifetimes of the red giant phase (see figure 4.8). The core degeneration delays the ignition, increasing the chance to find stars in this phase.

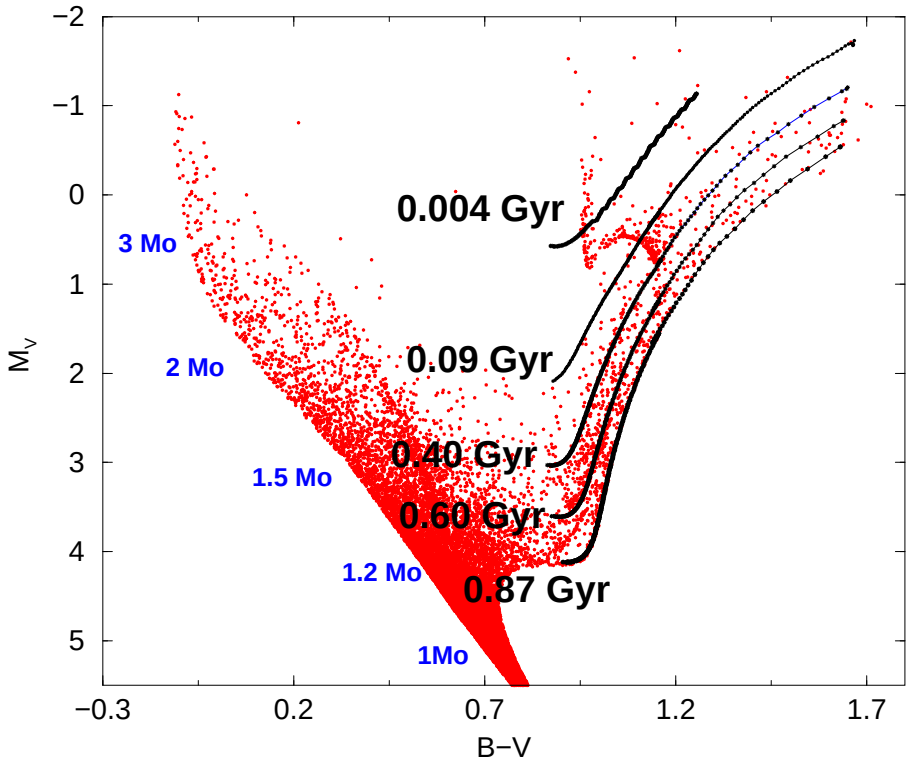

Figure 4.8: Red dots: artificial CMD. Black lines: red giant evolution for stars of the labeled masses. The corresponding lifetimes are labeled: it is worth to note that more massive stars have progressively shorter evolutionary times, a situation reflected by the artificial diagram where the massive stars in red giant phase are missing.

Another effect of the electron degeneracy is to build up an helium core of approximately the same mass ($0.45 - 0.5\,M_{\odot}$). As the mass of the star increases the He core is less degenerate and this leads to shorter RGB lifetime and to smaller He core. The trend is broken when a mass of $2 - 2.5\,M_{\odot}$ is overcomed: the degeneracy is vanished and the He core mass increases with total mass, following the increasing size of the central convective core in the main sequence structures.

The star luminosity during central helium burning is a combination of the luminosities produced by the helium core and the H burning shell. The figure 4.9 shows evolutionary tracks for central burning helium stars (the large majority of stars in our observational

sample is more massive than $1\,M_{\odot}$, whose the mass loss in RGB is negligible, thus the population of central burning helium stars is computed without taking into account mass losses during the RGB phase). For masses below $2\,M_{\odot}$, the luminosity of the structures increase with the mass: although the mass of the helium core slightly decreases, the enhanced H shell burning supply the decreased output of He-burning reactions. Reached a maximum in luminosity at $2\,M_{\odot}$, the luminosities drop off because the helium core reduction dominates. The attainment of the minimum for the He core mass (around $2.3\,M_{\odot}$ for solar composition) determines a minimum in luminosity. By further increasing the stellar mass the He core increases as a consequence of the extended convective core in the main sequence phase leading to brighter He burning structures. Figure 4.9 shows the evolution of different masses, during central helium burning, superimposed to an artificial CMD (solar metallicity, flat SFR).

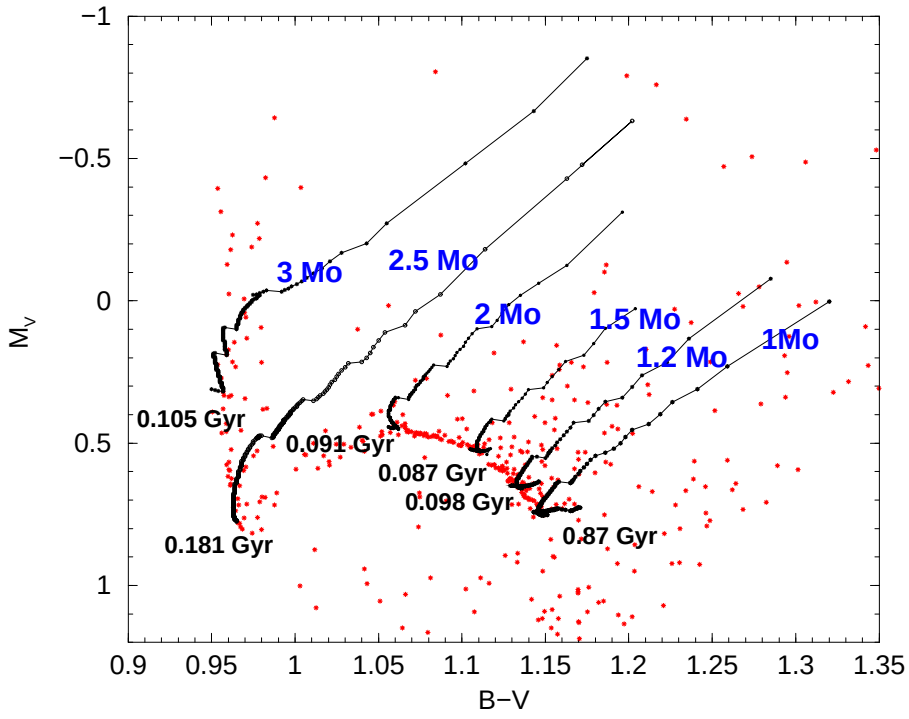

Figure 4.9: Red dots: artifi cial CMD. Black lines: central helium burning evolution for stars of different masses and solar metallicity. The corresponding lifetimes are labeled.

As a compendium of the stellar evolution phases now discussed, figure 4.10 presents a set of stellar tracks from main sequence to central helium burning, for masses between $0.7\,M_{\odot}$ and $7\,M_{\odot}$ (superimposed to the Hipparcos sample).

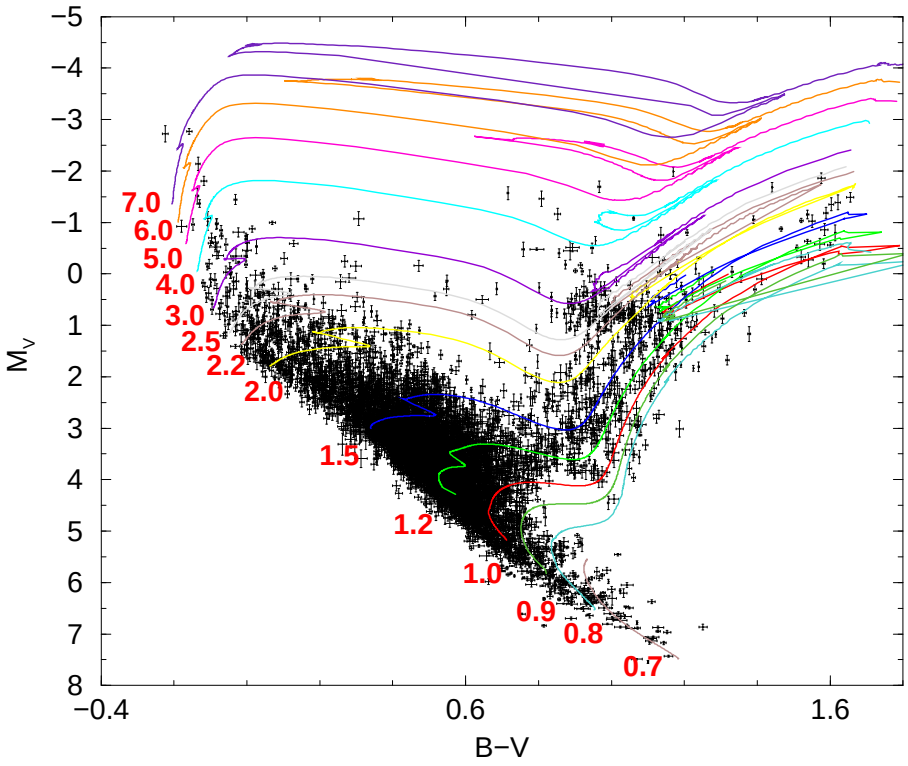

Figure 4.10: Evolutionary tracks for masses between 0.7 and 7 $M_{\odot}$ compared with Hipparcos sample (black dots).

4.3 Stellar ages mapped by Hipparcos

Until now I have shown how the stellar evolution and thus the behavior in the CMD can change with stellar mass and chemical composition. The Hipparcos stars, as a sample of disk stars, form a composite population. In this section I will try to answer to the question: what we can understand about the disk star formation rate from the Hipparcos sample? We have seen that different masses have very different evolutionary times. Massive stars live for short times (compared to the age of the Universe), while objects smaller than $1.5\,M_{\odot}$ can survive for many Gyr, mapping the recent as well as the ancient star formation rate. Due to the fact that different masses populate different regions of the CMD (this situation is well pictured in the artificial CMD of figure 4.11, where different mass intervals are populated with the same flat star formation), different regions of the CMD tell us different informations about the past star formation history.

Obviously the situation is not so simple, first of all because the Hipparcos stars can have different chemical compositions. As already discussed, a variation in the chemical

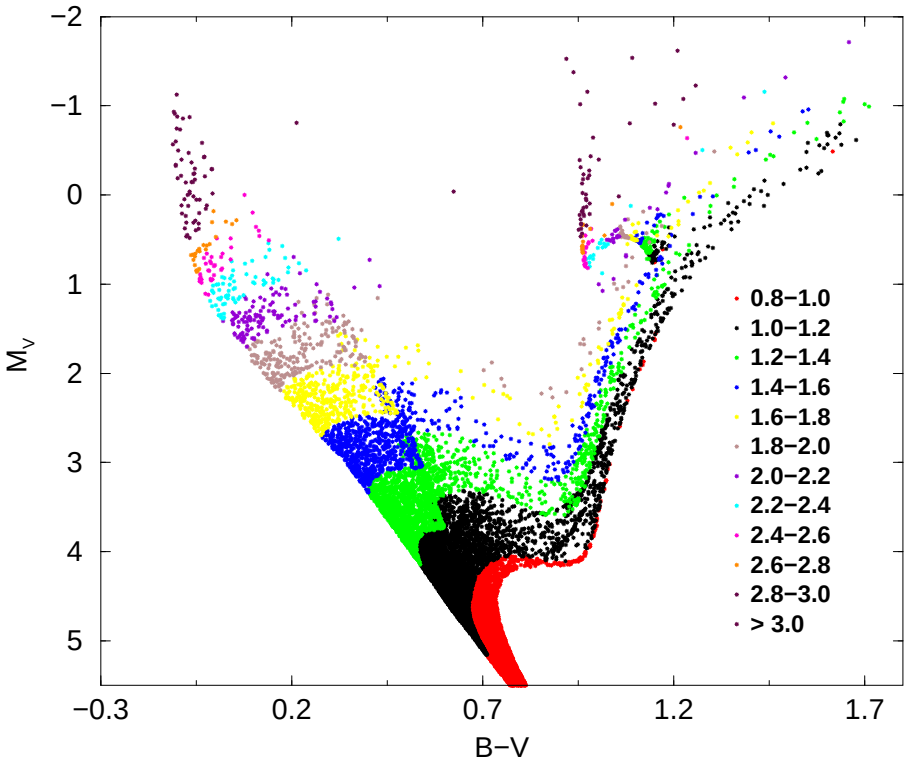

Figure 4.11: Artifi cial CMD: different colors indicate different artifi cial populations with a narrow range of masses (in solar masses): each population is obtained with the same initial number of stars, but masses in the indicated intervals only. The star formation is assumed flat between 0 and 12 Gyr.

composition have two main effects:

1) It mimics an evolutionary effect.

2) At fixed stellar mass, different compositions lead to different evolutionary times (so the same mass range can cover different lifetimes)

Another difficulty can be represented by the presence of binaries; I will analyse this point in section 4.4.

For the moment, using the usual artificial population generated with solar composition, no binaries, flat SFR, we can build a frequency-age plot (specific for different mass range) to understand how different CMD regions map different epoches of SFR.

In particular, it is interesting to check how the variation of the absolute magnitude limit, in general fixed by observational completeness and chosen maximum distance from the Sun (50-80-100 pc) changes the possibility to recover the SFR. The figures 4.12(a), 4.12(b), 4.12(c) show this for different assumptions on the absolute magnitude limit.

If this limit is set to $M_V = 2.5$ we discover that only stellar masses higher than $1.6\,M_\odot$ map the recent 2.5 Gyr of star formation, following the paradigm that more massive is a star the higher is the probability it is young. On the other side of the mass spectrum, lower masses map different periods of star formation, but never the recent SFR. The explanation comes from the limit $M_V = 2.5$: it cuts the main sequence, so for stars below $1.6\,M_\odot$ we see only late evolutionary phases as the RGB and the central helium burning. In other words, enhancing the minimum luminosity of the sample we miss low mass stars or, in the best situation, we see only the RGB and the He burning phases.

Enhancing the limit at $M_V = 3.5$, we discover that each mass above $1.2\,M_\odot$ is included in each period of star formation up to ~ 7 Gyr ago. At this magnitude limit we cannot see the main sequence for masses below $1.2\,M_\odot$. As result this mass range give informations on the old SFR through RGB and He burning stars, but not on the recent one.

At $M_V = 4.5$ we see all the main sequence down to $1\,M_\odot$, so we can analyse with this mass range each period between today and $10 - 12$ Gyr ago.

The specific results we have reached depend on the assumed prescriptions, in particular the chemical composition (besides the hypothesis of flat SFR). Changing metallicity, for example lowering Z, accelerates the stellar evolution and the analyzed regions of CMD leads to different information on the SFR. Anyway, this type of analysis can be useful when we will approach to real data, where ages and masses are unknown. The first natural refinement of the theoretical model is to introduce an age-metallicity relation. This law plus the SFR will allow to weight the CMDs obtained with a single chemical composition.

The comparison between the artificial diagram generated with solar composition and the real data (see figure 4.6) shows the limits of our simplicistic assumptions. In particular differences on the low main sequence and in the red clump region are evident. The theoretical main sequence is too much narrow with respect to the observed one. The theoretical clump reproduces the features discussed in the previous section for a given chemical composition while in the observed one the stars occupy an elliptical region (and they are systematically blue shifted). Thus the inclusion of stars with different chemical compositions seems to be a key parameter for the comparison with the observed CMD.

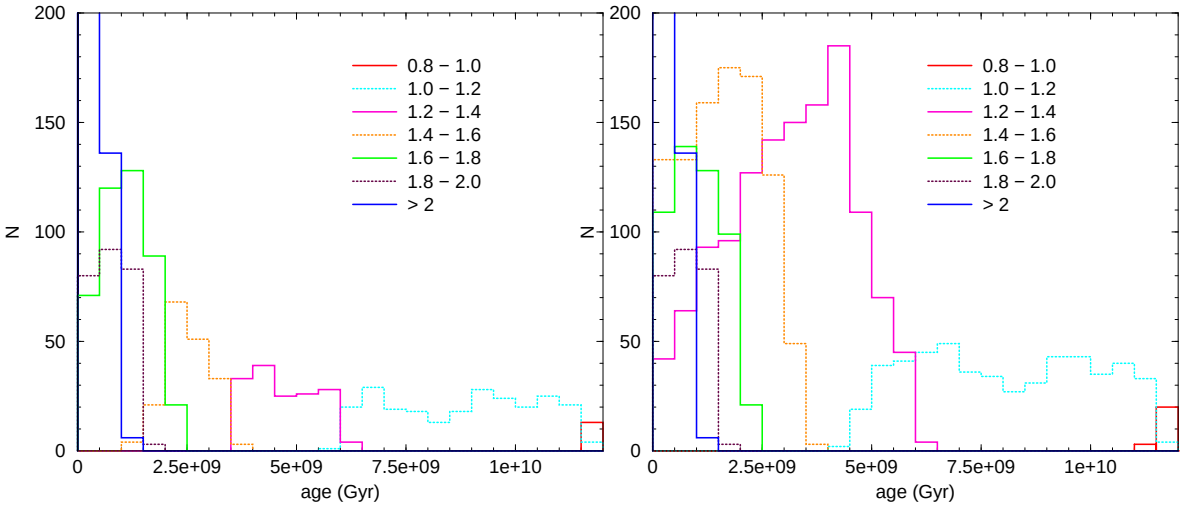

(a) Stars with $M_V < 2.5$.

(b) Stars with $M_V < 3.5$.

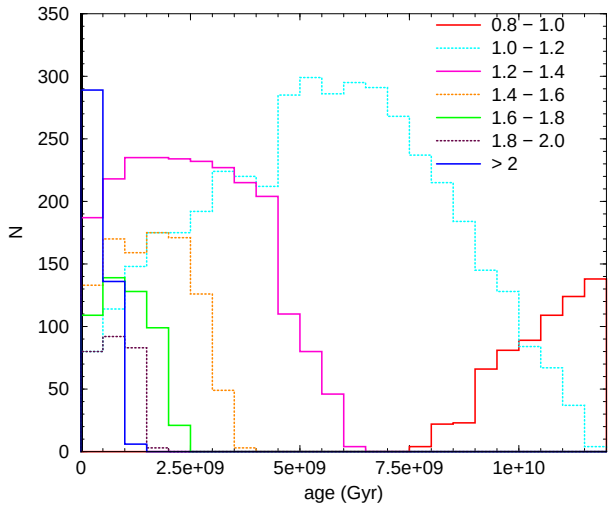

(c) Stars with $M_V < 4.5$.

Figure 4.12: Theoretical distributions in time of stars generated with a flat SFR (0-12 Gyr), Salpeter IMF and solar composition. In different colors are indicated different mass ranges. In figure (a) only stars with visual absolute magnitude below 2.5 are plotted, while in figure (b) and (c) this limit is respectively $M_V = 3.5$ and $M_V = 4.5$.

As an example, the figure 4.13 shows a set of artificial CMDs obtained with different chemical compositions. Using the fiducial line obtained by Nordström et al. 2004 (see figure 1.8(a)) and adding the observational spread (figure 1.8(b), we obtain the artificial CMD shown in figure 4.14.

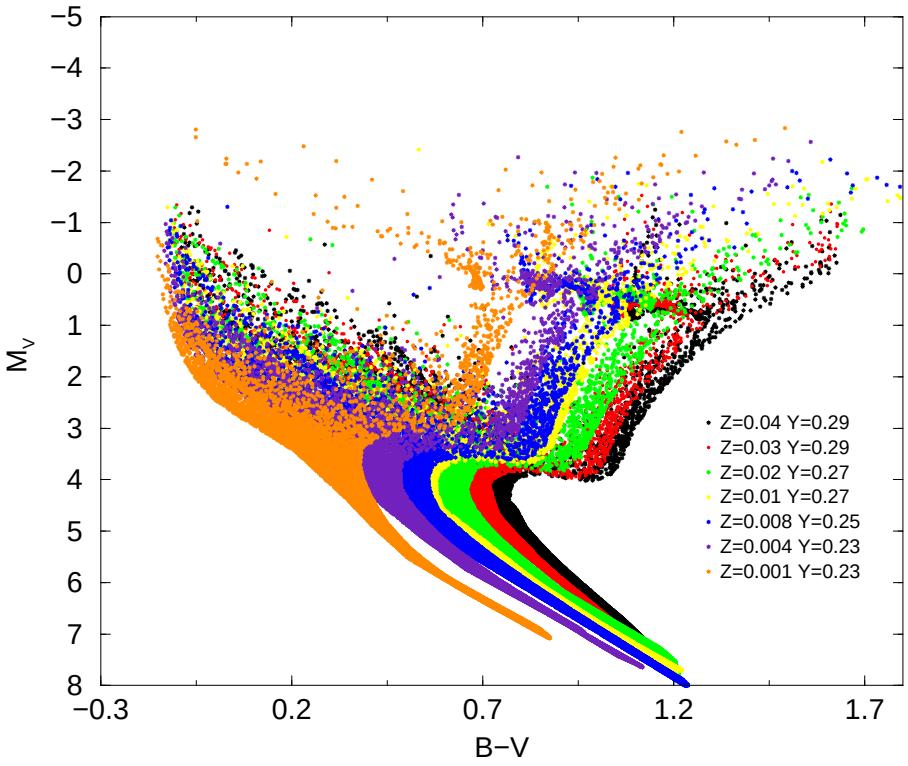

Figure 4.13: The effect of chemical composition on the artifi cial CMDs. The explored range goes from Z=0.001 to Z=0.04.

Now the artificial main sequence approximates much better the width of the observational one (it is worth to notice that the theoretical model does not include the observational errors). The red clump has assumed an elliptical shape, without the single metallicity signatures (hook) and covering the observational color extension. In this section we do not take into account the secondary differences between theory and observation (most of them coming from the assumed flat SFR), but we only would like to discuss the general characteristic needed to obtain a first order agreement with observations.

4.3.1 Red clump discrepancy

The most striking discrepancy is the luminosity excess of the theoretical red clump stars with respect to real data (figure 4.16(a)). The problem of the overluminosity of the theoretical helium burning stars (mainly for stars with a degenerate helium core in the RGB phase, $M \lesssim 2.3\,M_{\odot}$) is well known. In particular, it is striking when one uses evolutionary codes with updated physical inputs (see Pols et al. 1998, Castellani et al. 2000).

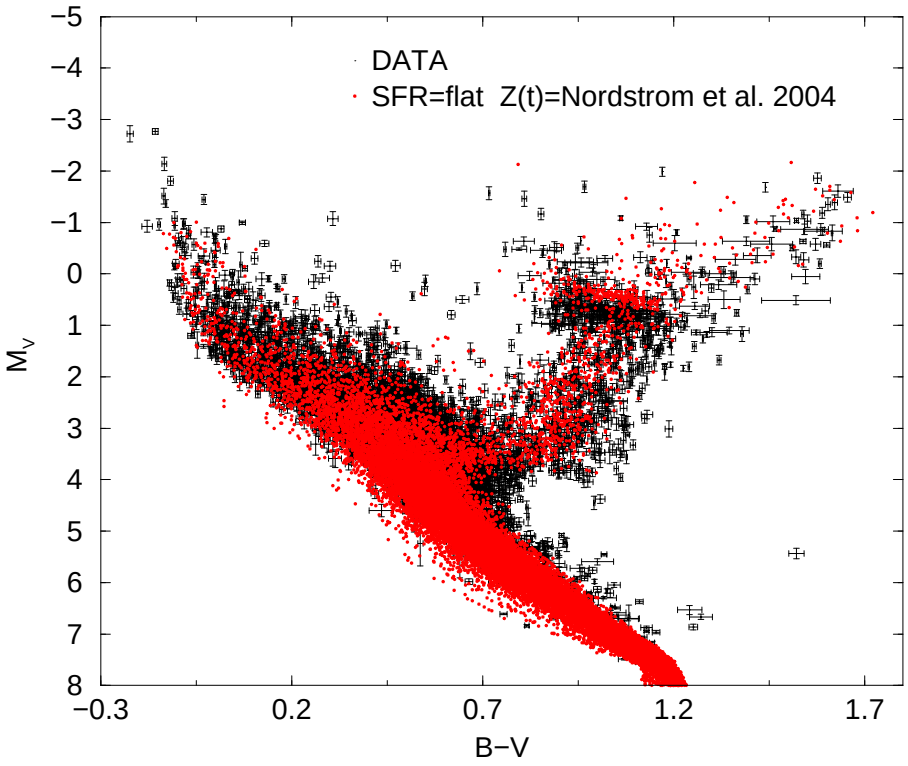

Figure 4.14: Artificial CMD generated with a flat SFR and Z(t) sampled from Nordström et al. 2004, superimposed to Hipparcos data.

However, if one uses evolutionary tracks computed with less updated inputs (as the Padua tracks) the observation is better reproduced (see Salaris & Girardi 2001).

Possible solutions could be searched among;

1. simple evolutionary effects, from the simple consideration that different masses reach the red clump phase in different ages. In particular, for a fixed metallicity we have seen that the minimum luminosity among clump stars is for masses of about $\sim 2.2 - 2.5 M_{\odot}$. Increasing the star formation in epoches comparable with time these stars need to ignite central helium burning would imply to lower the red clump mean luminosity;

2. problems in the atmospheric models adopted to translate theoretical predictions in the observational plane. In fact clump stars are low temperature stars and thus subject to higher uncertainties in the corresponding atmospheric models;

3. physics of convective cores (overshooting problem);

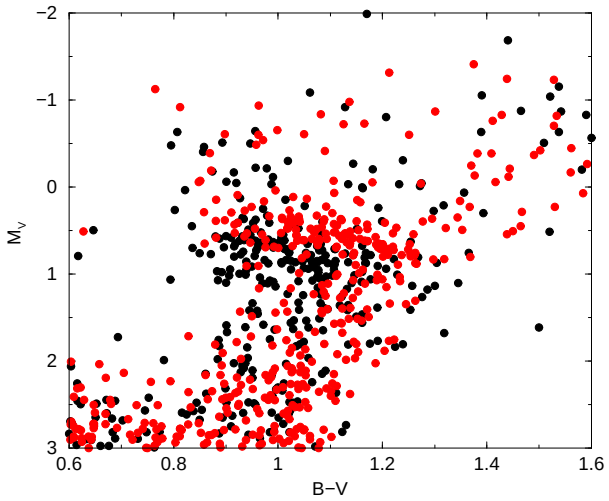

(a) Flat SFR

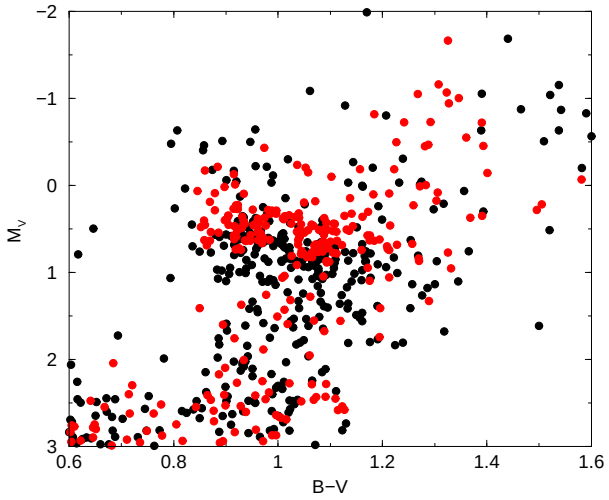

(b) Recent burst at 0.8 Gyr

Figure 4.15: Black circles represent Hipparcos stars. Red circles are artifi cial stars. Panel (a) and (b) show simulations respectively with flat and bursty (0.8 Gyr ago) SFR.

4. the presence of an hypothetical strong mass loss during the red giant phase;

5. uncertainties in the physical inputs inputs in the calculations (plasma neutrino emission, conductive opacities, etc..).

For completeness, I will shortly discuss the previous points, without any claim to solve the problem. First of all I tuned the star formation, increasing the rate between 0.5 and 0.8

Gyr ago (the idea is to increase the number of clump stars with the lowest luminosity, and 0.8 Gyr is the time needed for a $\sim 2.4 M_{\odot}$ to reach the clump). As expected (see figure 4.16(b)) the theoretical mean luminosity of the clump is lowered, even if the agreement with observations is still not reached.

From the point of view of the atmospheres, figure 4.17 shows a color-color diagram ($B-V$ against $V-I$) for a set of artificial clump populations computed for different chemical compositions, compared with Hipparcos data (obviously this sample will include also a fraction of red giants, un-distinguishable by red helium burning stars). It is evident that the theory does not cover the red part of the diagram, letting room for the hypothesis of problems in the adopted theoretical atmospheres. However, the comparison in $(V, V-I)$ plane (see figure 4.16) does not give a clear improvement.

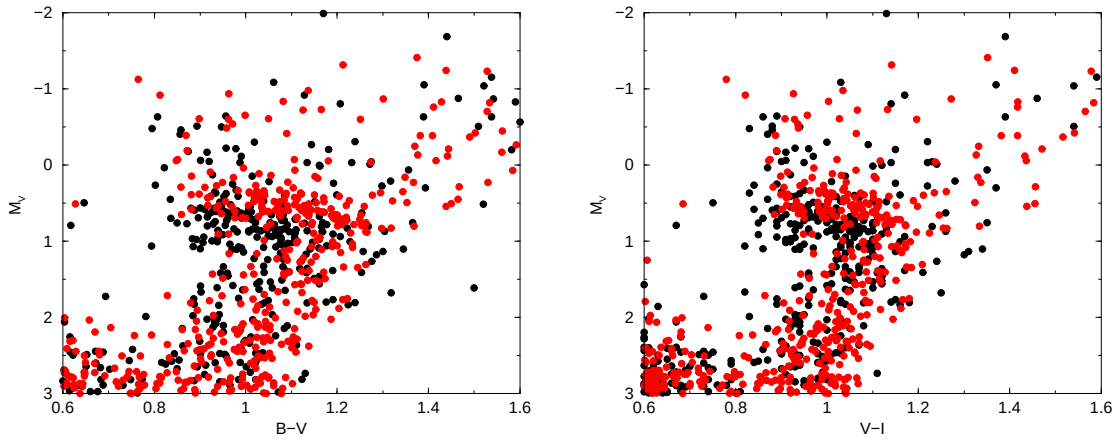

(a) (b)

Figure 4.16: A selection of Hipparcos data with absolute magnitude errors less than 0.1 mag is compared with artifi cial populations (flat SFR). (a) M_V against $B-V$. (b) M_V against $V-I$.

Overshooting problem: stars with $M \gtrsim 1.1\, M_{\odot}$ have convective cores and the size of the mixed core determines the structure of the star and the fuel available for its evolution. Thus, the penetration of convective motions (overshooting) beyond the Schwarzschild boundary* into the surrounding layers, affects the internal structure of stars and enlarges the chemically mixed regiones, which changes the subsequent evolution of the star. The predicted extent of the overshooting is parametrized in general in fractions of the pressure

*the Schwarzschild criterion locates the point where the convective bubbles are no more subjected to the buoyancy force (see e.g. Kippenhahn, R., Weigert A. 1990, "Stellar Structure and Evolution").

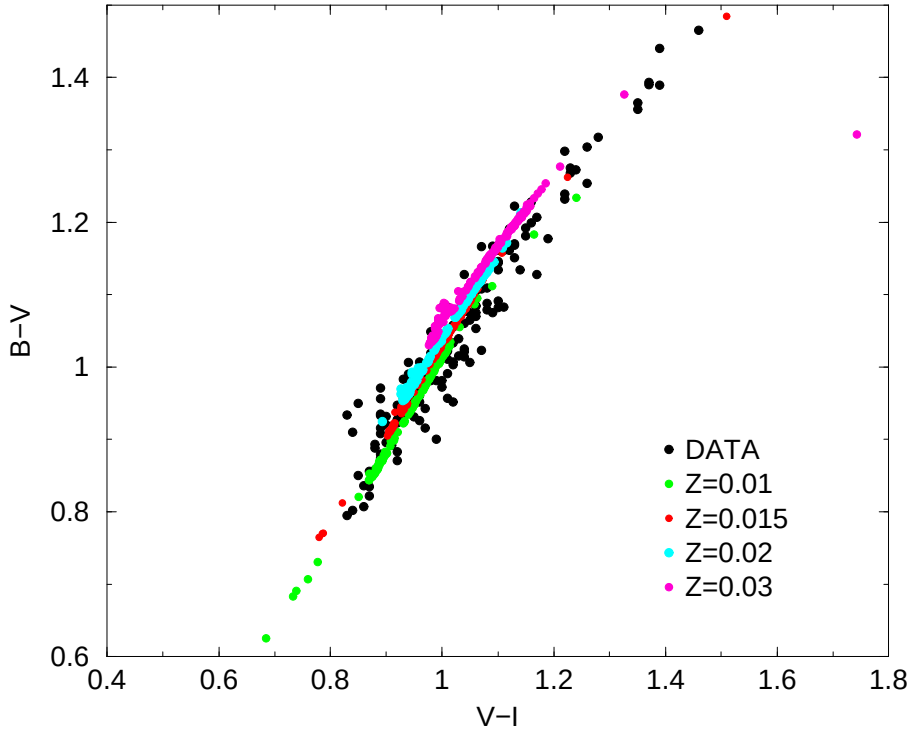

Figure 4.17: Artifi cial populations of clump stars for different compositions superimposed to real data.

scale height H_P (measured in our code from the border of the Schwarzschild convective region). Several comparisons between cluster data and theoretical CMDs indicate as upper value an intermediate amount of overshooting ($l_{OV} = 0.2 - 0.3\, H_P$; see e.g. Chiosi 1989, Chiosi et al. 1992, Girardi et al. 2000, Pols et al. 1998). In case of overshooting, the resultant effect is more hydrogen available (more massive H convective core) and thus the stars stay on the main sequence for a longer time reaching an higher luminosity. The influence of overshooting on an evolutionary track of $2\, M_\odot$ is shown in figure 4.18; it is evident the higher luminosity of the H exaustion for the model with overshooting.

The increased helium core at the end of the main sequence phase determines, for this mass, a lower luminosity of the He burning phase (see figure 4.18). In general the luminosity of the stars at the beginning of the central He burning phase (zero age He burning models) as a function of the total mass of the stars follows the one of the He core at the central H exaustion.

Figure 4.19 shows the luminosity of the zero age burning models as a function of the stellar mass for different overshooting values according to different authors (which

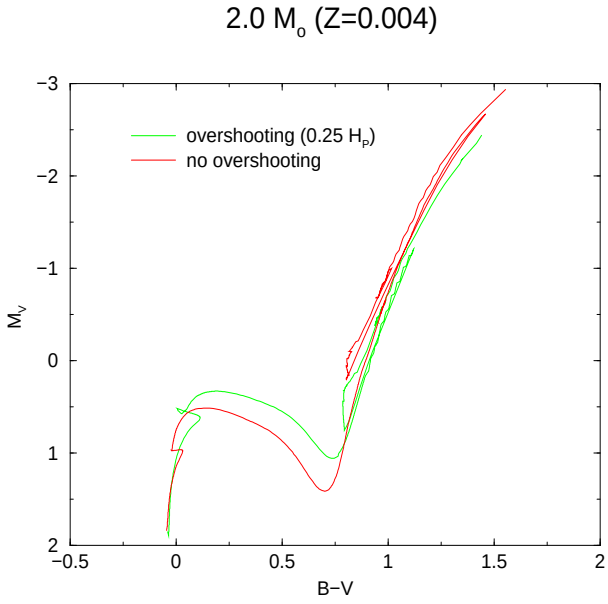

Figure 4.18: Evolutionary tracks ($2\,M_{\odot}$, $Z = 0.004$, $Y = 0.23$) with different assumptions of overshooting: red line is without overshooting, green line is calculated with an overshooting scale lenght of $0.25\,H_P$.

implement different physical inputs): the Girardi et al. (1998) tracks with and without overshooting, the Bressan et al. (1993) models with overshooting and the the Castellani et al. (2000) (the stellar tracks used in this work) calculations without overshooting. Even if the models with overshooting are underluminous compared to the Castellani et al. (2000) stellar tracks, one sees that for masses lower than $\approx 1.8\,M_{\odot}$ the influence of the overshooting on the He luminosity is very small or even negligible (compare the stellar tracks by Girardi et al. (1998) with or without overshooting), while the Hipparcos clump is populated by the whole mass range (see figure 4.9). The presence of overshooting could thus contribute to reduce the discrepancy between theory and observation for the clump luminosity but it cannot be the unique solution of the problem because it affects only a fraction of the masses which populates the clump region (see e.g. Castellani et al. 2000).

The problem of possible strong RGB mass loss is discussed in the literature (see Castellani & Castellani 1993). Mass loss in red giant phase has a differential effect according to if the star develops a electron degenerate core or not. In the first case (masses lower than $1.5\,M_{\odot}$), the mass of the helium core, which determines the luminosity during helium burning, is independent by the original mass and it is not affected by mass loss. The only effect of mass loss is to change the surface temperature during central

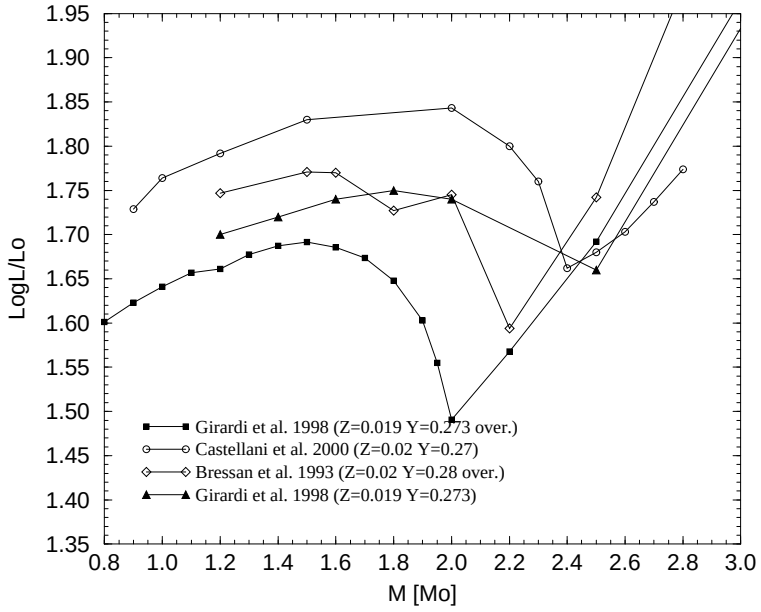

Figure 4.19: The luminosity of zero age He burning models with $Z \approx 0.02$ and $Y \approx 0.27$ as a function of the stellar mass, according to various authors (with or without overshooting).

helium burning, because the envelope mass changes the efficency of the hydrogen shell. For larger masses, the size of the helium core depends by the original mass of the stars, because it depends on the extension of the convective core during the main sequence evolution. As for low mass stars, the helium core mass is not affected by mass loss but, unlike low mass stars, a change in the envelope brings different luminosities in central burning phase. Under the light of the observed data-theory discrepancy (we observe larger discrepancies in the red part of the clump, that is populated by low mass stars), it seems difficult that mass loss could solve the problem (with low mass stars luminosity essentially unaffected). The last possible candidate to fill the gap between data and theory could be the input physics of degenerate cores which are affected by uncertainties which in some cases are difficult to be precisely evaluated (see e.g. Castellani & Degl'Innocenti 1999, Castellani et al. 2000). For example the results are sensibly affected by the adopted rate of plasma neutrino emission and the electron conduction opacity. However the problem, which is out of the purposes of this thesis, is still open.

4.4 Binary stars

The inclusion of binary stars is the final needed ingredient to make an artificial population close as soon as possible to real data. It is well known that the presence of equal mass main sequence binaries produce a second main sequence in the color-magnitude diagram of a stellar cluster (each binary system has the same color of a single star but twice luminosity), but this feature observed in open clusters is too much often used to conclude that the observed double main sequence of many cluster is the result of equal mass binaries. In reality several authors (see e.g. Hurley et al. 1998) have shown that, depending of the mass of the primary, also mass ratios different by one leads to a second main sequence (clearly separated from the main sequence). It is well known that binary systems exist, but unfortunately, because of the selection effects that govern the observations, one poorly knows which is the statistical distribution of the mass ratio $q = M_{SECONDARY}/M_{PRIMARY}$ (see e.g. Mazeh et al. 2003). For the same reason, also the fraction of binaries present in the solar neighborhood is unknown.

So, I will not assume a particular q distribution, but for a given percentage of single stars I will add a secondary star, whose mass is a random fraction (between 0 and 1) of the primary.

The figure 4.20(b) shows an artificial CMD generated with 50% of stars in binary systems and random mass ratio. The changes in the CMD morphology when it is compared with a single star population color-magnitude diagram are evident (fig. 4.20(a)): the presence of binaries affects overall the low main sequence (doubling the main sequence) and it produces a stellar over-density close to the equal mass binary main sequence (see figure 4.20(d)) (as claimed by Hurley et al. 1998). Clearly the effect is so evident in our simulation not only because the selected fraction of binaries is high but also because we adopted only one chemical composition. In the real CMD the spread of the MS due to the presence of binaries can be hidden by the spread due to the presence of different chemical compositions.

Only to show an extreme situation, in figure 4.20(d) we present a simulation where the binary population is composed by twin star only: in this case, each evolutionary phase shows a double sequence.

Seen in a different way, the CMD spread due to binaries could mimic a metallicity (or

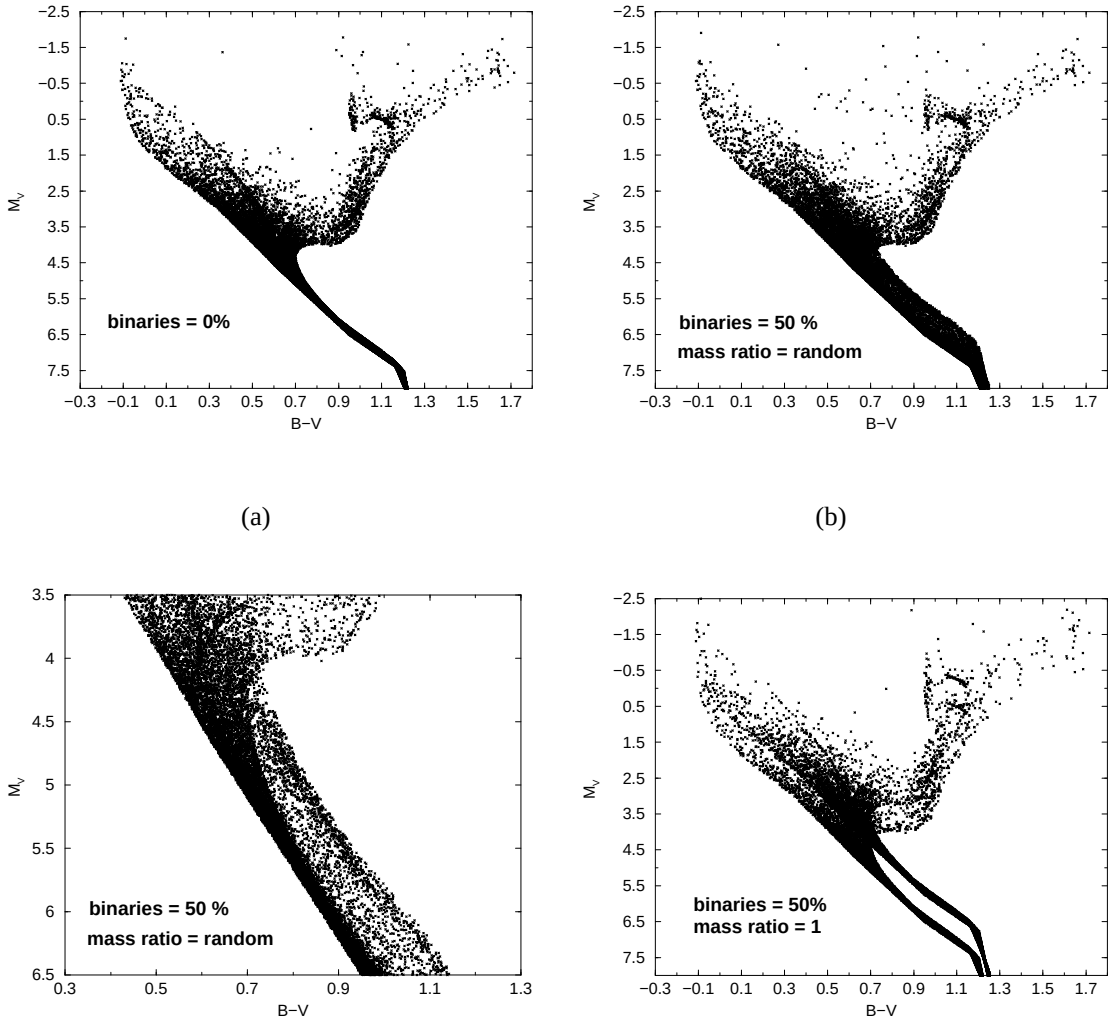

Figure 4.20: Artificial CMDs with only one chemical composition: (a) Population of single stars, (b) Population where the 50% of stars is in binary systems with random mass ratio, (c) As (b) but only low main sequence is shown, (d) Population where the 50% of stars is twin.

age) effect. Putting together a primary star with a smaller secondary star gives a system redder than the primary. The same effect could be produced by using an older primary alone (as well as a more metal rich primary alone). However, how we will see better in the chapter 6, the degeneracy binary-age is not so important, as long as we look at stars more massive than the Sun: the evolutionary times are short enough that the maximum spread caused by binaries in the CMD should correspond to a short time interval. In fact, during main sequence, a $1.2\,M_{\odot}$ takes less than 2 Gyr to cross 0.2 mag in $B-V$. This

time is reduced if we consider more massive stars or later evolutionary phases.

Figure 4.21 shows an example of the degeneracy binaries-metallicity: one population is generated using the age-metallicity scatter plot as derived by Nordström et al. 2003, the other population has a single metallicity (the mean value of the Nordström et al. 2003 dataset) but 80% of binaries with random mass companion.

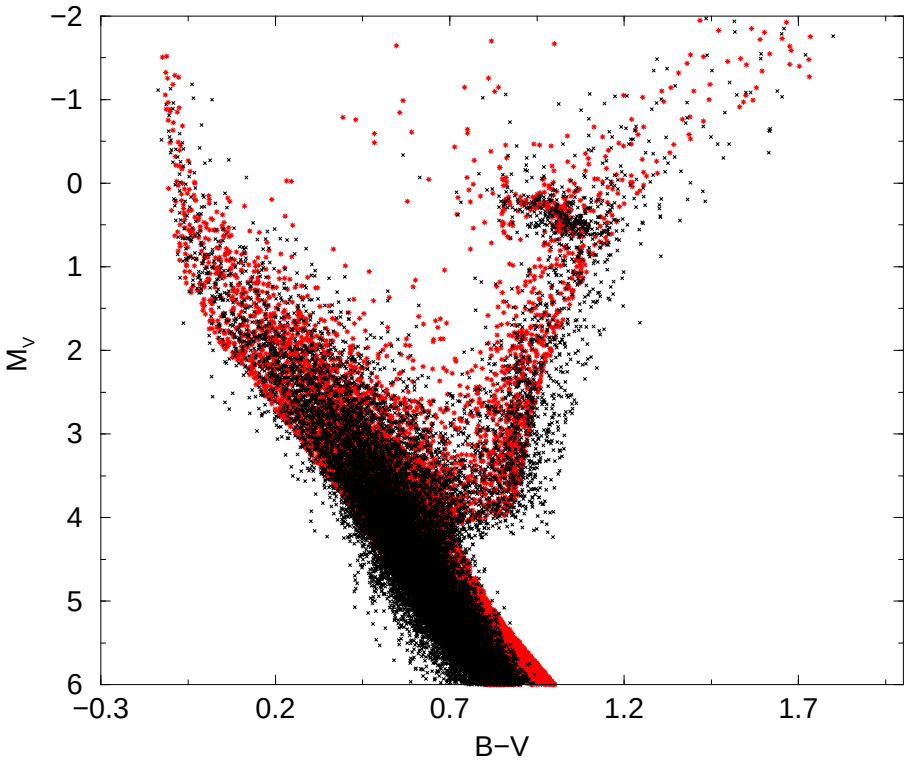

Figure 4.21: Red dots represent a population generated with the age-metallicity scatter plot as derived by Nordström et al. 2003. Black dots represent a population with $[Fe/H]$ equals to the mean value of the Nordström et al. 2003 dataset and 80% of binaries with random mass companion.

As conclusion, the fraction of binaries is important if one try to recover the age-metallicity relation, but it is not so important to recover the star formation rate (at least for the recent SFR).

5

RL algorithm applied to color magnitude diagrams

5.1 Introduction

The color-magnitude diagram (CMD) is the key tool for studying evolution in stellar populations. However, in order to extract physical parameters as the IMF or the SFR, it is necessary to account for observational uncertainties. There are two types of approach: in the first, the observational uncertainties are incorporated in the models and the data is directly compared with the "modified" theory. The alternative technique is to "clean" the data and decrease the statistical uncertainties in the observed color-magnitude diagrams.

An example of the first statistical treatment is the Bayesian inference scheme proposed by Tolstoy & Saha (1996). Here, each model point (apparent magnitude and color) is replaced with a box with a Gaussian distributed probability density (the photometric error). The total likelihood of a model is the product of the probabilities to observe the data in each box. The idea of this method is equivalent to use blurred isocrones (each point is weighted by the Gaussian spread), so that the photometric uncertainty is embodied in the theoretical model.

Following the second approach, the present work explores the possibility to eliminate the observational uncertainties from the data.

In order to unravel the star formation history of the solar neighborhood, I explore how to obtain a cleaned input for such analyses, that is a restoration of the intrinsic distribution to the limit of the errors.

In effect, a CMD is an image, the intensity being the number of stars in a bin of effective temperature and luminosity, affected by a point spread function (*psf*) that originates from the error distributions of the parallaxes. With this as our assumption, we propose to treat it with the same techniques that have been used for image restoration. This technique wants to be an alternative way to take into account the observational uncertainties: the correction is directly applied to the data, in a fashion that is reversed respect to the usual way to work (spreading the theoretical CMD).

5.2 The Richardson-Lucy algorithm

In this chapter I will describe the adoption of the Bayesian Richardson-Lucy algorithm (for details see the chapter 2) to "clean" observed CMD from the "confusion" due to observational uncertainties. This method is very well known in the astronomical community, in particular for the restoration of astronomical images (see, e.g. Bertero & Boccacci 2005 and references therein), but this is the first time that it is applied to the study of color-magnitude diagrams.

If we grid a CMD by building a two dimensional histogram in, say, M_V and $B-V$, the data is an image blurred by a *psf* that is the matrix produced by the observational errors. The analysis then becomes a deconvolution problem. From this point of view, the loss of information about single stars is balanced by the opportunity to analyze the sample data in a statistical sense using imaging methods. Our intent is to recover, as closely as possible within the limits of the *psf*, the intrinsic CMD for comparison with theoretical predictions.

To verify the usefulness of the RL-algorithm to recover color magnitude diagrams I blurred artificial CMDs mimicing the Hipparcos data and then I applied to the result the RL-algorithm. As I will show, comprehensive experiments demonstrate the successful image restoration under various *psf* assumptions. Finally the method is applied to observational data for the Hipparcos field.

5.3 Modeling the observational error

Before applying our method to real data, it is necessary to test the capability in restoring CMDs on the basis of artificial data. I began by modeling the *psf* with a Gaussian. From the analysis of color and magnitude uncertainties in the Hipparcos sample (see discussion in section 3.6), the mean error in absolute magnitude is about $0.1\,\mathrm{mag}$ while the error in $B-V$ is negligible. In order to be as close as possible to real data, I adopted a Gaussian with $\sigma = 0.1\,\mathrm{mag}$.

5.4 Application of the algorithm to artificial data

The obvious advantage of using an artificial data is that the real distribution is known and thus it is possible to compare the estimates produced by the technique with this real distribution. Thus, I blurred an artificial CMD by means of the chosen *psf* and I tried to restore the original CMD with the RL-algorithm. The artificial CMD (fig. 5.1(a)) was generated with a Monte Carlo using a Salpeter IMF, a flat SFR and a chemical composition about solar. In order to avoid possible differences due to the statistical fluctuations, it contains approximately the same total number of stars of the Hipparcos sample (according to the selection of the chapter 3).

The figure 5.1(b) shows the digitalized version (displayed through a 2-D histogram), binned with a step of 0.05 mag both in color and in absolute magnitude (with this binning the *psf* width of 0.1 mag corresponds to 2 bins, thereinafter "pixels", of the histogram). The chosen bin size is a practical compromise: reducing the size causes too high statistical fluctuations (noise amplification is a real problem with iterative algorithms), larger values destroy CMD details. Moreover, this size avoids possible bin correlations due to the photometric errors. After the convolution of the artificial CMD with a Gaussian PSF (σ=2 pixels), I obtained the blurred CMD of figure 5.2.

After reading the blurred CMD and assuming an initial guess (the blurred image itself) the iteration cycle is started. Figures 5.4 shows the results of the restoration as a function of the number of iterations: it is evident that after ~ 50 iterations the restored image is very close to the original one. There is thus the need of a convergence criterion, that is a rule that stops the algorithm when further iterations do not improve significantly the

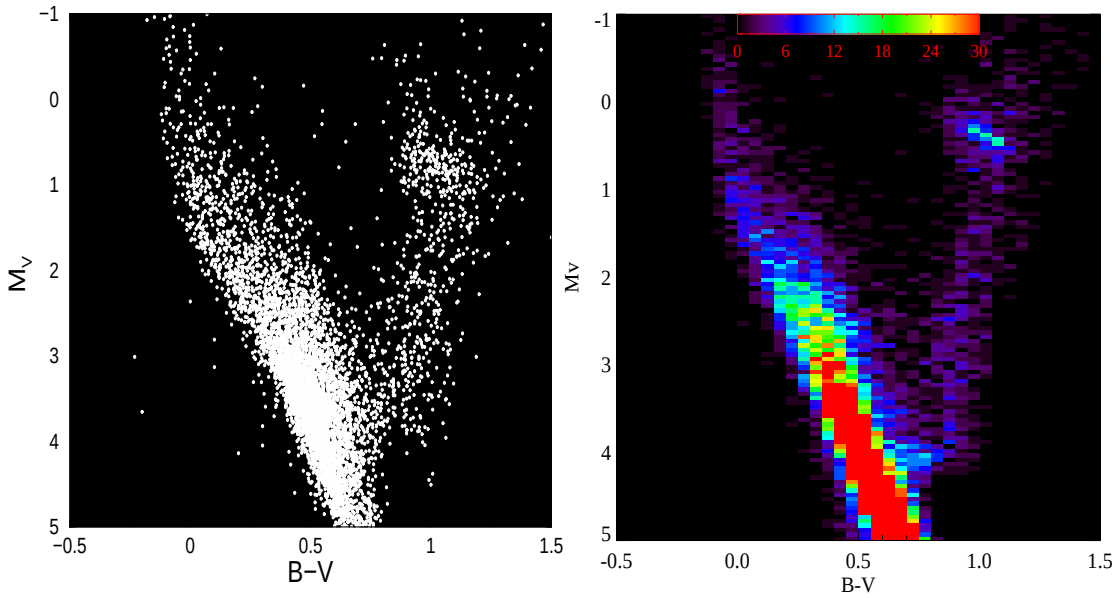

(a) (b)

Figure 5.1: (a) Artificial CMD. (b) 2-D histogram for the CMD; the number of stars in each bin is reported with a different color (according to the color bar on the top).

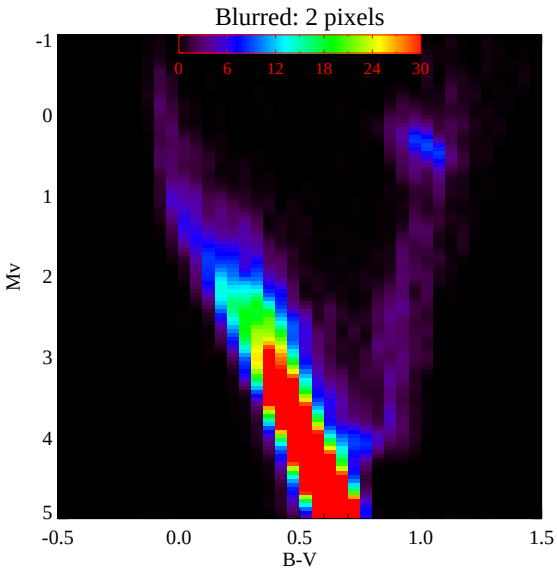

Figure 5.2: The 2-D histogram for the CMD of figure 5.1 blurred with a Gaussian *psf* ($\sigma = 2$ pixels).

result.

The most simple parameter that could give this information is a reduced χ^2 (Lucy 1974)

$$\chi^2 = \frac{1}{N}\frac{(\overline{\phi} - \phi_n)^2}{\phi_n} \tag{5.1}$$

where $\overline{\phi}$ is the blurred 2-d histogram and ϕ_n is the estimate of the observed 2-d histogram resulting after the iterations n. N is the number of pixels where the blurred image (the "data") or ϕ_n is different from zero.

The plot of the reduced χ^2 against iteration number (figure 5.3(b)) shows a decreasing monotonic trend, with a plateau reached after ~ 20 iterations. This result indicates that most of the restoration has been already obtained for such number of iterations. The most striking feature is the asymptotic value, much smaller than 1 and close to zero. This is due to the lack of noise in theoretical data: the artificial CMD has been convolved with a *psf, without noise addition*, so the R-L algorithm can perfectly recover the original CMD (leading to zero χ^2).

The idea to stop the iterations when the reduced χ^2 approaches to one cannot be applied in this case. Only an interpretation of the reduced χ^2 as a distance can be conserved (when the reduced χ^2 does not change anymore).

To better understand how the algorithm converges, I adopted a wider blurring function (*psf* with $\sigma = 6$ pixels, a value three times the previous case). The blurred image is shown in figure 5.5 and the relative reduced χ^2 in figure 5.6: after about 25 iterations, the χ^2 for the blurring 0.1 mag (2 pixels) and for 0.3 mag (6 pixels) converge to the same asymptotic value (that is, the algorithm works even in this case). The only difference is the rate of convergence: for the 2 pixels blurring the rate is higher.

5.5 Stability of the solution

5.5.1 Noise amplification

Until now, I discussed the deconvolution of blurred data without noise addition. An important point when one try to recover the underlying image behind noisy data is the sensi-

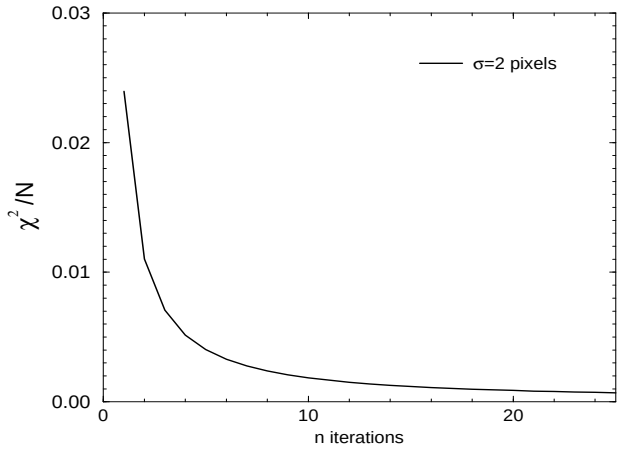

(a)

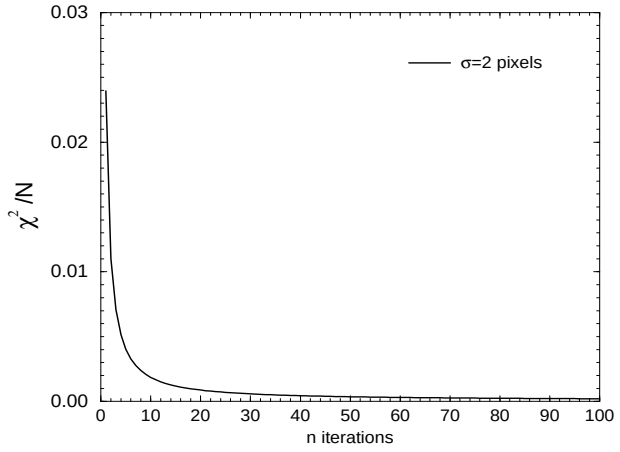

(b)

Figure 5.3: Reduced χ^2 computed for each iteration. The figures (a) and (b) show the same curve but respectively for the first 25 and 100 iterations. After $20-30$ iterations, the reduced χ^2 changes less than 10% of the initial value.

tivity to noise, which could be increased during the restoring process (resulting in output images with artifacts). The problem is that the convolution with a *psf* is a smoothing operation and, in the Fourier domain, it means to attenuate the high-frequency regions (responsible for the fine structure of the image). Methods like the R-L algorithm attempt to undo the smoothing, trying to amplify the high frequencies: this feature is also the weak point of the procedure, because of the noise that dominates at high frequency.

As already suggested by Lucy (1974), the estimate ψ^n of the real distribution do not

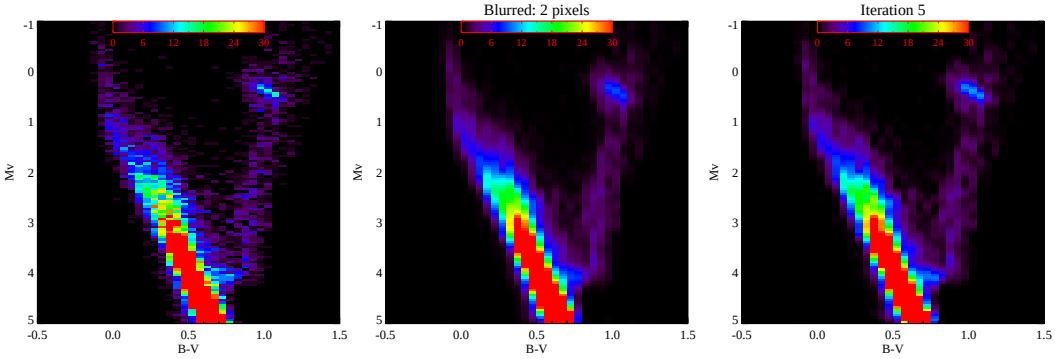

(a) Original image

(b) Blurred: $\sigma = 2$ pixels

(c) n=5

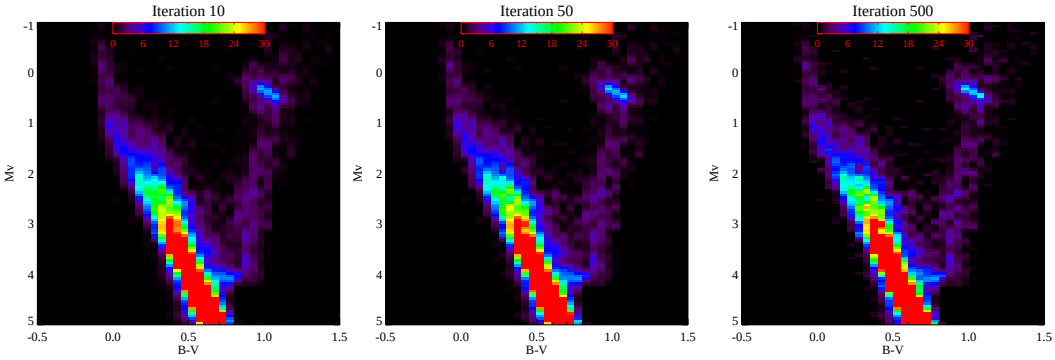

(d) n=10

(e) n=50

(f) n=500

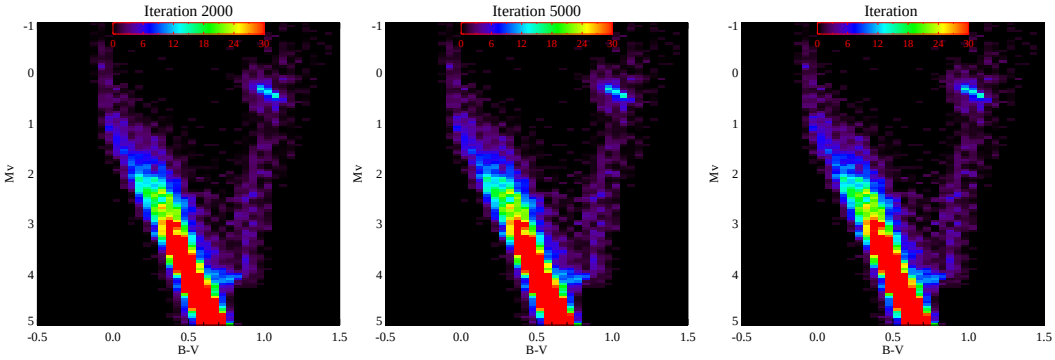

(g) n=2000

(h) n=5000

(i) n=10000

Figure 5.4: (c)-(i) The restoration results after the indicated number of iterations. The picture (a) shows the original image. The picture (b) the corresponding blurred image.

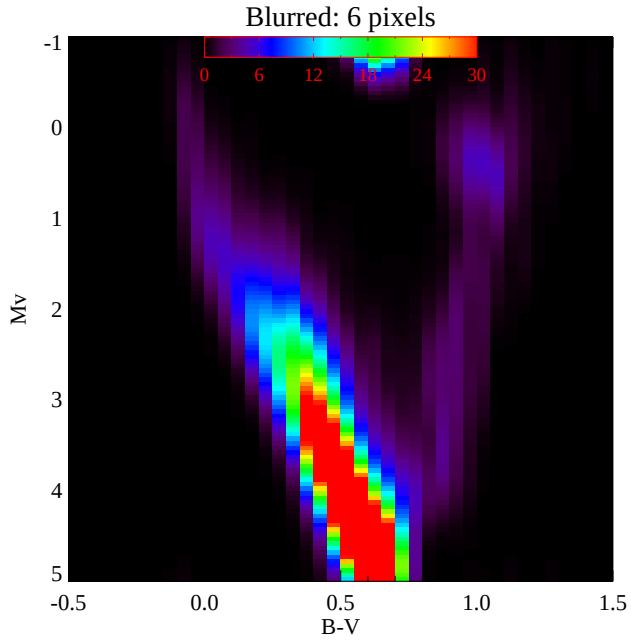

Figure 5.5: The artifi cial CMD of fi gure 5.1 blurred with a $\sigma = 6$ pixels Gaussian *psf*.

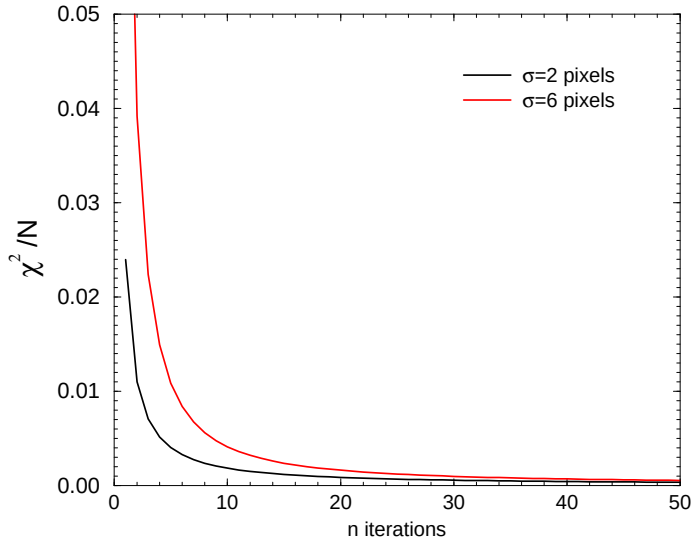

Figure 5.6: The χ^2 versus iteration number. The curve with star symbols comes from a Gaussian blurring with $\sigma = 2$ pixels. The curve with fi lled circles is the restoration from a Gaussian blurring with $\sigma = 6$ pixels. As expected, the deblurring with $\sigma = 2$ pixels is faster.

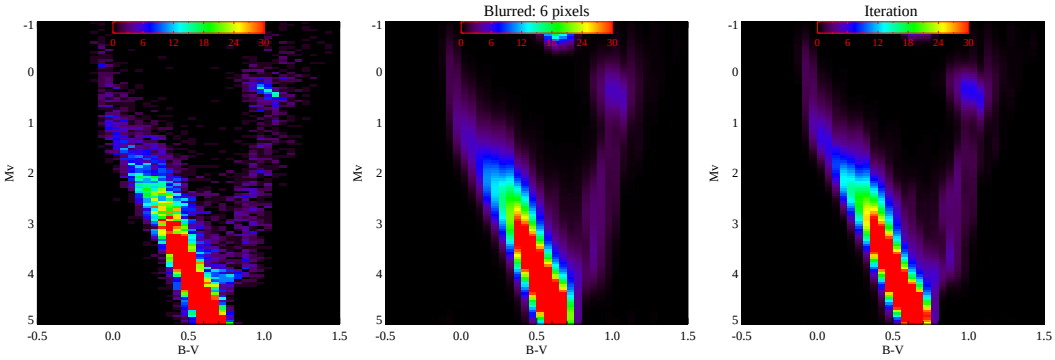

(a) Original (b) Blurred: $\sigma = 6$ pixels (c) 5

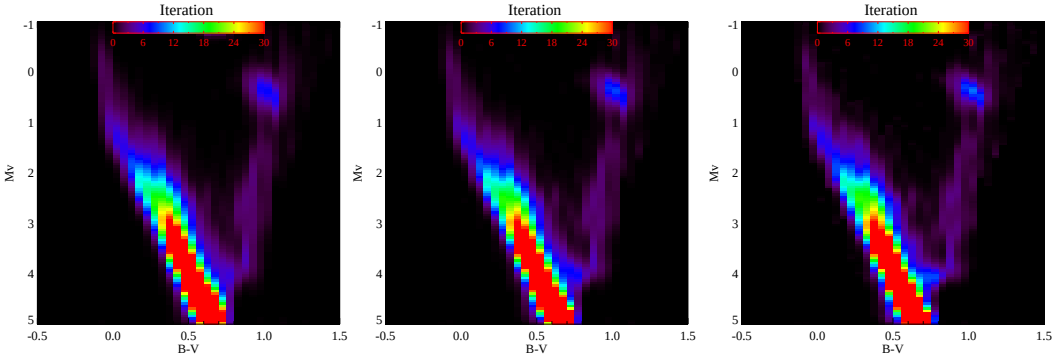

(d) 10 (e) 50 (f) 500

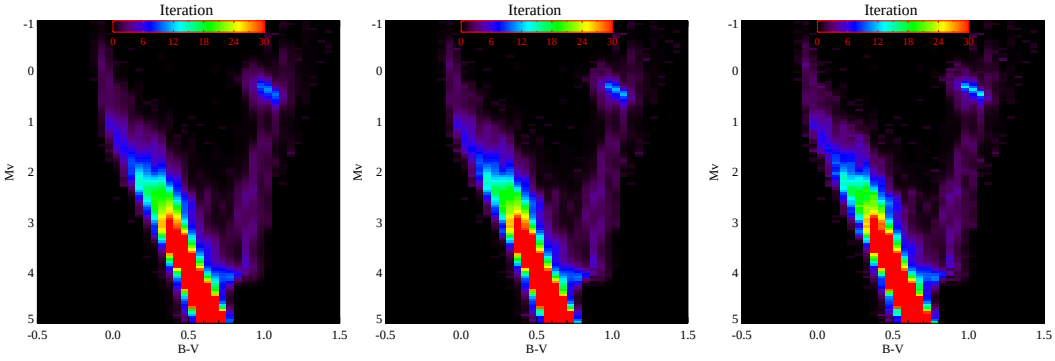

(g) 2000 (h) 5000 (i) 10000

Figure 5.7: As in Fig. 5.4 but for a blurring of $\sigma = 6$ pixels.

converge as $\psi^{n+1} - \psi^n \to 0$ as $n \to \infty$, in fact after a best estimate of $\psi^{\tilde{n}}$ the agreement get worse and artifacts could be generated (because of small scale fluctuations). The R-L algorithm is not regularized and when the iteration number increases the noise amplification appears in the solution. From a practical point of view, the iteration number could be limited to find an acceptable compromise between resolution and stability.

To test how the statistical uncertainties in the data can influence the deconvolved image, I blurred a CMD through a *psf* with a $\sigma = 2$ pixels and then Poisson noise was added (see figure 5.8). The restored CMDs are shown in figure 5.9. The result is very different from the case with pure blurring (compare with figure 5.4 and 5.7): the addition of Poisson noise represents a true limit and the original CMD is only partially restored. In particular, after about 20 iterations the deconvolved image takes a granular aspect, due to the noise amplification. Only the CMD regions with high signal to noise ratio give a better result: in this case, the CMD features are not buried by noise and the R-L algorithm is more efficient in restoring the CMD. The χ^2 is not sensitive to this problem. This is evident from figure 5.10 that displays the reduced χ^2 against the iteration number: this parameter is still dropping when, after about 20 iterations, many regions of the CMD are overcomed by the artifacts.

The main reason for this insensitivity comes from same χ^2 definition (equation 5.1): the numerator $(\overline{\phi} - \phi_n)$ is the difference between original data and the result of the n-th deconvolution, smoothed by the *psf*. So, it is insensitive to features in the CMD smaller than the *psf* width. Another reason is the global nature of the χ^2: it does not give informations on the local features (it is a sum over all pixels) while the noise amplification is a local trend. The regions with low signal to noise ratio, after an initial succesfull restoration, are slowly corrupted by noise amplification, but the χ^2 ignores them and it *over-weights* the regions giving the higher residuals $(\overline{\phi} - \phi_n)$ (like the main sequence). In other words, a decreasing χ^2 means that *the main sequence morphology is improving* and it is confirmed by the asymptotic value: in presence of noise, the reduced χ^2 converges very close to one (see figure 5.10). Obviously, also the noisy regions of the CMD are informative and must be preserved against corruption (e.g. the clump region and the high main sequence). Fortunately, the artifacts generation appears when the χ^2 changes are very littles. For our purposes, it is enough to stop the algorithm as soon as the χ^2 is quite stable to avoid the

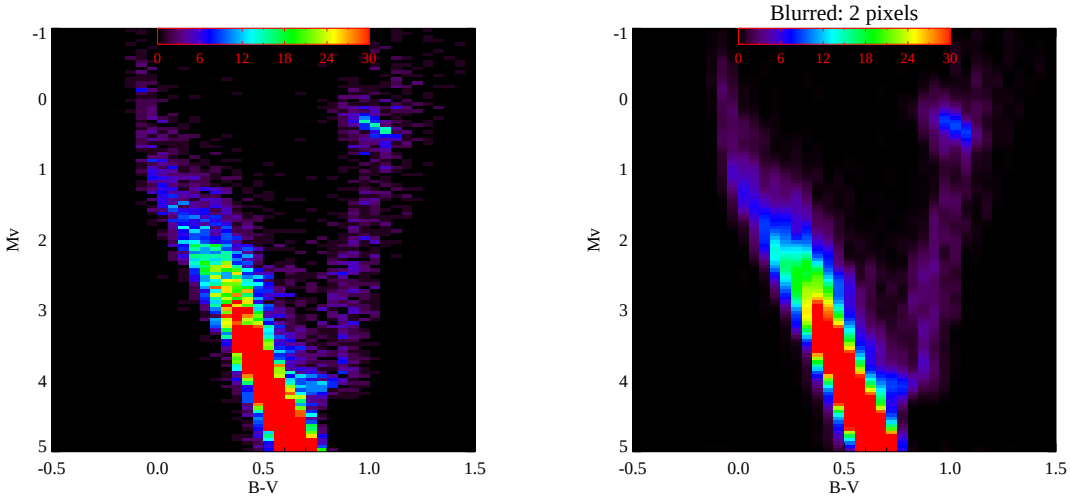

(a) Original

(b) After blurring

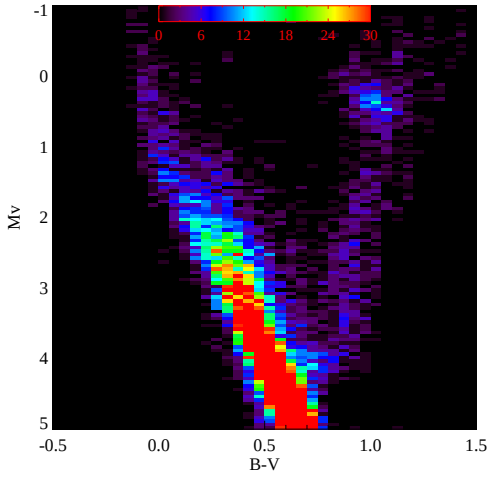

(c) After blurring and simulated Poisson noise

Figure 5.8: (a) 2-D histogram for the CMD, (b) 2 pixels blurring, (c) 2 pixels blurring plus Poisson noise.

artifacts regime.

5.5.2 Wrong *psf*

In this section I tried to test the effects of a wrong *psf* assumption. This situation is very common considering that the real blurring function is not a single Gaussian but it

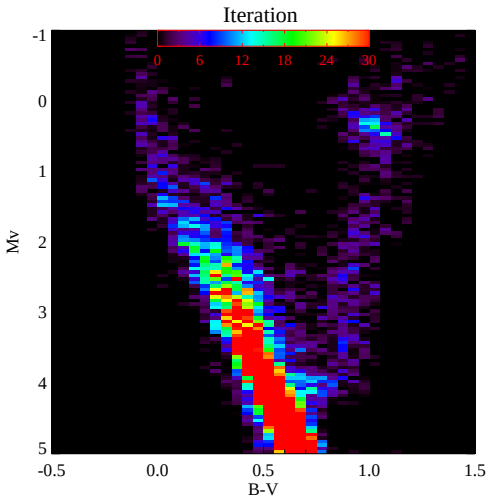

(a) 5 iterations

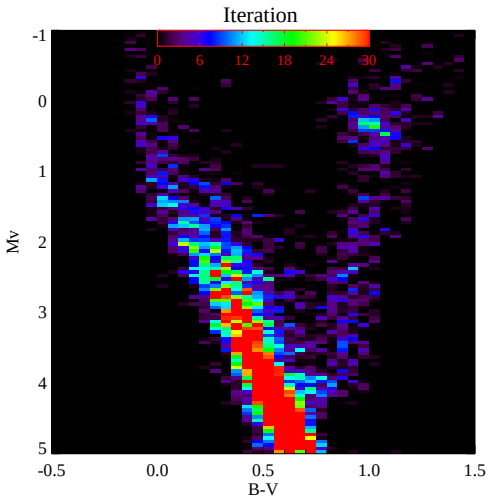

(b) 20 iterations

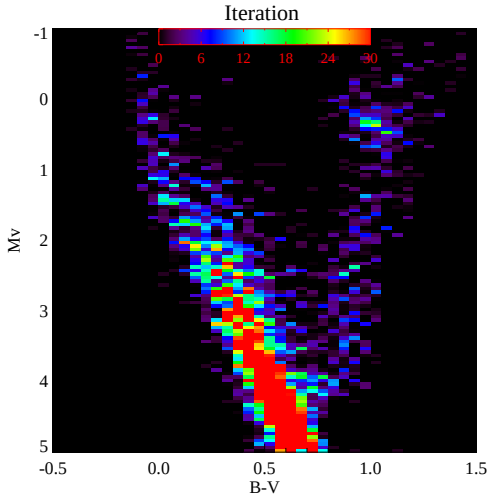

(c) 50 iterations

Figure 5.9: Restored 2-d histograms in case of blurring and noise addition. The number of iterations is labeled.

is a sum of many *psf* with different widths (see the error distribution in figure 3.5(a)). In this way, I blurred our CMD through a *psf* with a σ equals to 2 pixels and I tried to recover the original image using a *psf* with σ equals to 4 pixels. Figures 5.12 displays the restored image after respectively $7, 12, 16, 30$ iterations. Also in this case after some tenth of iterations the artifacts develop. The reduced χ^2 (figure 5.11) does not converge to

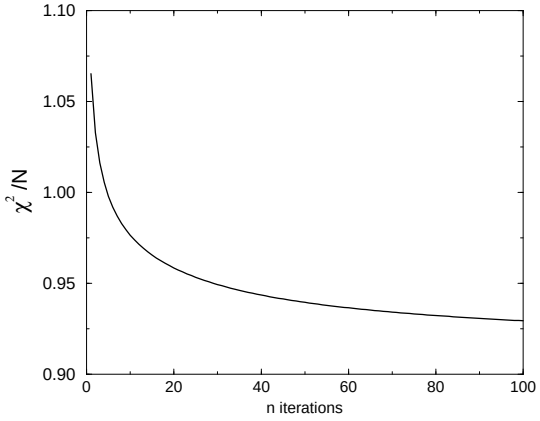

Figure 5.10: The reduced χ^2 versus iteration number (case with blurring and noise).

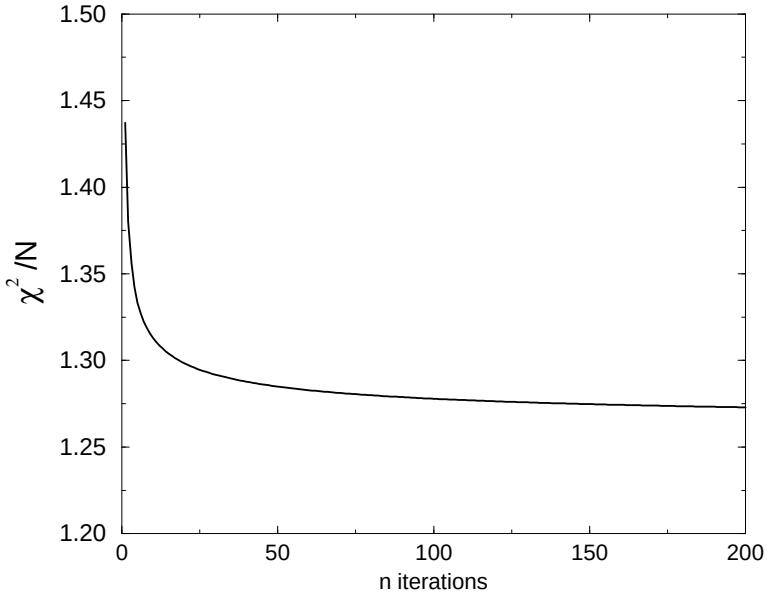

Figure 5.11: The reduced χ^2 versus iteration number for a deconvolution obtained with an over-estimated *psf*.

one but it stabilizes around a value slightly bigger. Also in this case, to avoid artifacts, it is enough to stop the algorithm after few iterations (the bulk of the restoration is anyhow reached).

5.6 Application to real data

As far as here, I tested the efficency (and the limits) of the R-L algorithm with artificial CMDs. However, analysing real observational data (figure 5.13), the first problem is the

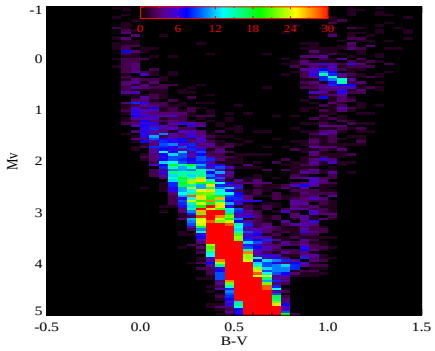

(a) Original.

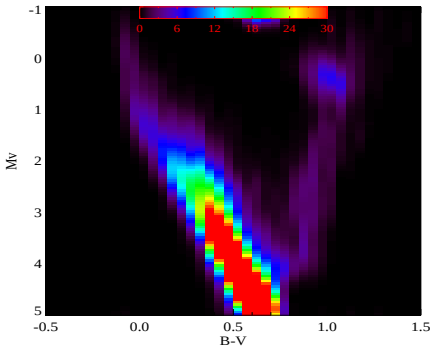

(b) Blurred with $\sigma = 4$ pixels.

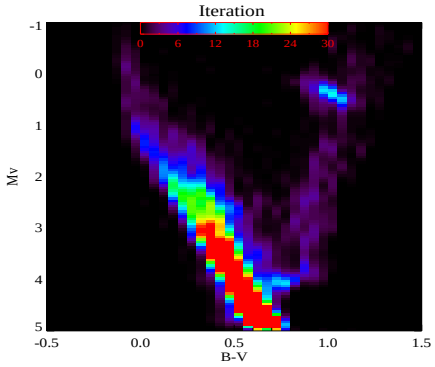

(c) 7

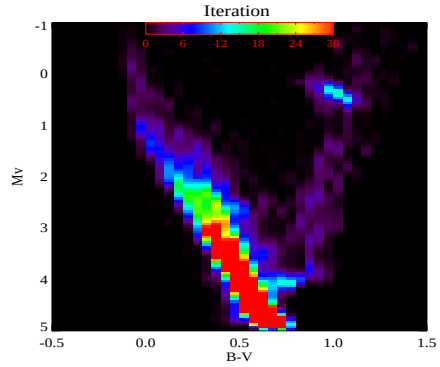

(d) 12

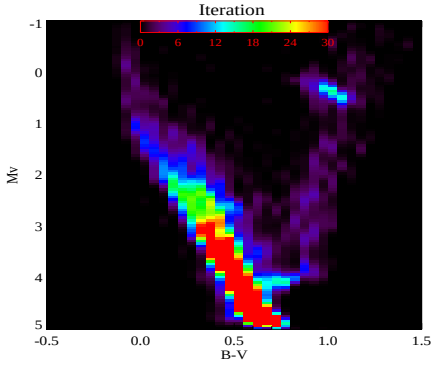

(e) 16

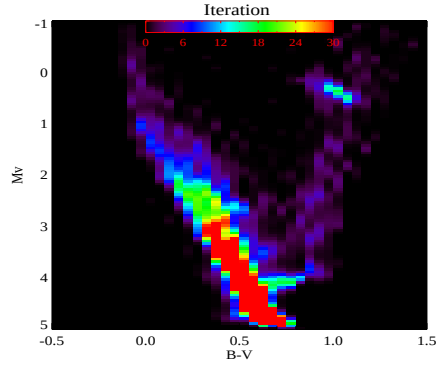

(f) 30

Figure 5.12: Deconvolutions obtained with an overstimed *psf* ($\sigma = 4$ pixels): after about 12 iterations, the Richardson-Lucy method amplifi es the noise (the main sequence becomes speckled).

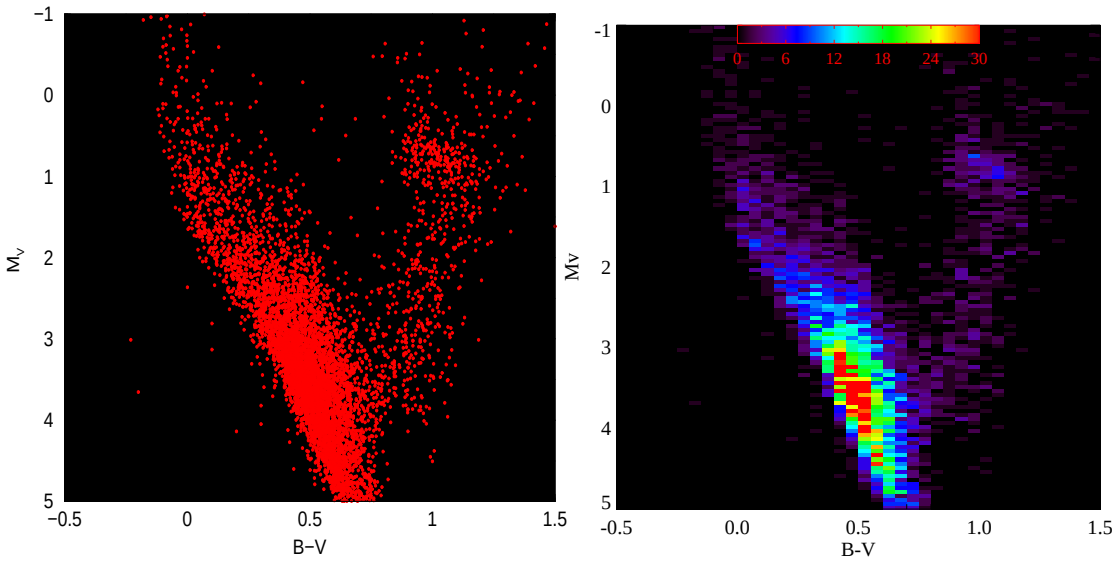

(a) Data (b) Data

Figure 5.13: (a) Hipparcos CMD; (b) 2-D Histogram for the Hipparcos CMD.

unavoidable presence of a *psf* characterized by a distribution of widths (see figure 3.5(b)); thus, in principle, I could not adopt a mean error ($\sigma = 0.1$ mag) as I did with artificial CMDs .

If I do not take into account this point and I blindly apply the algorithm with a Gaussian $\sigma = 2$ pixels large, the sequence of results is shown in figure 5.14.

The reduced χ^2 (figure 5.15) shows an asymptotic value equals to 1.27, very similar to the case with wrong *psf*. Moreover, after ~ 15 iterations, the speckles appear and local informations are lost.

A better result is obtained using the full information stored in the data error distribution, considering a *psf* formed by a linear combination of Gaussians:

$$g = \frac{1}{A} \sum_i \frac{1}{H_i} \frac{1}{\sigma_i \sqrt{2\pi}} \exp\left(\frac{-x^2}{2\sigma_i^2}\right) \tag{5.2}$$

where the A factor is a normalization constant, the weights H_i are the the histogram values of figure 3.5(b) (that is the number of stars with absolute magnitude error between $(\Delta M_V)_i$ and $(\Delta M_V)_i + \delta$), the σ_i are the values $(\Delta M_V)_i$.

The resulting *psf* is symmetric, narrower than a single Gaussian with $\sigma = 2$ pixels and it has tails that fall off more slowly than a Gaussian (see figure 5.16). Supplying this

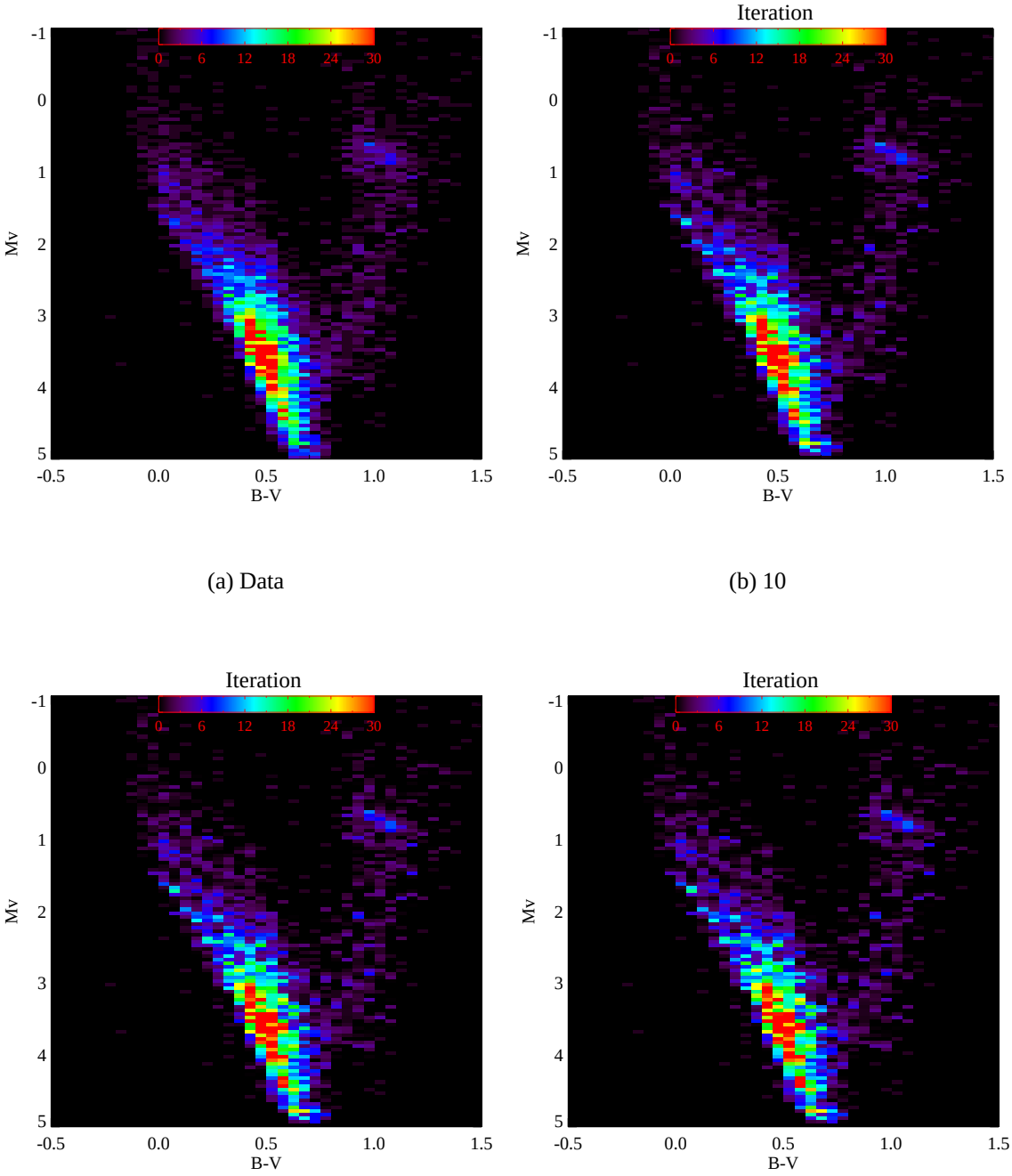

(a) Data (b) 10

(c) 15 (d) 20

Figure 5.14: Application of the R-L algorithm to the Hipparcos CMD. A Gaussian *psf* with $\sigma = 2$ pixels is used, see text.

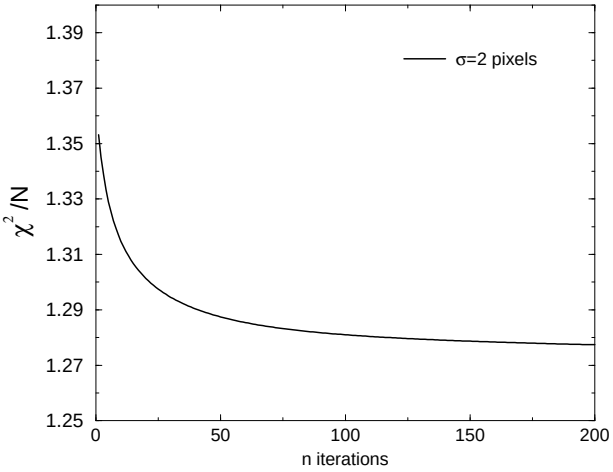

Figure 5.15: Reduced χ^2 against iteration for real data restored with a $\sigma = 2$ pixels Gaussian.

function to the R-L algorithm, I find the sequence restorations shown in figure 5.18. It is interesting to see that for, the same number of iterations, the new *psf* recovers many more details (compare e.g. the red clump region, at the 20-th iteration, as shown in figure 5.14(d) and in figure 5.18(d)).

Plotting the reduced χ^2 against iteration number (figure 5.17), one finds an asymptotic value ~ 1.06. Moreover, between iterations 1 and 25 the χ^2 parameter has already covered the 75% of its total variation, thus, if the algorithm is stopped before the 25th iteration, the bulk of the restoration is preserved (and the artifacts regime avoided).

The main effect of the restoration process is to compact the CMD features along the deconvolution axis (absolute magnitude axis):

1. the red clump region is compressed and new features appear

2. the giant and sub-giant regions are more definite

3. the main sequence blue border is sharper

These new features in the CMD could appear small, but the restored image is the most detailed data we could obtain.

In the next chapters, I will apply theoretical models to this restored (cleaned) data. Before closing this chapter, even if the “empirical” stopping criterion I adopted before is perfectly afficient, I will try to search for a possible parameter to indicate the beginning of noise amplification (in a way to we can stop the R-L algorithm before).

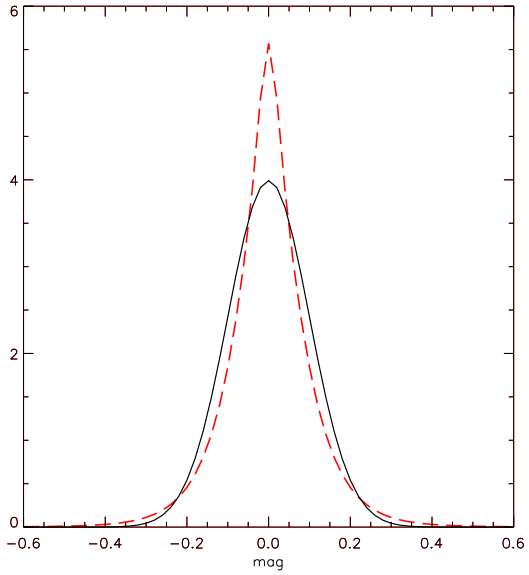

Figure 5.16: The black line is a Gaussian function with $\sigma = 2$ pixels mag. The red line represents the function obtained from a linear combination of Gaussians with standard deviations and weights obtained by the analysis of observational data.

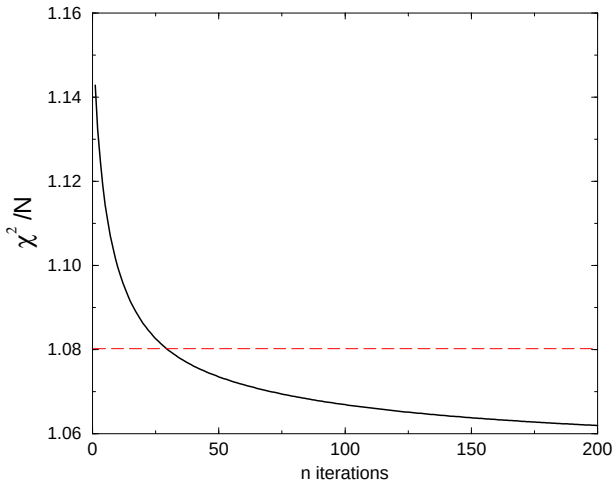

Figure 5.17: Reduced χ^2 against iteration number for the pseudo-gaussian PSF. The horizontal dashed line represents the value of χ^2 after 50 iterations.

5.6.1 Building an artifact sensitive parameter: some ideas

Noise amplification

Due to the global information brought by the χ^2, this parameter does not allow to identify the beginning of artifacts. A Kolmogorov Smirnov test, which is sensitive to local differences, cannot be the solution in this case because the restored image is binned.

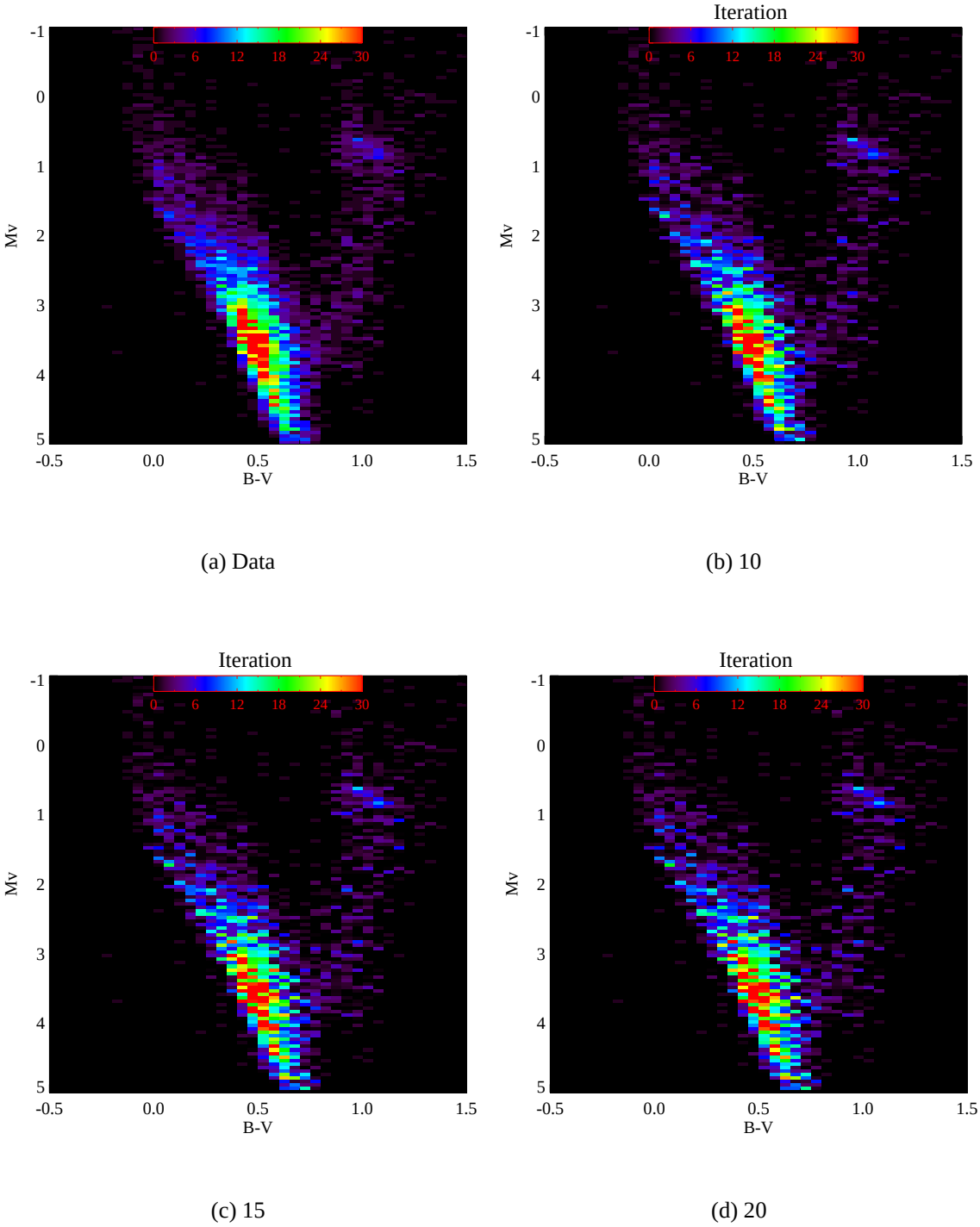

(a) Data (b) 10

(c) 15 (d) 20

Figure 5.18: (a) The original data. (b),(c),(d) show the restored data (adopting the pseudo-gaussian *psf*) after 10, 15, 20 iterations.

Another solution could come from a so called "dithering" technique. The same data should be binned several times in grids slightly displaced among each others, producing a set of pseudo-data (images). Each pseudo data could be restored separately, obtaining a set of restored images (representing the same solution, but with slightly different local information). These images could be combined to obtain a cumulative distribution (for absolute magnitude and for color) with much more information than a single restored image could bring. This cumulative distribution could be compared with the data cumulative distribution using a KS test. Changing the data sampling is equivalent to reconstruct a deconvolved image on a smaller grid (enhancing the resolution). In fact, the artifacts are the result of the Nyquist theorem violations: the initial binning cut the high frequencies of the data, producing a Nyquist frequency. Too many restoration increases the resolution (amplifying high frequencies), until the recovered frequencies overcome the Nyquist value and the artifacts appear. Combining different sampling (that is data binned with displaced grids) allow to identify the Nyquist frequency and, with this, also the point to stop the iterations.

Another possibility involves a weighted χ^2. In fact, most of the problem with noise amplification comes from the CMD regions with low signal to noise. From stellar evolution we know that low density regions (clump and giant zones, for example) are a consequence of the faster evolutionary times: in other words, from stellar evolution we know the ratio among star counts in different parts of the CMD. Thus, the idea is to weight the χ^2 with a factor inverse proportional to the life time of the stars involved. The result is a parameter that does not follow the χ^2 statistic, but it weights, without preferences, all the CMD regions. If the restoration generates artifacts in low signal to noise regions, this parameter should realize.

Wrong PSF

A wrong choice of the PSF leads to a limited restoration (after few iterations, the image is corrupted by artifacts; see discussion in section 5.5.2). In this section, I will attempt to find a parameter sensitive to artifacts (and in a position to judge if the chosen PSF is right). The starting point is to generate a copy of the artificial data, by means of the bootstrap technique (the data of the new artificial sample are selected random, with replacement,

from the original data). The two sets of simulated data will be binned and blurred with the same *psf* ($\sigma = 2$ pixels, for example). After that, the R-L algorithm is applied, adopting several point spread functions, characterized by different widths ($\sigma = 2, 5, 10$ pixels). The result is this: if we apply the R-L algorithm using the right σ (2 pixels), I recover the same solution (within the statistical differences) for both the samples. If we apply the R-L with a larger *psf*, after a given number of iterations, we find *two different restored images*, because the statistical noise is amplified (the statistical differences introduced by the bootstrap method will be magnified). A way to show this is using the distribution of the residuals calculated at each iteration step between the two solutions; the problem of the χ^2 was the global nature (sum of squared residuals), so a solution could be to analyze only specific regions of the residual distribution. After many trials, I found that a good parameter is this:

$$R = \frac{\Sigma_i(Res_i > 1)}{\Sigma_i(Res_i < -1)} \tag{5.3}$$

where $\Sigma_i(Res_i > 1)$ and $\Sigma_i(Res_i < -1)$ are respectively the sum on residuals greater than 1 and lower than -1.

The figure 5.19 shows the parameter R against iteration number, for different assumptions of the *psf* width adopted for the R-L algorithm (the data are blurred by a Gaussian *psf* with $\sigma = 2$ pixels). The dashed horizontal line is the R value for the two original images (before blurring). It is evident that the restoration made with the correct *psf* reach a R-value very close to the true one (about 1.16). The restoration made with σ equals to 5 and 10 pixels reaches a maximum (after 15-25 iterations) and after that it falls down (reaching a stable value very far from the true value).

This divergence is a manifestation that the noise amplification is begun. The parameter R is sensitive to artifacts generation because it does not use the total residual distribution but only the wings, checking the symmetry. In conclusion, the natural choice to avoid noise amplification will be to stop the restoration when the maximum for the parameter R is reached.

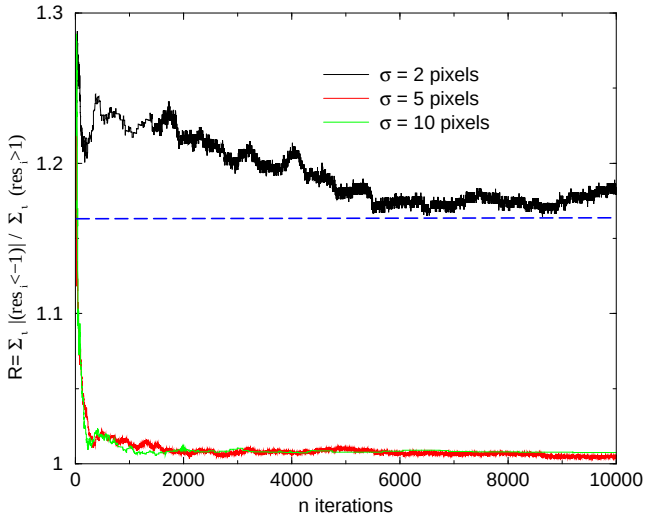

(a)

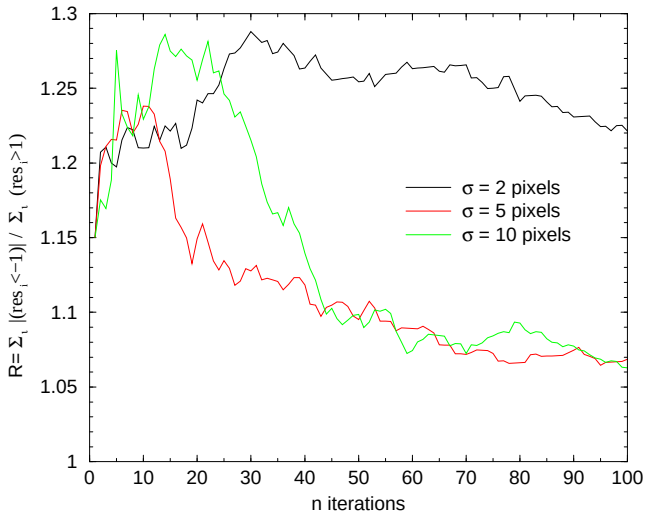

(b)

Figure 5.19: (a) R parameter against iteration number for the indicated σ values. The original and the bootstrapped images are blurred with a $\sigma = 2$ pixels. (b) As picture (a), but only the first 100 iterations are shown.

6

Recovering the SFR

In the previous chapter I described how a CMD for the typical mass range covered by the Hipparcos sample can be interpreted on the basis of stellar evolution theory. To demonstrate the relative influence on the CMD of different IMFs, chemical compositions and presence of binaries all simulations used a fixed star formation rate. In this chapter I will discuss the method and the related problems to derive, from an observational sample such as the Hipparcos catalog, informations about the SFR.

First of all, I will abandon the idea of "a priori" constant star formation; this does not mean that a constant SFR is necessarily wrong, but that it is not the only possibility, and I will explore a wide range of star formation histories.

Our problem is: do the Hipparcos data (characterized by a limited number of stars, with a completeness limit and masses above $\sim 1\,M_{\odot}$) permit a recovery of the underling SFR? In particular, does our partial knowledge about the IMF, uncertainties on the age-metallicity relation, and the presence of an unknown percentage of binaries affect the results? In the next sections I will analyse these points by using synthetic "artificial observations" built with the same number of stars as the observed sample (at the same completeness limit). Each artificial observations are computed with a specific combination of SFR and secondary parameters (IMF, chemical composition and percentage of binaries). As first step, I will try to recover the input SFR when the "artificial observations" and the

"theoretical model" have been created with the same secondary parameters. In this case the only limit is the completeness limit. In fact, if the sample extends to a larger distance, the completeness limit in absolute magnitude is brighter and the possibility to recover information on the old star formation history decreases.

As a second step I will check how the result changes when wrong (that is different from the ones of artificial observations) secondary parameters are adopted in the model. In this way, one can identify which parameters are critical to recover the right SFR. Finally, the influence on the recovered SFR of a simple stellar population accidentally present in the sample will be explored.

The last section will be dedicated to the comparison with the real Hipparcos data sample.

6.1 Artificial color-magnitude diagrams

An usual procedure to understand which SFR could generate an observed color-magnitude diagram is to produce artificial CMDs to be compared with the observations. Both the data photometry and the artificial photometry are stored in a color magnitude grid and each bin of the color-magnitude grid will contain the number of stars observed or predicted to be in it. The SFR with the higher probability to generate the data is chosen by means of a suitable maximum likelihood test.

The first technical problem of a similar approach is the time spent for the Monte Carlo generation of a CMD for each SFR. So, to explore a sufficiently wide number of star formations, it is impossible to generate directly every single CMD. A necessary step is to build a set of partial CMD and to use them to produce whatever CMD. Each partial CMD will be generated with a step star formation, uniform in a given time interval and zero elsewhere. The step functions has to be exhaustive (the sum covering the whole Hubble time) and they cannot overlap.

Thus, for each combination of IMF, binary distribution and chemical composition the CMD corresponding to any SFR will be computed as a linear combination of the partial CMDs:

$$m_i = \sum_j r_j \, c_{ij} \tag{6.1}$$

where m_i is the number of star in the final CMD in bin i, r_j is the star formation rate for partial CMD j (see figure 6.1), and c_{ij} is the number of stars in the bin i owning to the partial CMD j.

The main advantage of this procedure is the possibility to explore a large parameter space: instead of building a time-consuming Monte Carlo for each star formation history, the partial CMDs can be linearly combined to build a CMD for any star formation history. In other words, the number of Monte Carlo simulations is reduced to the number of partial CMDs. This method has been already applied by several authors (see e.g. Aparicio, Gallart & Bertelli 1997a-b, Gallart et al. 1999, Bertelli & Nasi 2001). The duration of each star formation step should depend on the timescale of the typical stellar population involved, in order to enhance the time resolution of fast evolutionary phases. Thus, for the Hipparcos sample, I chose star formation steps of half Gyr for stars younger than 2 Gyr, increasing the duration for the older star formation steps (see figure 6.1 for details).

When the temporal step is chosen, the partial CMDs are generated following the prescriptions of the chapter 4 (section 4.1). In order to minimize the Poisson fluctuations, the partial CMDs are populated with the same large number of stars (40000).

6.2 Statistical approach

After the calculation of an artificial CMD with a specific SFR, the main problem is to compare it with an observational CMD, in order to accept or refuse the adopted SFR. The first step is to transform the CMDs in two dimensional histograms, choosing bin sizes in color and in absolute magnitude. Once the number of theoretical and observational objects is known in each bin, the artificial histogram is normalized to the number of objects populating the whole observed histogram. The second step is to use a norma (a function of the residuals) to define the distance between the two histograms. The third step is to move in the parameter space (through a minimization algorithm) searching for the best set of parameters and evaluating the confidence limit of the results.

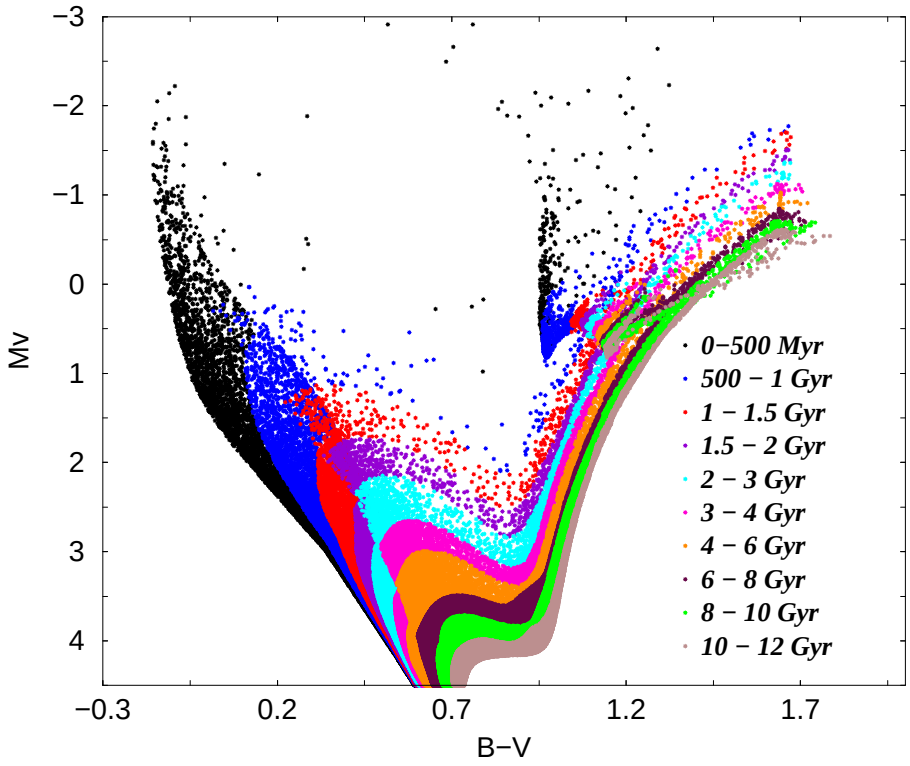

Figure 6.1: The figure shows in different colors the partial theoretical CMDs. Each one is generated with a flat star formation rate, for the labeled age intervals. The metallicity is solar. The bright part of the main sequence is dominated by high mass stars so that finer time steps for the corresponding SFRs are chosen.

6.2.1 Grid choice

An important choice is the histogram bin size, or equivalently, the number of bins. If the bin width is too small, the histogram greatly fluctuates, and it is more difficult to recover the underlying SFR, on the contrary, if the bin size is too large one could loose informations.

A first rule to choose the grid, arises from the population of the sample; in fact the final result of my simulation is a CMD with the same stars number of the observed sample, so the suitable bin size is heavily dependent on the *total observed number of stars*. Another problem comes from the *mass range* of the sample: for example, massive stars have short life time (that is they move fast in the CMD) and they make straightforward to increase the bin size in order to map their history. Another limit is the *evolutionary phase* of the star mapping the CMD: after the main sequence, the partial CMDs become nearly degenerate

and consequently the grid needs to be finer. The right choice must thus come from a numerical check on the specific problem.

6.2.2 Estimator choice

In the following analysis I will assume that the observational CMD has already been "cleaned" by a R-L algorithm (see chapter 5) thus I will not take into account the observational errors. In other words, the possibility to retrieve information on the star formation history is checked under the hypothesis of pure statistical error (no correlation among bins), thus the choice of the likelihood estimator is between a chi-square or a Poisson based statistic. In order to prevent from low number statistical effects, I'll implement the Poisson estimator as seen in equation (2.38).

6.2.3 Confidence limit

The bootstrap is a resampling method for statistical inference, and it is commonly used to estimate confidence intervals. In empirical bootstrap simulations we process N time the original sample of data in a way that each of the original n data points is sampled with replacement * and with equal probability of being sampled. One finally obtains N synthetic data sets $D_1, D_2, ..., D_N$, everyone with n data points. Because of the replacements, some observations in each synthetic data set are repeated, while others are lacking. This feature mimics the observational process: if the observational data is representative of the underlying distribution, the synthetic data produced with replacements are copies of the original one with local crowding or rarefaction. This type of approach is particularly useful when one does not know the underlying distribution.

Imagine to have a model dependent by a parameter a and call a_0 the value giving the minimum distance (according to the selected estimator) between model and data. In practice, the method consist to impose to the bootstrapped copies the same minimization procedure as it would be performed to the real data set. The result will be a set of best parameters $a_1, a_2, ..., a_N$. The hypothesis is that this set of parameters will be distributed

*In a random sample with replacement, each observation in the data set has an equal chance to be selected and can be selected over and over again.

around a_0 close to the same way that a_0 is distributed around a_{true}. The confidence interval is just the interval that contain a certain percentage of this parameter distribution.

6.2.4 Searching for the "best model"

As already discussed, the model depends on several parameters (10 coefficients of the star formation rate), while the *distance* between theoretical models and data is measured through the function χ_P to be minimized to find the "best values" of the model parameters. The problem is to move within this multi-dimensional parameter space and to search the combination of parameters giving the minimum for χ_p [†]. The Nelder Mead simplex method (Nelder & Mead, 1965) has been extensively used for this purpose (see appendix 1 for details). An interesting feature of this technique is that it is only needed to know the values in N+1 points (in a space of N dimensions) of the function to be minimized, while no knowledge of the gradients is required. The core of the method is an evolving pattern of $N+1$ points (the vertices of a simplex) that span the N-dimensional space. The simplex explores the space by reflecting, contracting or expanding away from the actually worst vertex, or by shrinking toward the best vertex. An appropriate sequence of such mouvements converges to the nearest local minimum.

The main problem of the simplex method is the efficency: the presence of many local minima can prevent from reaching a real global minimum for χ_P. There is a solution to improve the simplex method efficency: for each new simplex we add a logarithmically distributed random variable to each vertex. Calling V the value of χ_P in a generic point of the simplex, this procedure leads to obtain a new value V':

$$V' = V - T \ln ran \tag{6.2}$$

where T is a parameter ("temperature") and ran is a random number between 0 and 1. The choice for the size of the parameter T depends on the depth of local minima from which we want to jump out. Large T values allow to explore randomly the whole space and to make experience of many local minima (avoiding to be trapped in one), small T values allow to explore the fine structures around the nearest local minimum.

[†]Poisson equation (2.38) is defi ned with the negative sign, so the maximum search become a minimum search

There is not unique formula for determining the best temperature. In practice, I tested the algorithm on artificial color-magnitude diagrams (in a way that I already knew the value of the parameters to be recovered).

The minimization algorithm was re-started (from an initial guess for model parameters) each time a “global minimum” was found. The new departure was randomly chosen (in order to avoid the dependence by the initial guess) in the parameter space, obtaining a class of best values. The final best parameter is the smallest among the best values. The restart process is stopped when this “minimum value” does not change anymore. Finally, the temperature is adjusted in a way that this “inf” is close as possible to the “right” combination of parameters (the coefficents of the star formation rate used to build the artificial data).

6.3 Sensitivity tests

We can thus study the application of the quoted method to the data sets, both simulated and real. The second implementation must follow the first, which represents the best possible situation and thus shows the theoretical limits of this type of analysis.

With this aim, there are different types of tests given in this work:

1. The selection of bin size for the CMD gridding. As already discussed, different choices affect the recovered star formation; it is necessary to try many values with the artificial data to be sure to have properly sampled all the mass ranges and the evolutionary phases.

2. The analysis of the influence of the completeness limit: it fixes the boundaries of the CMD that can be used. Due to the fact that different zones of the CMD give us informations about different epoques of star formation, the completeness limit determines our “zone of ignorance” of the SFR.

3. The uncertainties in the model parameters: it is important to investigate how the recovered SFR is sensitive to the model parameters (IMF, ingredients for the binary population, AMR, helium content, overshooting). This procedure may highlight

parameters whose values need to be known very accurately because they have a significant impact on the recovered SFR;

4. the contamination of stellar clusters in the sample. Their stars, if accidentally present in our sample, could lead to a biased SFR. The possible effects of an unidentified cluster within our sample must be explored.

Hereinafter I will call simply "Hipparcos sample" the selection of Hipparcos stars with visual apparent magnitude less than 8 and a maximum distance of 80 pc (corresponding to an absolute visual magnitude less than 3.5).

6.4 Choosing the bin size

Since now, I will call "artificial data" each synthetic CMD mimicing the Hipparcos data while the theoretical CMD will be simply indicated as "model". In order to understand how the choice of the grid can influence the results, I built an artificial CMD with a number of stars, brighter than $M_V = 4.5$, as in the selected Hipparcos sample and I tried to recover the SFR by adopting different bin sizes (artificial CMDs are compared with model CMDs for stars brighter than $M_V = 4.5$). First of all I fixed in the artificial data and in the model the same chemical composition and IMF and I assumed no presence of binary stars. The SFR used to create the artificial data (input SFR) is shown in figure 6.2 (black line).

The same figure shows how the recovered SFR changes when the bin size is increased. It is interesting to recognize two different effects. The first one regards the error bars (defined at 1σ level) of the recovered SFR: they increase slightly until the size of the bins reaches 0.2 mag, after that they increase faster, probably because overcoming 0.2 mag means to loose many typical CMD features.

The other point is the different informations brought by different CMD zones. For stars younger than 5 Gyr, increasing the bin size improves the match between recovered and input SFR. The situation is opposite for the old SFR: when a coarse binning is adopted ($\Delta M_V \gtrsim 0.2$), the information on the SFR older than 5 Gyr is progressively lost. This is easily understood by looking at figure 6.1. Young partial CMDs comprise massive stars so the covered CMD region is wide (more massive is a star, longer is the excursion in

color to reach the red giant branch) and poorly populated: small bins pick few stars and the recovered SFR suffers of low number statistic. On the other side, old partial CMDs are composed by less massive stars so a narrower bin size is required to distinguish different SFRs. A bin size between 0.05 and 0.1, both for the color and for the absolute magnitude, seems to be the best compromise.

6.5 Completeness limits

The presence of a completeness limit hinders the possibility to exploit all the informations contained in the CMD. Following our sample selection (see section 6.3), the completeness limit for Hipparcos stars is close to $M_V \sim 3.5$. In this section I will explore how different limits in absolute magnitude can modify the recovered SFR. For this analysis, I will focus the attemption on three limits in absolute magnitude: $M_V = 2.5 \div 3.5 \div 4.5$. During the test I will emphasize the separate contribution given by the main sequence and by late evolutionary phases (RGB and red clump), that I selected as stars with $B - V > 0.8$. The results are pictured in figure 6.3. It is evident that the main sequence brighter than 2.3 mag gives us informations only about the recent SFR. The entire information on stars older than 3 Gyr is lost. The result is improved very much including also late evolutionary phases. The recovered SFR is close to the original one, even if the error bars are large. Large error bars are due to the fact that one obtains informations only from fast evolutionary phases (clump and red giants for the past star formation and high main sequence for the recent one) and the probability to find stars in these zones is low. Obviously we are considering a perfect situation where both the chemical composition and the IMF of the stars are well known so the obtained uncertainty is the minimum possible. When we will analysis real data other sources of uncertainties will occur.

Including stars until $M_V = 3.5$ the precision of the recovered SFR increases and also from the main sequence alone one can recover the SFR up to ~ 6 Gyr. However, to recover older star formation histories it is necessary to include the late evolutionary phases. Also in this case the uncertainty in the recovered SFR, for stars older than 6 Gyr, is large. The reason is the same: for $M_V < 3.5$, the information on the ancient star formation comes only from late evolutionary phases, too fast to account a sufficient

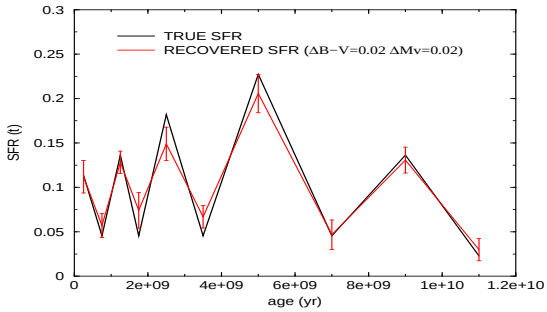

(a) $\Delta(B-V) = 0.02$, $\Delta M_V = 0.02$

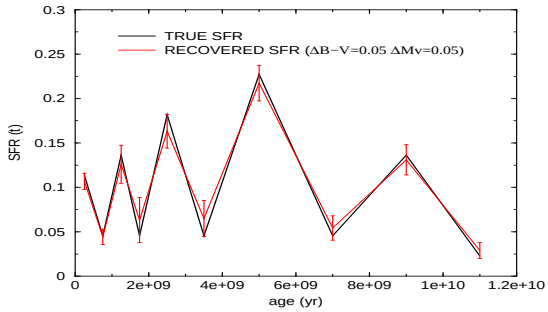

(b) $\Delta(B-V) = 0.05$, $\Delta M_V = 0.05$

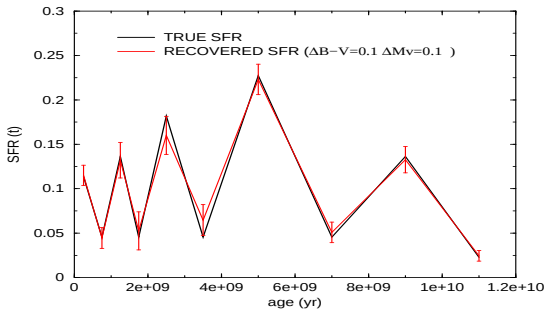

(c) $\Delta(B-V) = 0.1$, $\Delta M_V = 0.1$

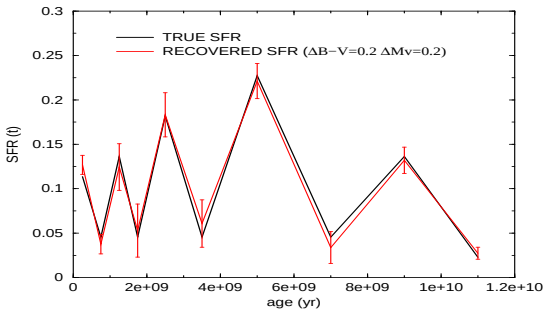

(d) $\Delta(B-V) = 0.2$, $\Delta M_V = 0.2$

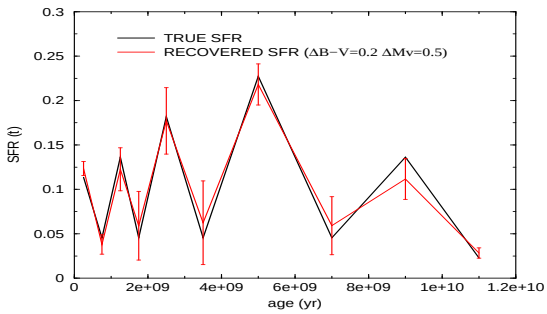

(e) $\Delta(B-V) = 0.2$, $\Delta M_V = 0.5$

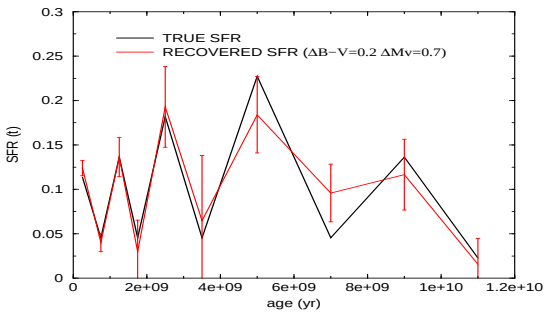

(f) $\Delta(B-V) = 0.2$, $\Delta M_V = 0.7$

Figure 6.2: "True" (black line) and recovered (red line) SFR for different binning choices, as indicated.

number of stars.

By increasing the magnitude limit at $M_V = 4.5$, the entire SFR is recovered with small uncertainties. Including only the main sequence gives some problems in the old SFR; in fact a systematic difference between recovered and input SFR is evident. The inclusion of late evolutionary phases leads to the right solution. The results are not linked to the chosen SFR. Figure 6.4 shows the results of the method for different input SFRs.

6.6 IMF - SFR degeneracy

Even if the IMF shape for masses above $1\,M_\odot$ is quite well known by observations and theoretical analysis (see Larson et al. 1992), the precise value of the exponent is still debated. Kroupa (2001) claims as the most probable value the Salpeter exponent 2.3, but the same author gives an uncertainty of about ± 0.7. Thus each investigation for the local SFR must take into account this still present uncertainty.

The possibility that the IMF mimics the SFR effects on CMD is related to the problem of the precise knowledge of the IMF shape, leading to a well known degeneracy of the effect of the two parameters.

Thus I will analyse the sensitivity of the recovered SFR to the chosen IMF. To this aim, artificial data were generated with different IMF exponents ($s = 1.3,\ 2.3,\ 3.3,\ 4.3$). The possibility to recover the underlying SFR was tested using in the model a *fixed IMF exponent equals to 2.3*. The results are shown in figure 6.5. It is important to notice that the input SFR is always recovered: even if one adopts a wrong IMF (that is different from the one used for the artificial data) it does not lead to a wrong solution (at least for "reasonable" exponents less than 4). The conclusion is that, for the mass range covered by Hipparcos sample, the IMF is not a crucial parameter and the explanation is simple. Recent steps of star formation are populated by the whole mass spectrum (only very high mass stars could be dead), so the IMF modifies the population of all the recent steps of star formation in the same way (the relative SFR is preserved). On the other side, the old steps of star formation (8-10, 10-12 Gyr) include only low mass objects (more massive stars are already dead), while the IMF variations mainly alterate the ratio between old (older than 8 Gyr) and recent star formation and thus do not sensitively influence the population

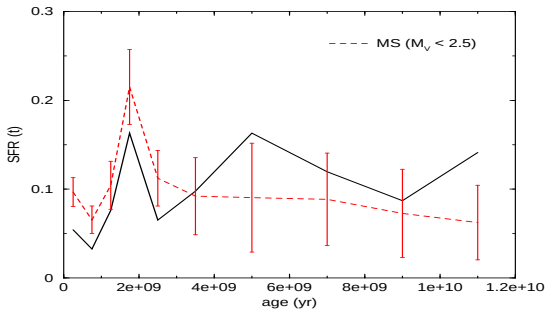

(a) Main sequence stars ($M_V < 2.5$)

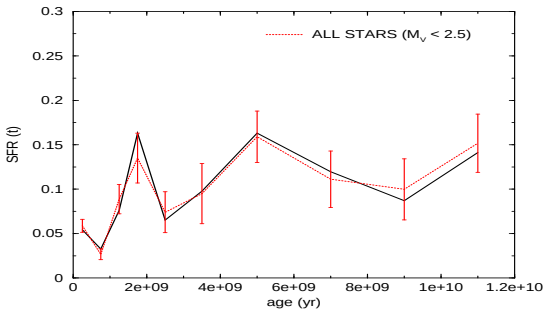

(b) From all stars ($M_V < 2.5$)

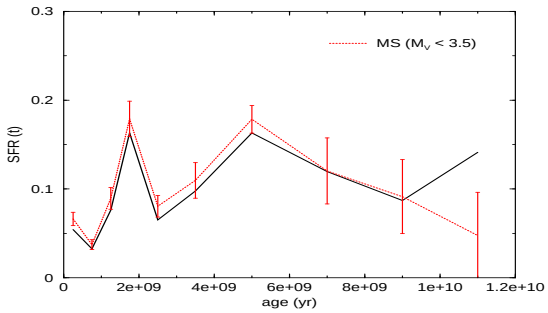

(c) Main sequence stars ($M_V < 3.5$)

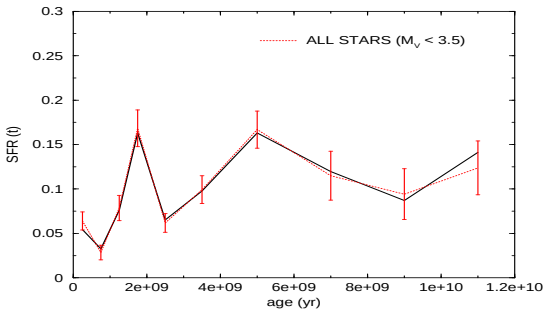

(d) From all stars ($M_V < 3.5$)

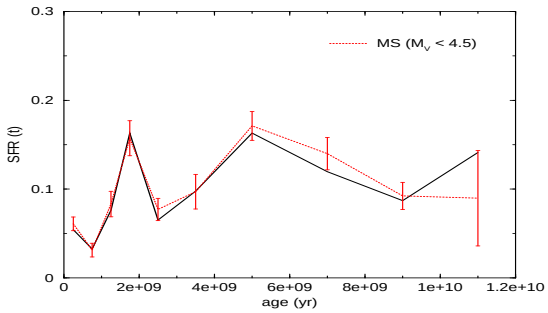

(e) Main sequence stars ($M_V < 4.5$)

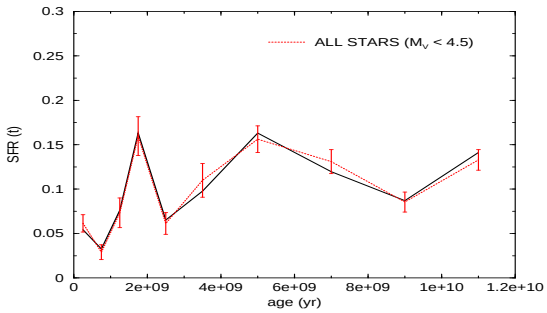

(f) All stars ($M_V < 4.5$)

Figure 6.3: "True" (black line) and recovered (red line) SFR from stars brighter than $M_V = 2.5 - 3.5 - 4.5$. On the left the figures show the results obtained using only main sequence stars. Figures on the right represent the recovered SFR by exploiting all the evolutionary phases.

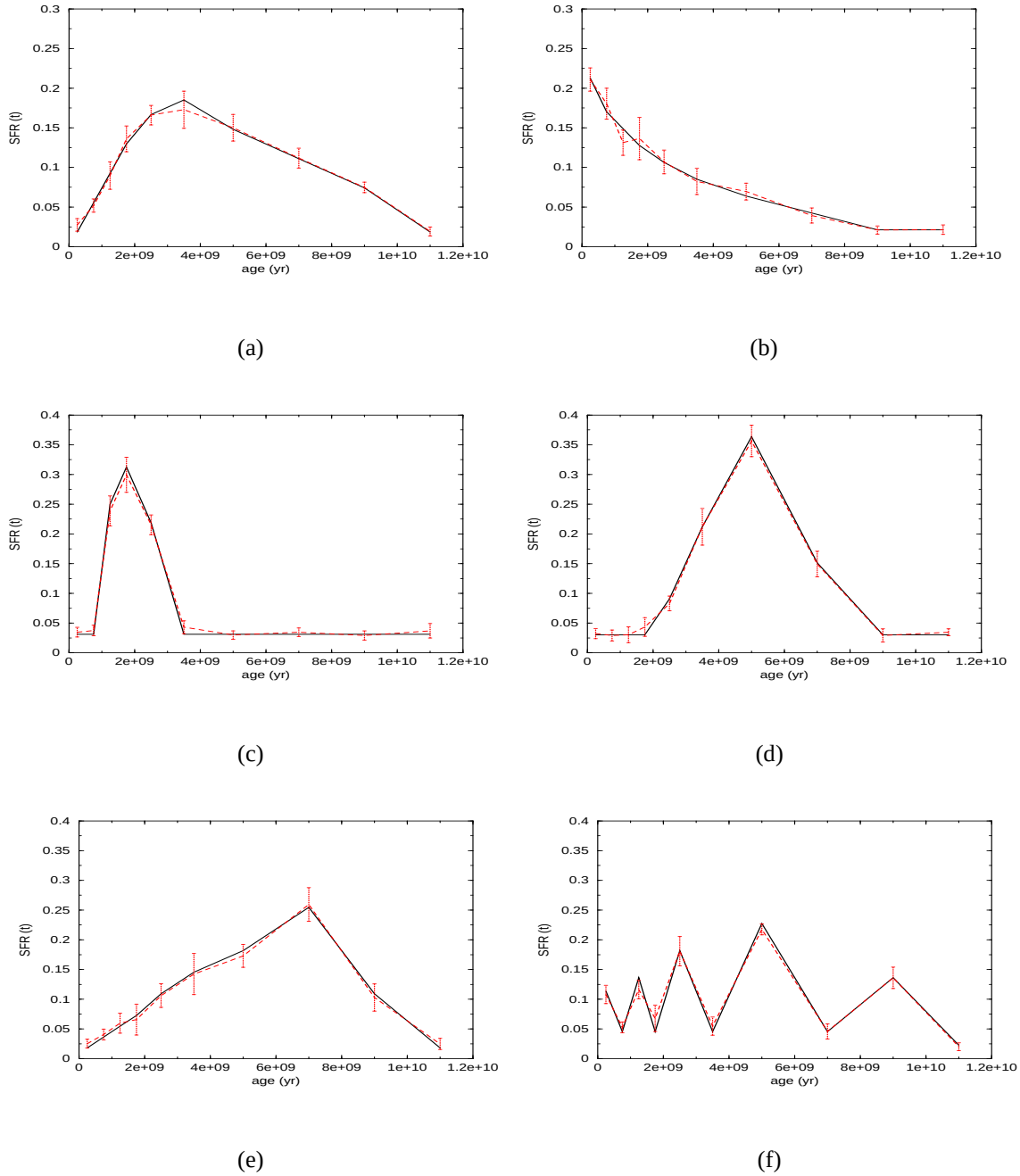

Figure 6.4: As in figure 6.3 for $M_V < 4.5$ and all evolutionary phases for different input SFR shapes.

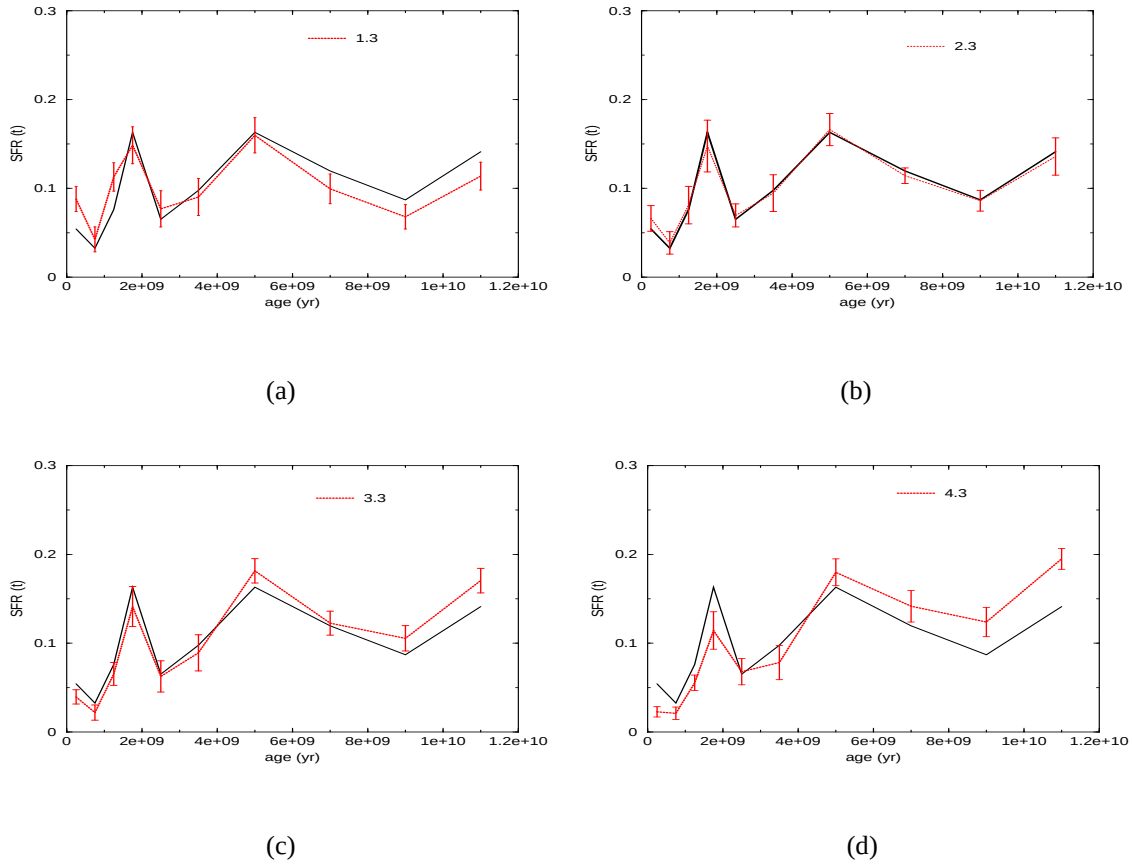

(a) (b)

(c) (d)

Figure 6.5: The "true" (black line) and the recovered (red line) SFR for different values (labeled) of the IMF exponent used in the artificial data. The IMF exponent used in the model is fixed to 2.3.

in the old SFR steps (see figures 6.5).

6.7 Binaries - SFR degeneracy

Another source of uncertainty, when one looks at the solar neighborhood, is the percentage of stars in binary systems and the relative mass ratio. My model does not account for binary evolution with mass exchange, thus I assume that each star in a double system evolves as a single star. On the other hand the state of the art of our knowledge for binary stars populations and evolution in the local disk is far from a perfect understanding, so the inclusion in the model of interactive binaries would involve many other unknown parameters as the mass exchange rate, separation, etc..). However, the simple presence

of a given percentage of not resolved binary systems affects the CMD morphology. The aim, here, is to establish if these effects can destroy or alterate the recovered information on the SFR. In order to perform this analysis, I built the usual artificial data (solar metallicity, Salpeter IMF) using different prescriptions on the binary population (10%, 20%, 30%, 50%, 70% of binaries with random or equal mass ratio). The equal mass ratio represents an extreme case which increases the effect of the presence of binaries. The partial CMDs used in the model were built with the same composition and IMF adopted for the artificial data, but without binaries. From figure 6.6 one clearly sees that, as found for the IMF, we can recover the right SFR independently on the presence of binaries in the artificial data. In particular, the presence of binaries does not affect the recent SFR, while the only modifications concern the old SFR. This is due to the presence of high mass stars in the recent steps of SFR: for these stars, the CMD displacement caused by the presence of binaries is of the same order of the displacement in color and luminosity that a mass cover in a time shorter than the duration of a recent star formation step. In contrast, the old steps of star formation include only low mass stars: here, a displacement in the CMD caused by binaries could mimic the effect of an age difference longer than 2 Gyr (that is the duration of the old steps of SFR), causing a "degeneracy effect" in recovering SFRs. This effect is evident in the simulations where the artificial data comprised at least about the 30% of stars in binary systems (see figure 6.6): beyond 6 Gyr the recovered SFR is slightly and systematically different by the input SFR (even if for all the cases but (d) the general trend is still recovered).

6.8 Metallicity - SFR degeneracy

6.8.1 Artificial data with single metallicity

In this paragraph I will analyse the effect of the assumed age-metallicity relation on the recovered SFR. Hereinafter, we will assume that IMF and binary population are the same both in the model and in the artificial data.

From the stellar evolution concepts introduced in the chapter 4, we understood how old, metal-poor stellar populations could mimic younger, metal-rich populations. Moreover, from the knowledge that the solar neighborhood is a blend of stars of different

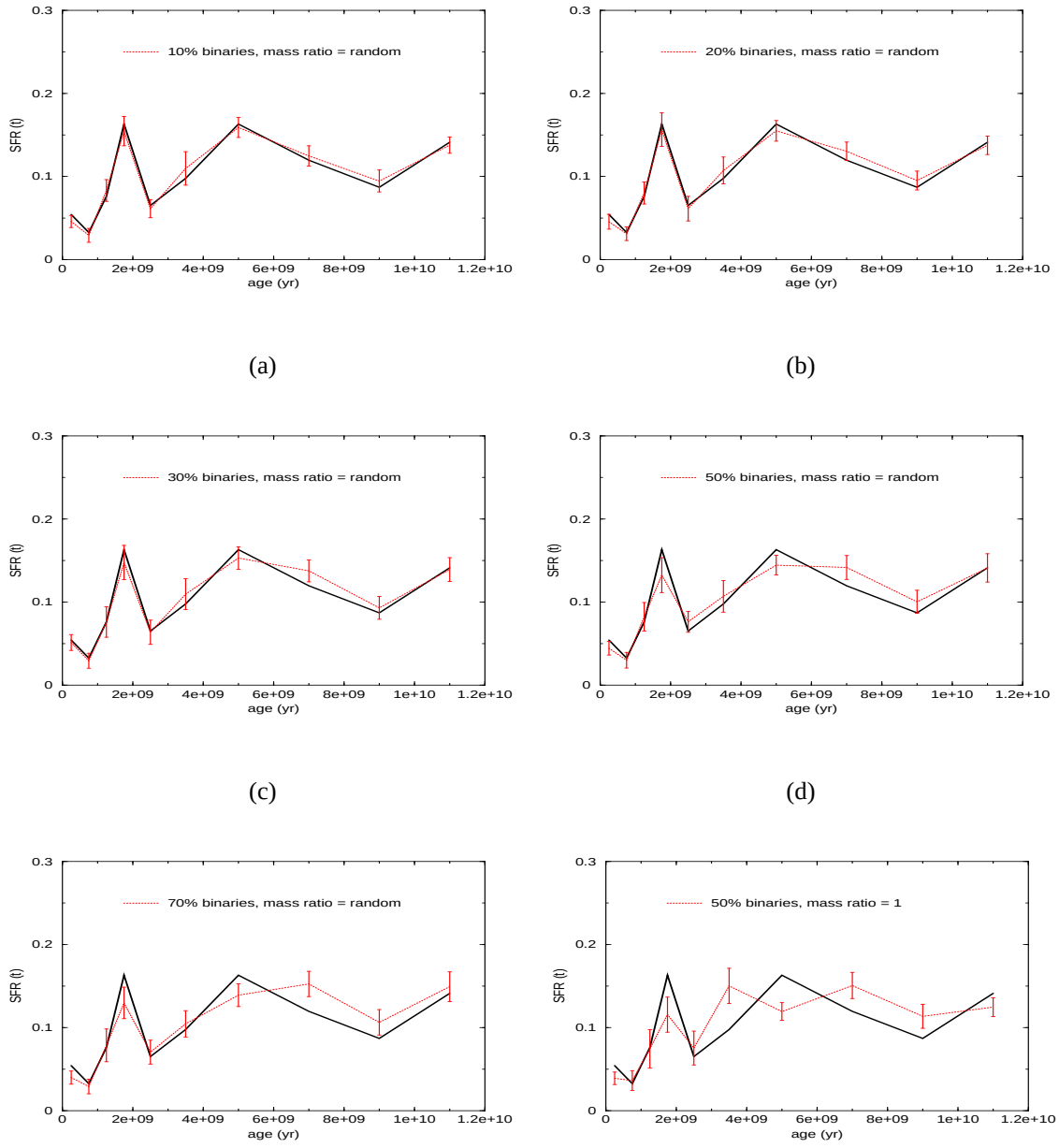

(a) (b)

(c) (d)

(e) (f)

Figure 6.6: "True" (black line) and recovered (red line) SFR. The artifi cial data is generated with the indicated percentage of binaries and mass ratio (random number or unity), while the model is without binaries.

chemical compositions (see scatter plot in figure 1.8), we expect a very complex influence of the composition on the CMD morphology. These simple considerations oblige us to check if it is still possible to recover the SFR when only a partial knowledge on the AMR is available.

As first step, I built a set of artificial data with different metallicities and I tried to recover the SFR by adopting a model with the solar metallicity.

The results are drawn in figure 6.7. Clearly, if we adopt the same metallicity in the artificial data and in the model, the SFR is recovered. However, if we slightly change the metallicity in the data ($\Delta Z = \pm 0.005$), without changing the solar composition of the model, systematic and relevant discrepancies appear in the recovered SFR.

If the artificial data are metal poor compared to the model, one obtain an underestimate of the ancient SFR (because less metallic artificial stars are bluer and to reproduce them the more metallic models must be younger); on the other side, metal richer artificial data lead to overestimate the ancient SFR.

This result is a strong warning about the widely used assumption of solar composition for nearby stars: small deviations from the solar value could bias the recovered SFR. Moreover, we know that similar deviations from solar values exist and are usually much larger than $\Delta Z = \pm 0.005$ (the metallicity distribution for the solar neighborhood in figure 1.8(b) shows stars with metallicity from $Z \sim 0.006$ to $Z \sim 0.03$).

6.8.2 Artificial data with an age-metallicity relation

In the previous section it has been pointed out the effects of a wrong assumption about the model chemical composition: if the metallicity chosen for the simulations does not match the data composition, the recovered SFR is definitely faked. If the metallicity is right, the SFR is recovered. Since the real data are far from being characterized by a single composition, it is necessary to explore a situation where both the model and the artificial data are generated with an age metallicity relation.

In other words, the new question is: if I know with a given uncertainty the composition of the stars in relation with their age (for example from external measurements or from the output of a chemical Galactic code), can I still recover the SFR? This point is important, if one considers that generally the AMR is assumed and one tries to recover

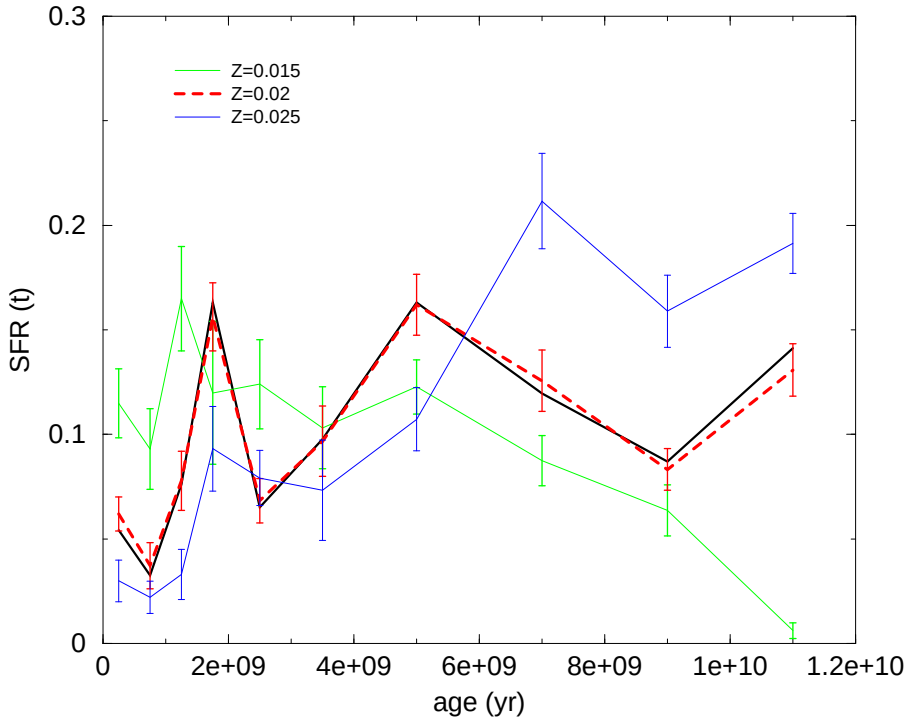

Figure 6.7: Sensitivity test to metallicity. The adopted composition for the model is solar. If the data have the same composition, the "true" SFR (black solid line) is close to the recovered one (red solid line). If the data metallicity is sligthly different from the solar value ($\Delta Z = \pm 0.005$), systematic relevant deviations appear in the solution (blue and green solid lines).

others parameters (IMF, SFR, binary fraction). The figure 6.8 shows the morphology of the model partial CMDs if an exponential age-metallicity relation $Z(t) \sim \exp(-t/\tau)$ is implemented.

Comparing figures 6.8-(b)-(e)-(h) to figure 6.1, a significant feature is appeared: as a consequence of the age-metallicity degeneracy, the partial CMDs obtained with different intervals of SFR overlap. The presence of a specific metallicity for each age allows young metal rich stars to overcome the CMD position of old metal poor stars. In this situation, when the SFR extraction method is applied, even if the artificial data and the partials CMDs have the same AMR, the input SFR is only partially recovered (see figures 6.8-(c)-(f)-(i)).

In order to exclude any influence by the explored AMR class (exponential), I tested another functional form. The figure 6.9 shows the result when a linear AMR is used.

Comparing figures 6.8 and 6.9 it seems evident that one of the factors determining the importance of the degeneracy is the AMR shape: where the AMR is steep, stars with

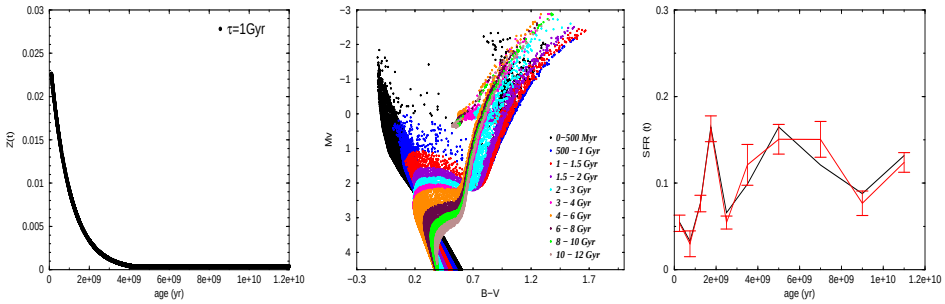

(a) $\tau = 1$ Gyr (b) Partial CMDs (c) SFR

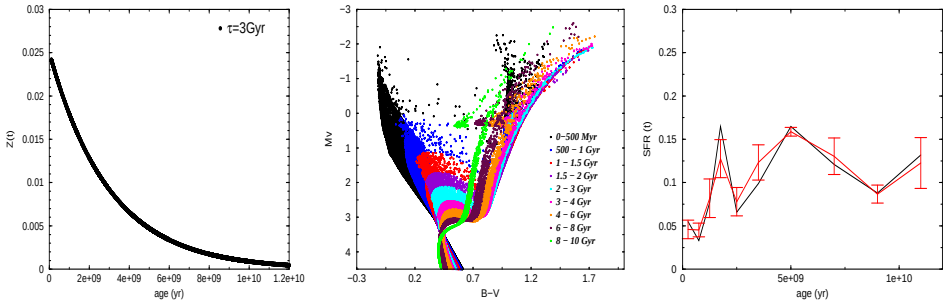

(d) $\tau = 3$ Gyr (e) Partial CMDs (f) SFR

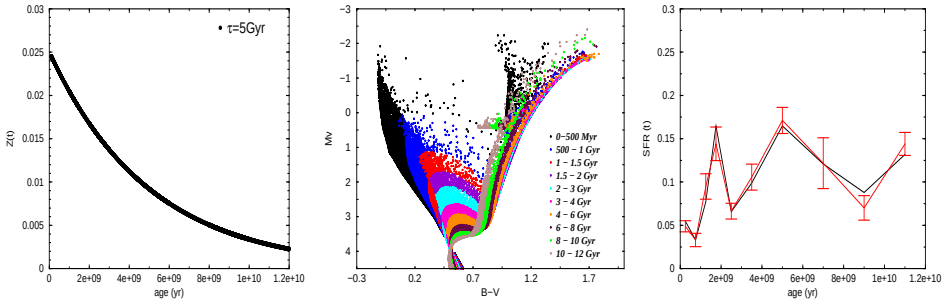

(g) $\tau = 5$ Gyr (h) Partial CMDs (i) SFR

Figure 6.8: Partial CMDs b,e,h computed with the exponential age-metallicity relations a,d,g which differ by the relative timescale (τ). The duration of the SFR steps is also indicated. The curves on the right are the input SFR (black line) and the recovered one (red line).

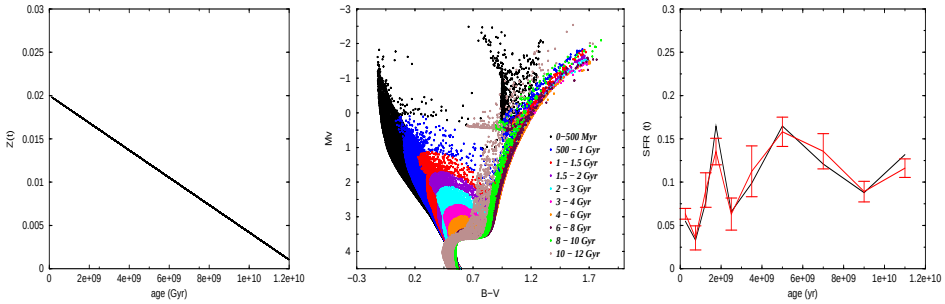

(a) (b) (c)

Figure 6.9: (c) Recovered SFR (red line) and input SFR (black line). The artificial data and the model adopt the linear AMR of panel a.

similar ages can assume very different metallicities and the degeneracy can develop. This effect is more important for the old SFR, where the partial CMDs are composed essentially by small masses (massive stars are evolved). The reason is simple: small stars evolve slowly and neighboring steps of star formation include very similar masses (see discussion in the chapter 4), so that a steep AMR can lead to a perfect overlap between contiguous partial CMDs. From the other side, recent steps of star formation include a *different* mass spectrum each one, making difficult for the AMR to produce a strong overlap on the CMD. As a result, recent SFR is, in general, better recovered, independently by the specific AMR, while the recovered old SFR has systematic differences from the input SFR, in a way dependent on the particular AMR.

In conclusion, the SFR extraction method is very successful when the data has only one metallicity, but it shows some limit when an age-metallicity relation is adopted. Moreover, the explored AMRs are monotonic, while a real AMR could change slope (infall could dilute the interstellar medium decreasing the metallicity). Thus, even if many features of the input SFR are not swept out (the overall structure is always recovered), the possibility to recover a detailed SFR only from the photometry and the knowledge of the chemical history is impossible. Probably, only the availability of additional information as the kinematic data (different velocities can identify different stars of different ages) or less metallicity dependent photometric indexes (as the Strömgren photometry) could help to break this degeneracy.

However, real data for nearby stars instead of showing a steep age-metallicity rela-

tion seems to show a large metallicity dispersion present at each time. The next section will be dedicated to test the possibility to recover the SFR when a metallicity dispersion characterizes the artificial data.

6.8.3 Artificial data with a metallicity dispersion

The age-metallicity relation by Nordström et al. (2004) (see figure 1.8), the most representative census for ages and metallicities in solar neighborhood, is characterized by a constant mean metallicity and a large scatter at all ages (about $\sigma \sim 0.2\,\mathrm{dex}$). In order to test the sensitivity to a metallicity dispersion, an artificial data was generated with the observed mean metallicity plus a Gaussian dispersion (the explored range is from $\sigma = 0.01$ dex to $\sigma = 0.2$ dex in $[Fe/H]$). The conversion between $[Fe/H]$ and Z appropriate for our models ($[Z/X]_{\odot} = 0.0245$, Grevesse & Noels 1993) is as follows:

$$Z = 0.73 \times 10^{([Fe/H]-1.61)} \tag{6.3}$$

where the enhancement of α elements is not taken into account because it is negligible for disk stars.

The SFR was searched, adopting in the model the same mean value of the artificial data, but *no spread*. The results are shown in figure 6.10, where the dashed line is the input SFR and the solid line the recovered one.

From the simulations it is evident that beyond $\sigma = 0.1$ dex, the most of the information contained in the SFR is wiped out: this numerical experiment has pointed out how the dispersion in metallicity can be a critical factor. Underestimating this dispersion can lead to a wrong solution.

It is interesting to see what happens when the right dispersion in metallicity is adopted both in the artificial data as in the model. In order to be close as soon as possible to the real data, I will adopt for our tests, the metallicity distribution as found by Nordström et al. 2004 (figure 1.8). This distribution is close to a Gaussian with a mean -0.14 dex and a dispersion of 0.19 dex.

Using this relation, the partial CMDs (see figure 6.1) assume a new morphology, drawn in figure 6.11.

Under these conditions, how just seen for the exponential age-metallicity relation, the partial CMDs overlap. However, the morphology is different from the figures 6.8

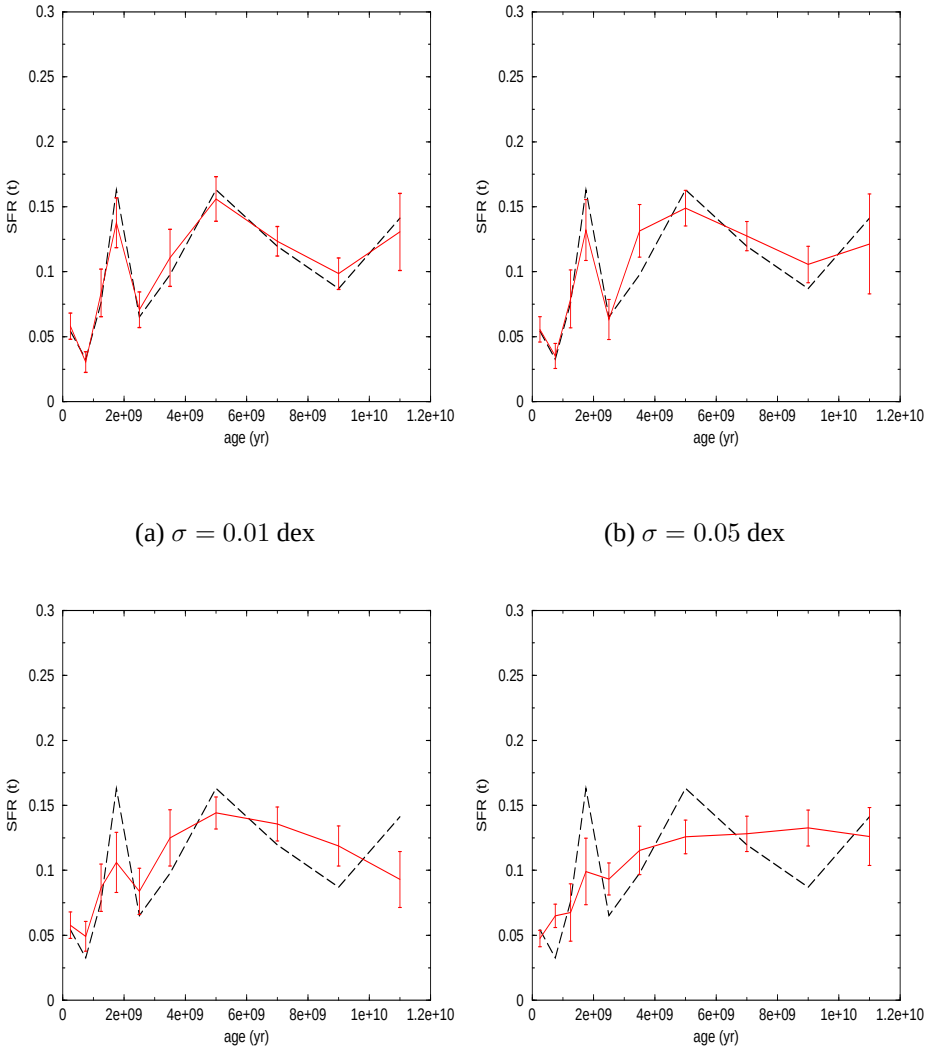

(a) $\sigma = 0.01$ dex

(b) $\sigma = 0.05$ dex

(c) $\sigma = 0.1$ dex

(d) $\sigma = 0.2$ dex

Figure 6.10: Dashed line: input SFR. Solid line: recovered SFR. The σ value indicates the dispersion in $[Fe/H]$, used for the artificial data. The model has the same mean metallicity, but no dispersion.

and 6.9 (obtained using AMRs without dispersion): now the old CMDs do not overcome the younger ones and the overall effect is only a broadening of the partials CMDs. The explanation for these features is all in the observational AMR used for the simulations. This relation shows a large spread and no significant trend, so that each partial CMD covers the *same metallicity range*.

Generating an artificial population with this AMR (the input SFR is the black dashed line in figure 6.12), the result of the SFR extraction (the partial CMDs are computed

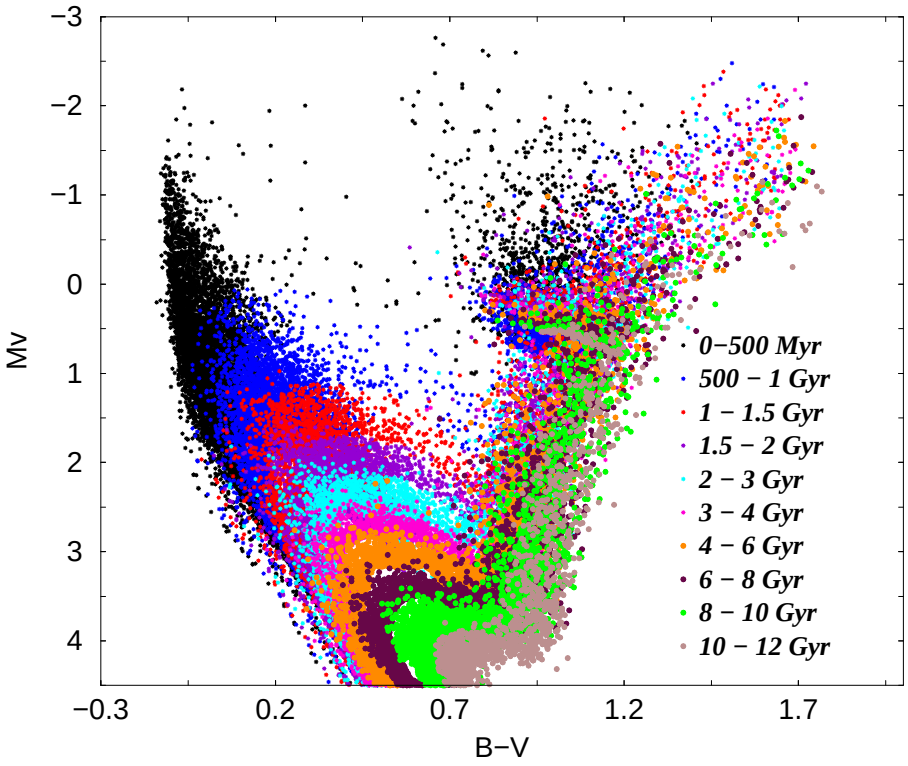

Figure 6.11: Partial theoretical CMDs. Each one is generated with a constant star formation rate with the labeled duration and the age-metallicity relation by Nordström et al. (2004).

with the same AMR) is presented in figure 6.12. There are systematic shifts between the recovered and the input SFRs (in particular the old SFR), indicating an uncertainty in our ability to distinguish different neighboring steps of star formation (for a comparison with the single metallicity tests, see section 6.8.1), but the trend is preserved. The implication for real data is appealing: if the nearby stars show an age-metallicity relation with a behavior similar to the one by Nordström et al., the application of the model to Hipparcos stars could give many information on the true SFR. Obviously in the real situation there are further complications, first of all the uncertainty on the IMF and the binary population: even if these parameters are not critical when one recover the SFR from the bright ($M_V < 4.5$) stars in the solar neighborhood (see sections 6.6, 6.7), a weak influence on the result is always possible. These effects, joined with the age-metallicity dispersion, could, in an unluckily situation as the one shown in figure 6.13, lead to a wrong solution. However, the aim of this work is not to recover the SFR, but to test the sensitivity of the recovered SFR to different choices of the Galactic parameters.

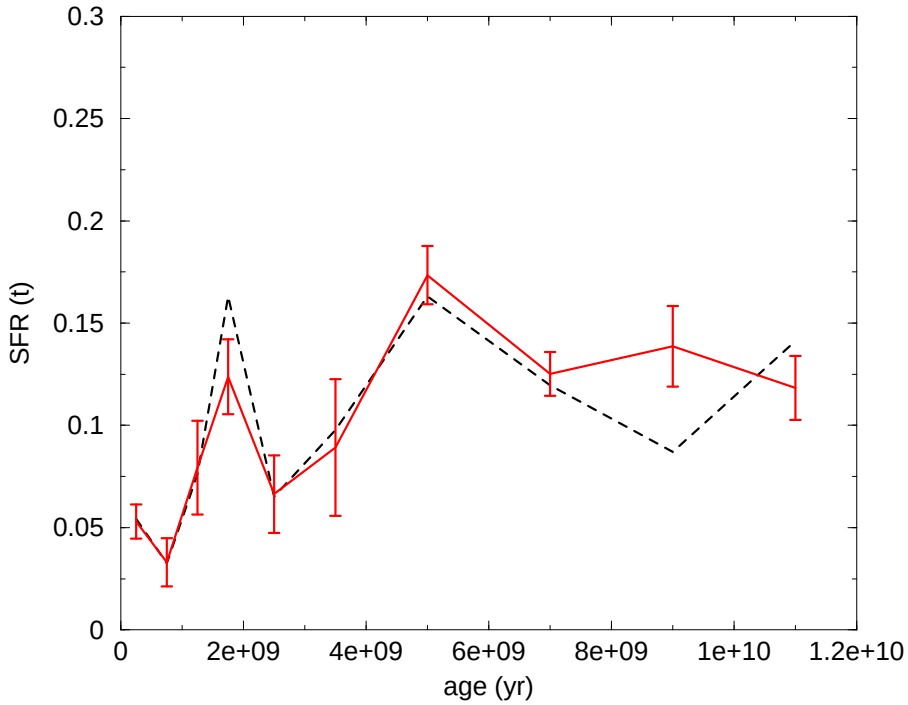

Figure 6.12: Input SFR (black dashed line) compared with the recovered SFR (red solid line). Model and artificial data have the same metallicity dispersion.

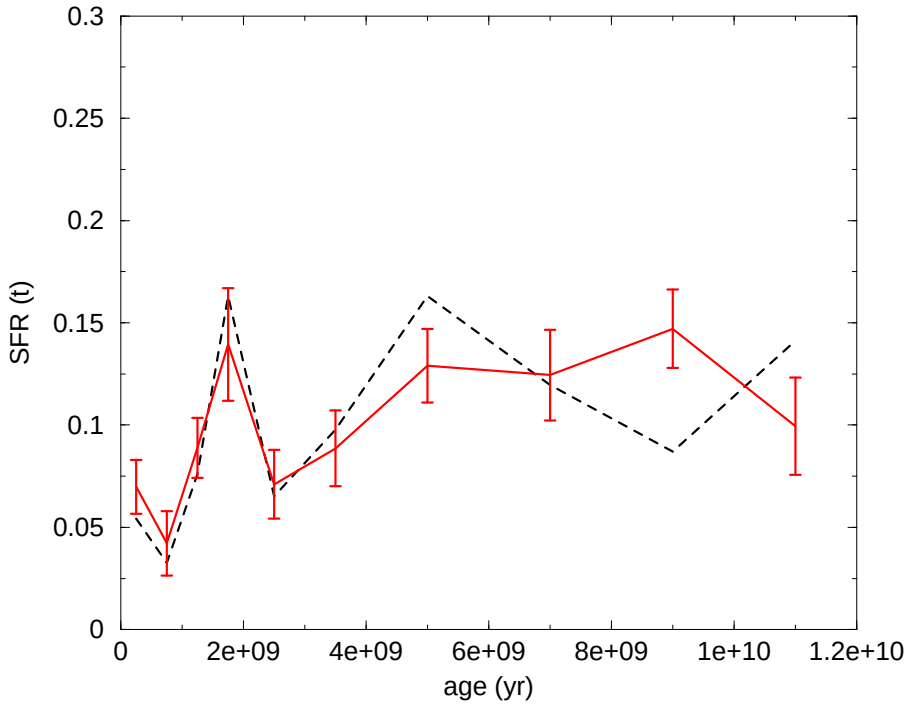

Figure 6.13: Artificial data and model have the same metallicity dispersion, but different IMF (s=2.3 for the model and s=1.6 for the data) and binary percentage (10% the model, 30% the data). The black dashed line is the input SFR. The red solid line is the recovered SFR.

6.9 Uncertainty on the helium content

Beyond the metallicity effect, the possibility to recover the SFR must be tested against the problem of the helium abundance for a given metallicity.

In fact, a direct measurement of the helium abundance in the photosphere of stars with effective temperature less than 20000 K is not possible because there are not helium lines in their spectra.

The traditional procedure to infer the helium abundance is to make use of a correlation (which is assumed linear) between the helium mass fraction Y and the metal abundance Z: the first step is to measure the primordial helium abundance Y_P; then, this value is compared to the Sun helium value (obtained fitting solar models).

In this process, the measure of Y_P is the most difficult because it is limited by systematic errors. In particular, from the observed metal-poor HII region spectra, the results indicates a value $Y_P = 0.249 \pm 0.009$ (Olive & Skillman 2004). On the other hand, recent determinations of the cosmological baryonic matter density from the cosmic microwave background provide a value $Y_P = 0.2484 \pm 0.0004$ (Cyburt et al. 2003).

The resulting $\Delta Y/\Delta Z$ is consistent with the color magnitude diagram for the solar neighborhood stars (Pagel & Portinari (1998) determines a ratio $\Delta Y/\Delta Z = 3 \pm 2$), for which we have accurate Hipparcos parallaxes and accurate spectroscopically determined metallicities.

In order to explore the effects of a wrong choice of the helium content I built an artificial CMD with $Z = 0.004$ and $Y = 0.27$ and I tried to recover the SFR using a $Z = 0.004$ model coupled with a canonical $Y = 0.23$ (the helium discrepancy is accentuated, so we are looking at a maximum effect). The result is shown in figure 6.14.

The small features of the recovered SFR are blended (the peaks are attenuated) but the overall trend is still recovered. The precise helium value seems not to be a critical parameter.

6.10 Uncertainty on the overshooting process

As already discussed in chapter 4, another important input (even if its efficency is still debated) of the stellar models is the overshooting in the convective regions (see e.g.

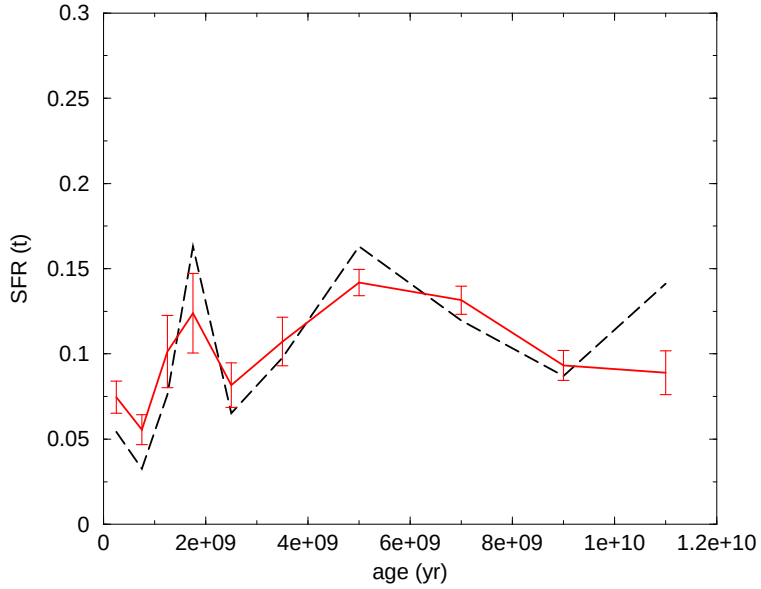

Figure 6.14: Artifi cial data and model have the same metallicity $Z = 0.004$, but different helium content ($Y = 0.23$ for the model and $Y = 0.27$ for the artifi cial data). The black dashed line is the input SFR. The red solid line is the recovered SFR.

Bertelli et al. 2003 and references therein, Brocato et al. 2003).

In order to investigate the effect of a wrong choice of the overshooting extent on the recovered SFR, I built an artificial CMD using stellar tracks *with overshooting* ($l_{OV} = 0.25\, H_P$), $Z = 0.004$, $Y = 0.23$ and I tried to recover the SFR using the canonical stellar tracks (same metallicity) without overshooting (the stellar tracks used in this work).

Figure 6.15 shows the result. The recovered SFR suffers of systematic shifts from the right SFR, but the overall trend is preserved.

6.11 Solar neighborhood and clusters contamination

The possibility that the solar neighborhood can include simple stellar populations (clusters) or part of them is very likely. From the studies about cluster membership, I identified about 80 Hipparcos objects, mainly Hyades stars, within 80 pc and brighter than $M_V = 3.5$ (the part of Hipparcos sample we are interested in). This number could appear small ($\sim 2\%$ of the sample), but these object are concentrated in time so they can produce a peak in the recovered SFR (at 500 Myr, for the Hyades). Indeed, this peak does not represent a global property of the Galaxy but only a local event. Thus, it is important to

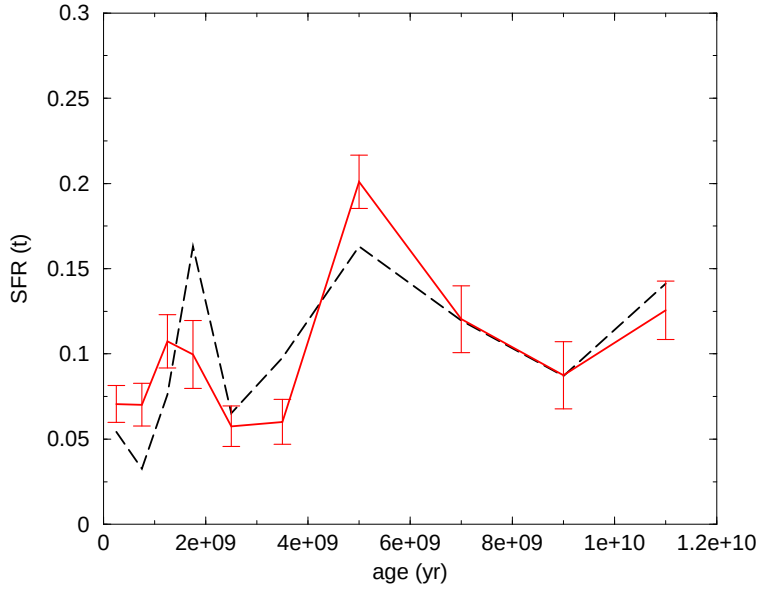

Figure 6.15: Dashed line: input SFR (the artifi cial CMD is built with overshooting stellar tracks). Red solid line: recovered SFR (the model is without overshooting).

eliminate each track of the known clusters and associations. Obviously, we cannot completely exclude that some cluster stars remain in the sample. Therefore, an interesting analysis could regard the cluster effect on the recovered SFR. To check this, the best way is to built the usual artificial data and add a cluster like Hyades or older. The comparison between the recovered SFR before and after the cluster contamination could inform about the possible effects of hidden populations in the real data.

In practice, I contaminated an artificial sample with a variable percentage of synthetic Hyades-like stars (500 Myr and solar metallicity) from 2% to 15%, trying to recover the SFR from the stars brighter than $M_V = 3.5$. The results are shown in figure 6.16. At 2% of contamination the SFR changes are within the error bars. Increasing the cluster stars percentage, the peak at 500 Myr becomes more and more evident. At 15%, the recovered SFR is perturbed on a scale of 5 Gyr.

The same test has been performed with a synthetic cluster of 2 Gyr. The figure 6.17 shows the recovered SFR when a 15% of synthetic cluster stars is added to the artificial data. It is evident that the changes in the recovered SFR are not localized at 2 Gyr, but it is the whole SFR shape between 2 Gyr and 7 Gyr to be altered. The reason is the chemical composition: we used a cluster with solar metallicity that is metal rich compared to the mean metallicity used in the model (synthetic data and model assume the observa-

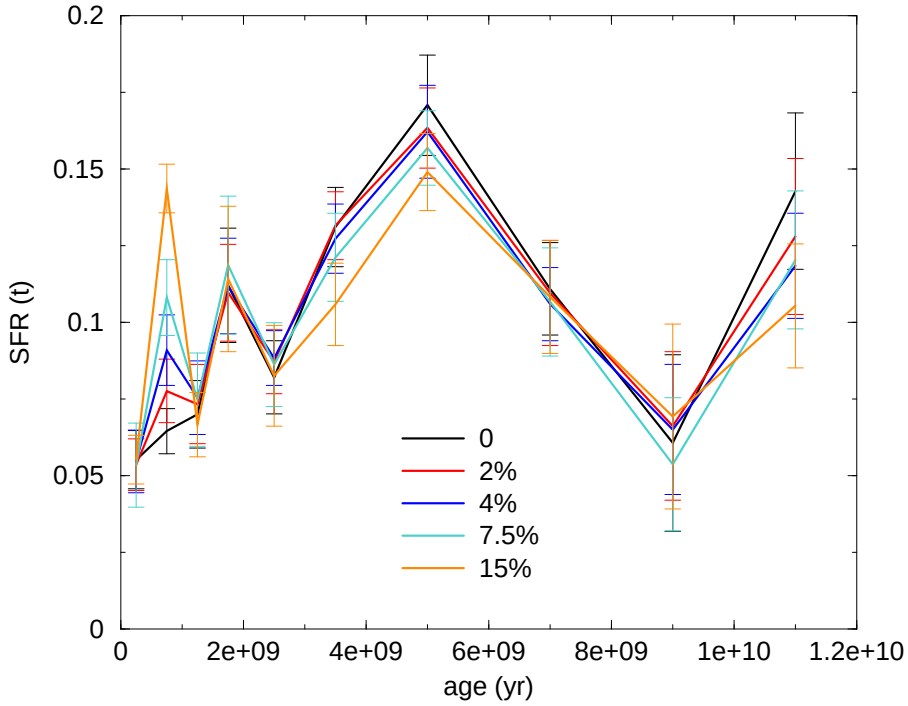

Figure 6.16: Recovered star formation rates for different contaminations (the percentage is labeled) of Hyades-like stars.

tional AMR by Nordström et al. 2004). Because of the age-metallicity degeneracy, this contamination of metal rich stars mimics a younger SFR.

Summarizing, these numerical experiments have shown how an accidental presence of stellar clusters blended with our sample could lead to a wrong SFR. For low concentrations (below 4 %) the right SFR is still recovered. On the contrary, when the contamination overcome the 15% the deviations in the recovered SFR are not localized to the cluster age, involving a wider time interval period.

These experiments did not consider the possibility that the contamination could take place by different types clusters at the same time. One can imagine that a similar situation could represent a strong limit to the recover of the Galactic SFR.

6.12 Comparison with real data

This last section is dedicated to the SFR extraction from the real Hipparcos data. Because both the IMF and the binary population do not represent critical factors (see sections 6.6 and 6.7), I will fix them: I adopted a power law IMF with a Salpeter exponent and no

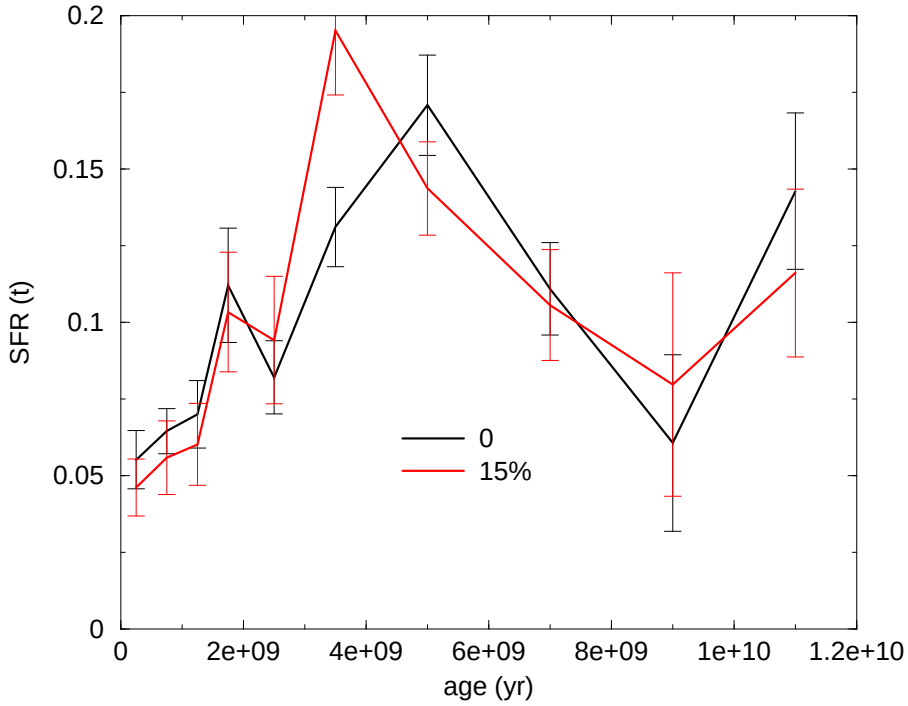

Figure 6.17: Black line and red line are respectively the recovered SFR when the contamination by cluster stars (2 Gyr old) is 0 and 15%.

binary population. The adopted AMR is the usual observational one by Nordström et al. 2004. Before applying the SFR extraction method to real data, we must treat the observational errors. In the previous chapter we saw how the Richardson-Lucy algorithm allows to restore the original CMD corrupted by a point spread function. Here, I will apply the SFR extraction to the Hipparcos CMD that was previously deconvolved by this algorithm (see paragraph 5.6). However, the result of a R-L restoration is a two dimensional histogram and the information on the single stars is lost thus I cannot apply directly the bootstrap technique (randomly drawing values with replacement among the original sample) to determine the variance on the recovered SFR. A trick to avoid this problem is to build bootstrap replicates of the data *before the Richardson Lucy restoration*. Then, each bootstrap data is reconstructed with the R-L algorithm and for each reconstruction the SFR is extracted. From this set of recovered star formation rates one obtains mean and variance for the final SFR.

I applied this procedure to the Hipparcos stars brighter than $M_V = 3.5$ (cleaned from the objects with an identified membership, as described in chapter 3). The R-L algorithm is performed with the PSF built from the observational absolute magnitude error distri-

bution (see chapter 3). Figure 6.18 shows the results: the different curves represent the recovered SFR, after respectively 5, 10, 15, 20, 25 R-L restorations. In order to avoid artifacts, the restoration is stopped at the 25-th iteration (when the bulk of the restoration is done). For comparison, the figure 6.18-a shows the recovered SFR (labeled with 0) when our method is directly applied to the data (without R-L restorations).

The global effect of the restorations is small [‡] and it is focused around 2-3 Gyr. Over the 10th iteration, the solution is very stable and the only change is the enlargement of the estimated uncertainties (because of the noise amplification).

Before discussing the recovered SFR, it is necessary to remember that the implemented Nordström et al. AMR is heavily uncertain for ages lower than 1.5 Gyr and higher than 7 Gyr (see chapter 1), thus the result could be unavoidably biased. Moreover, all the information (at luminosities larger than $M_V = 3.5$) on the SFR older than 7 Gyr comes from evolved stars, giving chances to underpopulation problems. All these points will be discussed further. For the moment, the appearance of the recovered SFR is characterized by:

- A bump in the time interval 10-12 Gyr;
- A modest activity in the time interval 7-10 Gyr (flat);
- A steep increase from 2 Gyr to 6 Gyr;
- A modest activity during the last 1 Gyr (sligthly increasing toward the present).

Sensitivity to the AMR

The SFR we have found represents the most probable result, provided that the ingredients we used in the model are not biased. In fact, I assumed an observational AMR and specific prescriptions for IMF and binaries: while these last two inputs are not crucial (see numerical experiments in sections 6.6 and 6.7), the AMR is very critical (a biased AMR could result in a totally wrong SFR). As already discussed, the Nordström et al. AMR

[‡] This means that the uncertainties in the Hipparcos data (at the luminoisities of our sample) are small. In the previous chapter I showed (using artificial data) that this reconstruction is useful also when the uncertainties are much more larger. The idea was to build a method that could be exported in different problematics (beyond Hipparcos), characterized by larger uncertainties (field CMDs, dwarf galaxies CMDs).

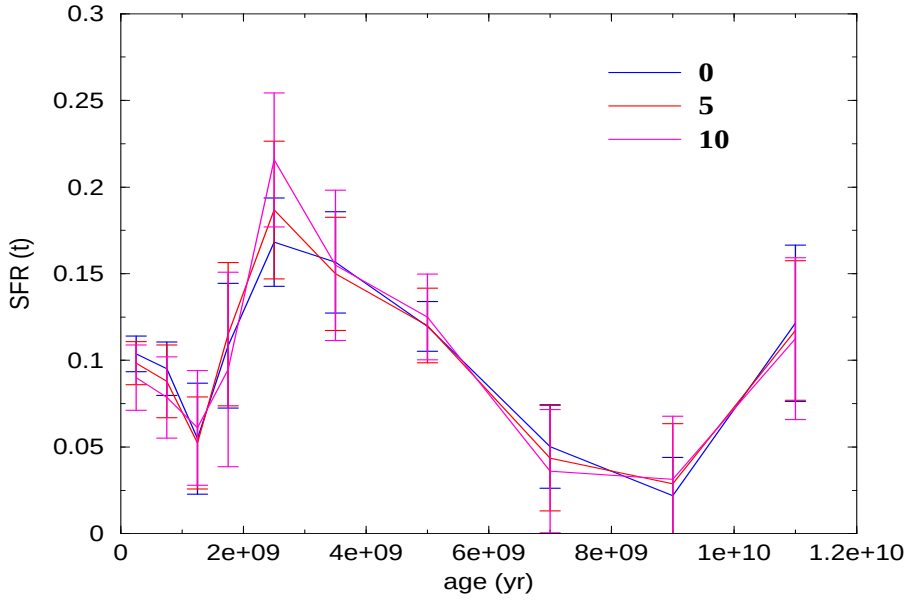

(a) 0, 5, 10 iterations

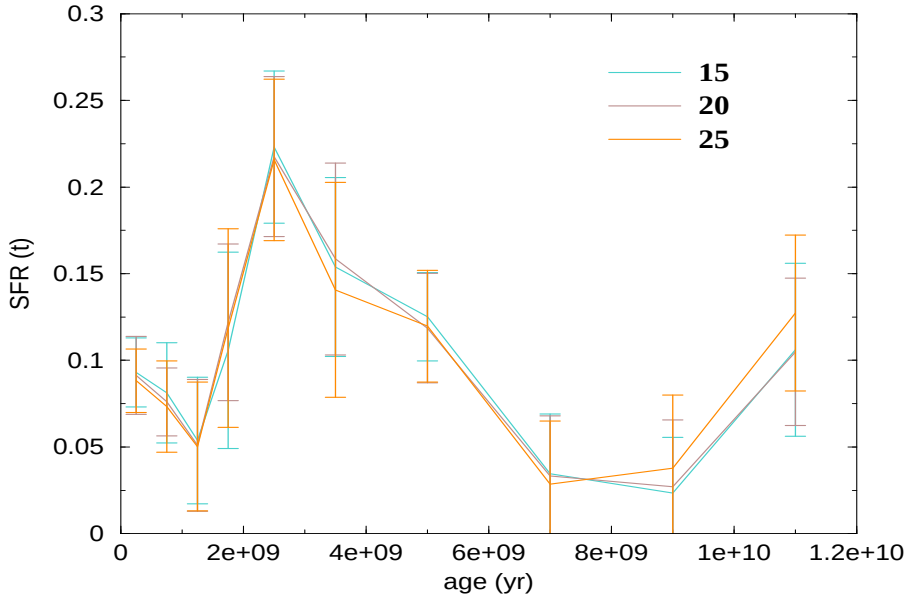

(b) 15, 20, 25 iterations

Figure 6.18: The SFR recovered from the Hipparcos sample. The comparison area involves all stars brighter than $M_V = 3.5$. Different lines show the result after the labeled number of R-L iterations.

was chosen mainly because it arises from a very wide observational sample. However, it is still affected by three important bias:

1. The Nordström et al. AMR was built looking for F-G type stars. This selection was done choosing stars between suitable blue and red color boundaries (by means of $(b-y)$ Strömgren color, which is almost metallicity independent). However, as a consequence of the blue cut-off, the younger metal poor stars are under-represented in the final AMR;

2. Due to the observational errors, the stellar age determination is progressively more and more difficult as a star is close to the zero age main sequence (where the stellar tracks degenerate). Consequently, the Nordström AMR is poorly known for very young stars and the AMR we used below 1 Gyr is essentially an extrapolation;

3. The age determination is a problem also for stars older than 8 Gyr, because at these ages the main sequence stars are low mass stars which evolve in a restricted region of the CMD. As a consequence, the old part of the Nordström AMR is given with huge age errors (the first evidence is the presence of stars older than 13 Gyr).

Although I selected only stars with relative precision on the age better than 25%, the previous points lead to doubts about the recovered SFR for stars younger than 1 Gyr and older than 8 Gyr. In particular, the recovered activity during the last 1 Gyr is partially due to the way the Nordstrom et al. AMR is parameterized in our model. Figure 6.19 shows the effect on the recovered SFR of a different parameterization: the black SFR is the result if the adopted AMR is a polynomial fit (cubic) plus the dispersion, the red SFR is the result when the dispersion alone is implemented. In fact, if we use the fit, the AMR is steeper in the last 1.5 Gyr, if we use only the dispersion the relation is obviously flat at each age.

Sensitivity to the completeness limit

Another point is the adopted completeness limit $M_V = 3.5$: from chapter 4 we understood how the information on the old SFR is enough limited by the completeness limit, with the full information only available with an hypothetical sample complete up to $M_V = 4.5$. With the $M_V = 3.5$ cut-off, the only tracers of the star formation older than 7 Gyr (see

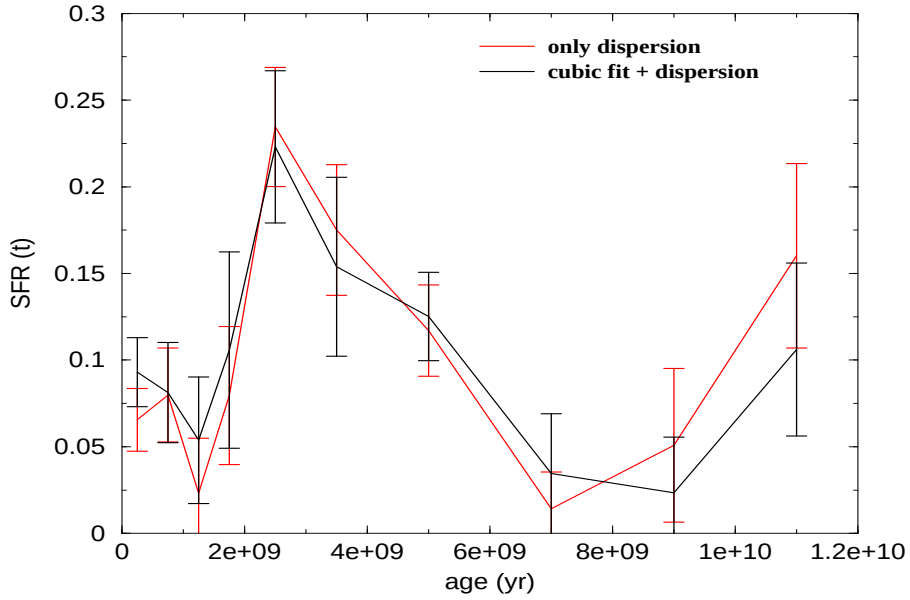

Figure 6.19: Dependence of the result by a different parameterization of the observed AMR. The red SFR is obtained implementing the metallicity dispersion (without trend) of the Nordstrom et al. AMR. The black SFR is the result when is a cubic interpolation of the Nordstrom et al. AMR plus the same dispersion is adopted, see text.

figure 4.12(b)) are red giants, clump stars and subgiants. For this reason, at ages older than 7 Gyr the recovered SFR is certainly undersampled. Thus, the bump between 10 and 12 Gyr could be a pure artifact. Only a deeper volume limited sample could allow to infer a better understanding on the old SFR.

6.13 Kinematical selection

A genuine star formation rate should represent the number of stars born at each time in our volume; this condition can fall, for example when:

α) Old disk stars may be *diffused* in a larger volume, letting the old local SFR undersampled; in fact, the stellar velocities are randomized through chance encounters with interstellar clouds and in star-cloud collisions the stars gain energy increasing the velocities.

β) "Hot" populations may contaminate the sample. Thick disk and halo stars have kinematical properties that could have been fixed before the disk developed. These

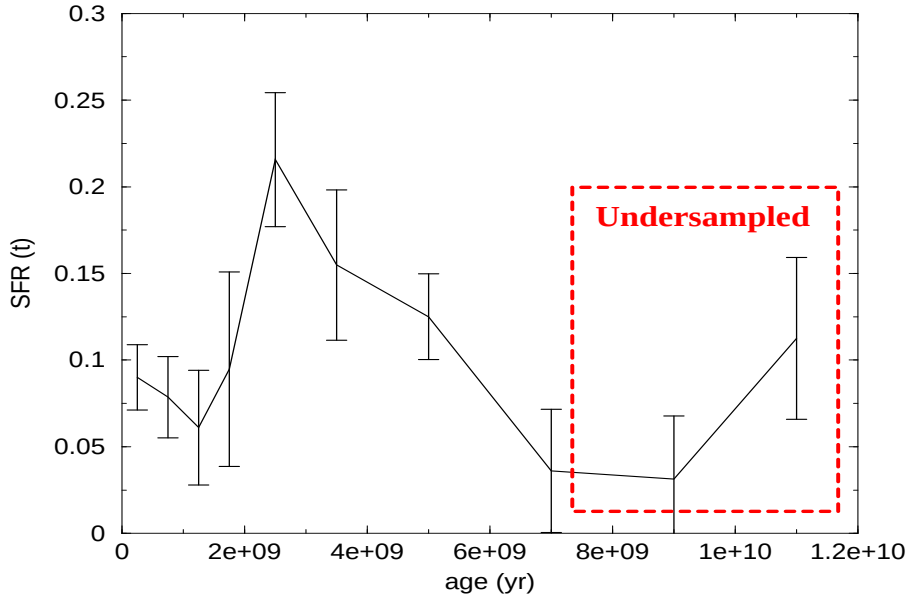

Figure 6.20: The red region identifies the time interval where the recovered SFR is undersampled (because of the magnitude cut at $M_V = 3.5$, the only tracers at these ages are red giant and helium clump stars).

stars experience a much larger volume of the disk stars and they are weakly represented in the solar neighborhood.

In these cases, the recovered SFR would be a mere census of the ages in the solar neighborhood. In order to avoid thick disk/halo contaminations and to check the amount of orbital diffusion by old disk, I computed Galactic velocity components for all stars in the sample and I tested the recovered SFR choicing subsamples kinematically selected.

The Hipparcos mission measured proper motions that, together with the parallaxes, give a chance to study the effects of a selection in tangential velocity V_T. Moreover, for most of the stars in our sample, a measure of the radial velocity is available (from the SIMBAD database [§]). With these data, I computed the Galactic velocities U,V and W for more than 90% of the stars in the sample, corrected for the solar motion relative to the Local Standard of Rest ($U_\odot = +10.0$ Km/s, $V_\odot = +5.2$ Km/s, $W_\odot = +7.2$ Km/s according Dehnen & Binney 1998). Figure 6.21 shows the distribution of U,V and W velocities for all stars in the sample with a measured radial velocity (stars brighter than $M_V \sim 3.5$).

[§]SIMBAD database is available at the following URL: http://simbad.u-strasbg.fr/Simbad

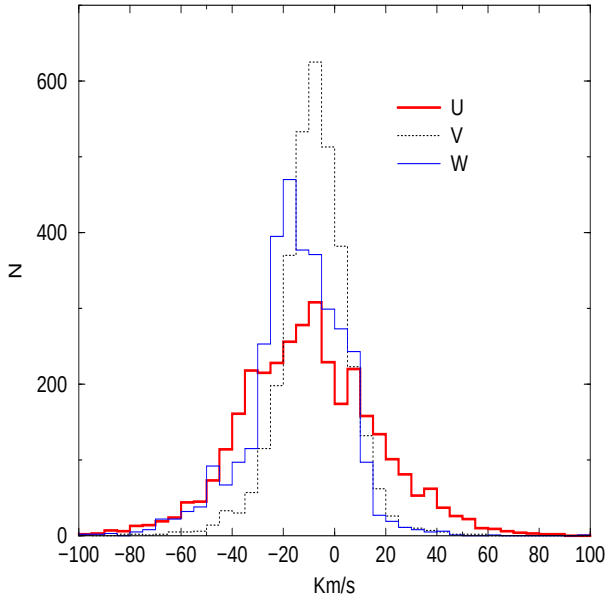

Figure 6.21: Distribution of U,V and W velocities (referred to the LSR) for all stars in the sample with a measured radial velocity and $M_V < 3.5$.

Table 6.1: Characteristic velocity dispersions ($\sigma_{\rm U}$, $\sigma_{\rm V}$, and $\sigma_{\rm W}$) in the thin disk, thick disk, and halo. X is the estimated observed fraction of stars for the given population in the solar neighborhood and $V_{\rm asym}$ is the asymmetric drift with respect to the LSR (values taken from Bensby et al. 2003).

	X	$\sigma_{\rm U}$	$\sigma_{\rm V}$	$\sigma_{\rm W}$	$V_{\rm asym}$
		——— [km s^{-1}] ———			
Thin disk	0.90	35	20	16	-15
Thick disk	0.10	67	38	35	-46
Halo	0.0015	160	90	90	-220

In order to search for stars with thin disk properties I needed a kinematic criteria. Table 6.1 summarizes recent results for the kinematic properties of the thin disk, thick disk and halo (values from Bensby et al. 2003).

Figure 6.22 displays the CMD of fast stars (red dots) superimposed to the total sample (black dots): panels (a) and (b) represent respectively stars with kinematic properties outside 2σ, 1σ the thin disk mean velocities.

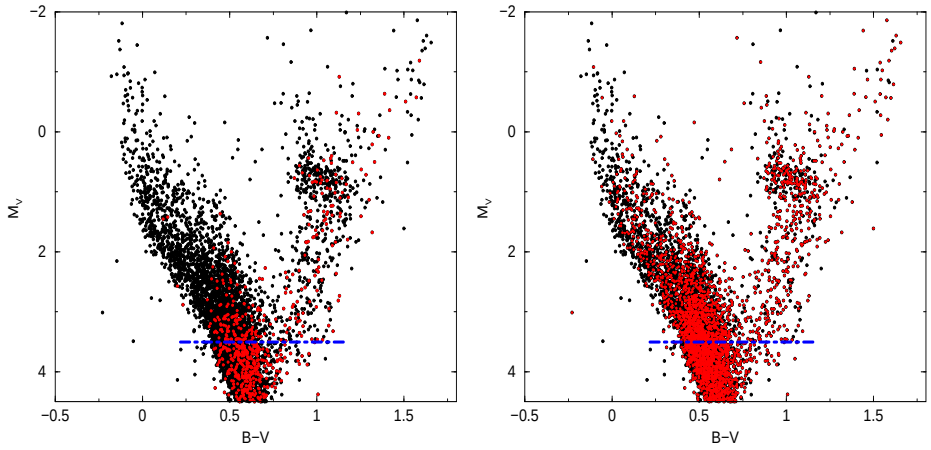

(a) (b)

Figure 6.22: Black dots: full sample. Red dots: stars with velocities outside 2σ (panel a) and 1σ (panel b) from the mean thin disk values. The blue horizontal line is the completeness limit ($M_V = 3.5$).

Before applying the SFR extraction on the kinematical selected data, I performed the same selection also on the Nordström age metallicity relation (the AMR implemented in the SFR extraction code). The result is presented in figure 6.23: even if the $[Fe/H]$ dispersion slightly decreases with stellar velocity, this value is still very high and no trend in the AMR is recognizable. For this reason, I adopted the same AMR I used for the full sample without kinematic selection (see the discussion in chapter 1). This result is related to the debate on the existence of a distinct chemical history for disk and thick disk. In fact, it is well known that high velocity stars belong to more extended structures (thick disk and halo), in particular Sandage (1987) and Casertano et al. (1990) used kinematic measurements to trace the thick disk population, but it is much less obvious that these stars reveal an age-metallicity relation well distinguished from the disk AMR. Metallicity distributions of the thick disk and thin disk do not allow for an unequivocal classification. Some authors (see e.g. Gilmore et al. 1989, Bensby et al. 2005) argue that the thick disk is a completely separated Galactic component (that is, it has distinguishable kinematic and chemical properties), in particular Bensby et al. (2005) claims to determine a specific AMR. A different conclusion is reached e.g. by Norris & Green (1989) and Norris & Ryan (1991), where the thick disk is found as the high velocity dispersion tail of the old

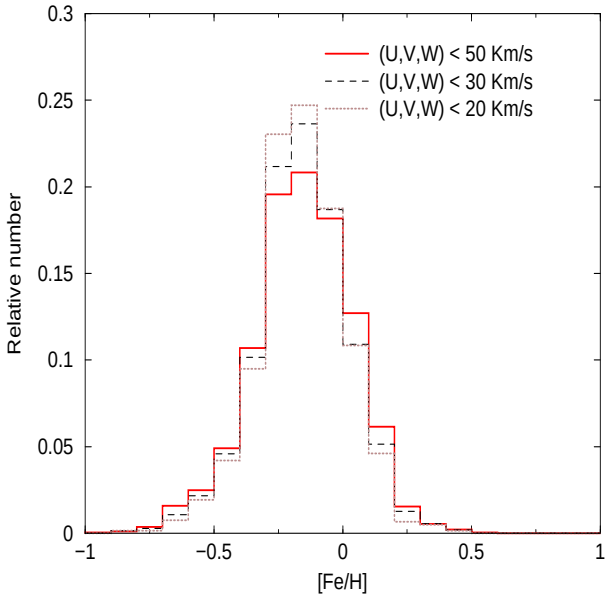

Figure 6.23: $[Fe/H]$ distributions (data by Nordström et al. 2004) for stars with the labeled kinematic selection.

disk.

Figure 6.24 shows the recovered SFRs (after 15 R-L restorations) when the sample is kinematically selected. In particular, the result in panel (a) is found selecting objects with Galactic velocities within the velocity ellipse at 2σ for the thin disk. Result in panel (b) is found for objects with velocities within the velocity ellipse at 1σ for the thin disk.

The cut at 2σ excludes essentially halo and thick disk objects. In this case (figure 6.24, panel a), the recovered SFR is almost identical to the one without any selection. One explanation is that the contribution of thick disk and halo stars, for the period 1-8 Gyr, is minimum; this result confirms the general findings: the thick disk, if it exists, seems older than thin disk; e.g. about 8 Gyr for Fuhrman (1998), from 7 to 13 Gyr (with an average of 9.6 ± 0.3 Gyr) for Soubiran & Girard 2005. In addition, the number density of local thick disk stars is a small fraction ($\sim 8\%$) of the thin disk stars. Also this result is confirmed by many works: Gilmore & Reid (1983) and Chen (1997) claim a 2% fraction, Robin et al. (1996) find 6%, Soubiran et al. (2003) find a 15% fraction.

In contrast, removing stars out of 1σ should exclude:

- low velocity tails of halo and thick disk;
- disk stars whose orbits explore large scale heights (200-300 pc);

In this case, the recovered SFR (fig. 6.24, panel b) is slightly younger: the peak at 3 Gyr is lowered, while the activity in the last 1.5 Gyr is increased. However, the variations are within the statistical uncertainties (between 1 and 2 σ of acceptance) and the global trend is preserved.

In conclusion, the recent SFR (last 6 Gyr) seems not to suffer of a significant dynamical diffusion. In this case, a correction for a possible disk depletion due to fast stars, does not really matter: within our level of acceptance, the recovered SFR is a genuine local SFR and not a mere local age distribution.

Because of the theoretical difficulties to reproduce the red clump stars (see the discussion in chapter 4), the analysis was repeated excluding all stars with $B-V>0.8$. In this case, because the excluded region involves stars of all ages, the recovered SFR (see figure 6.25) is slightly different at all ages (but still within the $1\,\sigma$ uncertainties), with a major effect around 10 Gyr.

6.14 Sensitivity to the adopted $(Z/X)_{\odot}$ value

Recent analysis of spectroscopical data using three dimensional hydrodynamic atmospheric models (see Asplund, Grevesse & Sauval 2005 and references therein) have reduced the derived abundances of CNO and other heavy elements with respect to previous estimates (Grevesse & Sauval 1998, GS98). Thus the Z/X solar value decreases from the GS98 value $(Z/X)_{\odot}=0.0230$ to $(Z/X)_{\odot}=0.0165$. GS98 already improved the mixture by Grevesse & Noels (1993), GS93, widely adopted in the literature ($(Z/X)_{\odot}=0.0245$), mainly revising the CNO and Ne abundance and confirming the very good agreement between the new photospheric and meteoric results for iron. As already discussed our tracks are calculated for the GN93 solar mixture.

The change of the heavy element mixture might have two main effects: 1) the change of theoretical tracks at fixed metallicity which however has been shown to be negligible (see Degl'Innocenti, Prada Moroni, Ricci 2005); 2) the variation of the inferred metallicity from the observed $[Fe/H]$. This could be important for our purposes due to the adoption of the observative age-$[Fe/H]$ relation. Figure 6.26 compares the recovered SFR obtained using Asplund, Grevesse & Sauval (2005) and GS93; one finds that the differences are

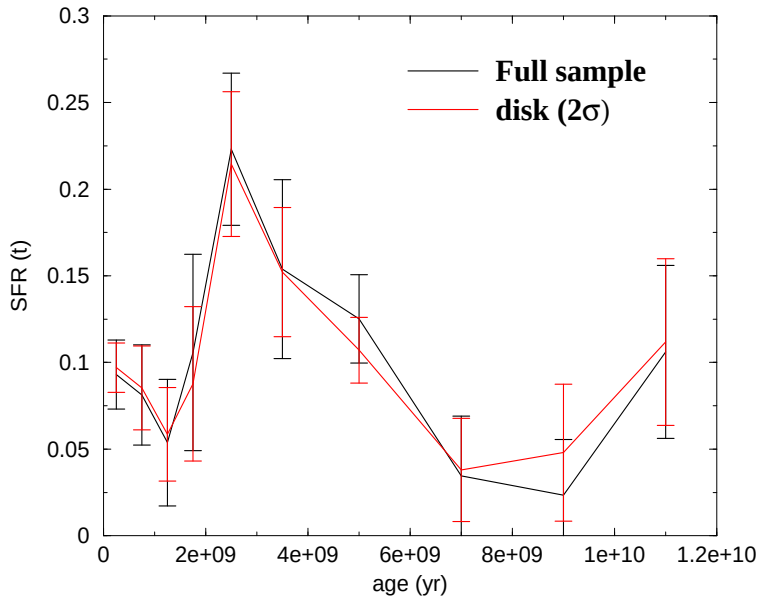

(a)

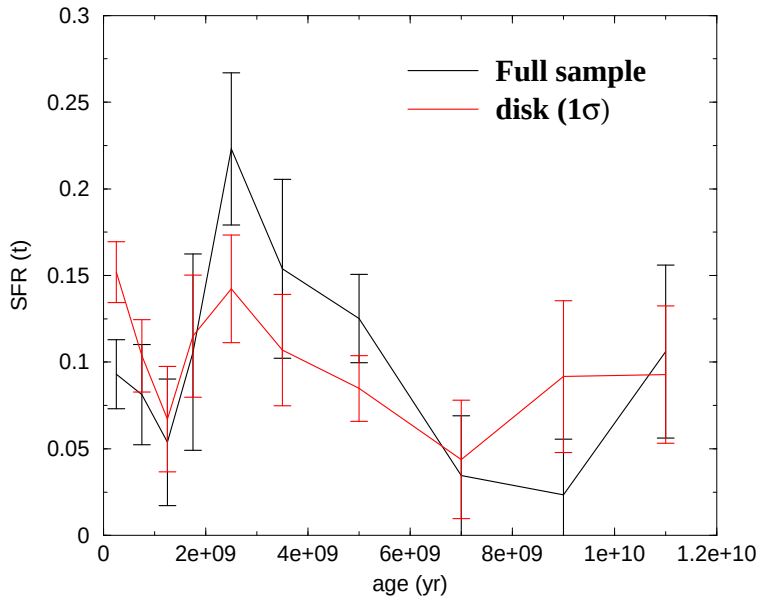

(b)

Figure 6.24: Black line: the recovered SFR using the full sample. Red line: the SFR recovered from stars with Galactic velocities within the velocity ellipse at 2σ (panel a) and at 1σ (panel b) the velocity ellipse of the thin disk.

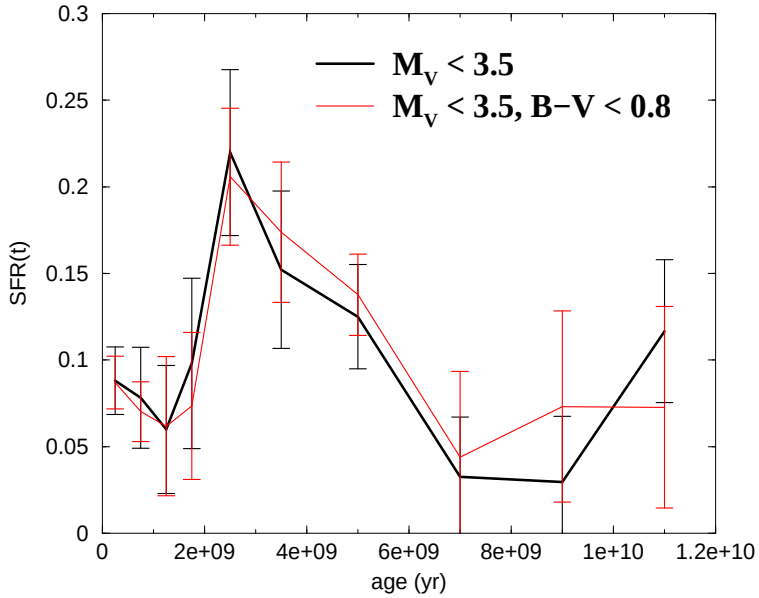

Figure 6.25: Comparisons between the recovered SFR obtained from the full sample (black line) and from a selection of stars with $B - V < 0.8$.

within the statistical uncertainties.

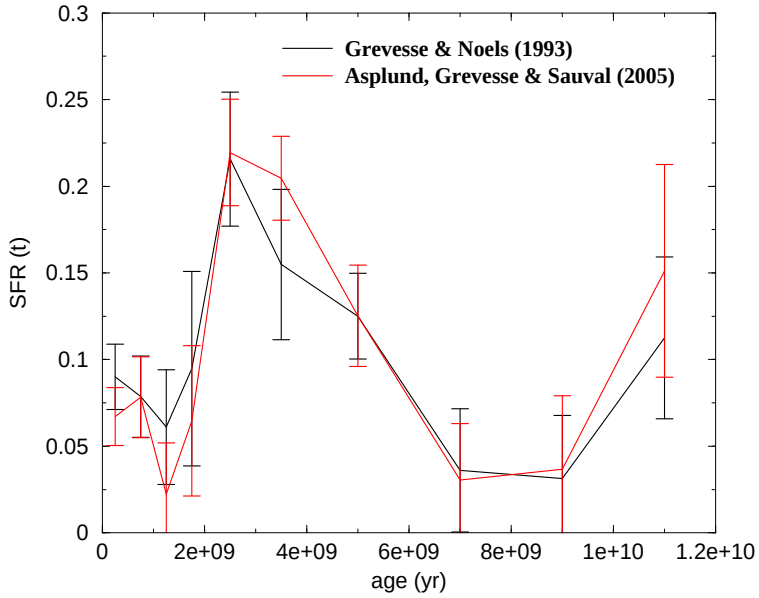

Figure 6.26: Comparison between the recovered SFR obtained adopting the Z/X solar value by Asplund, Grevesse & Sauval 2005 and by GS93.

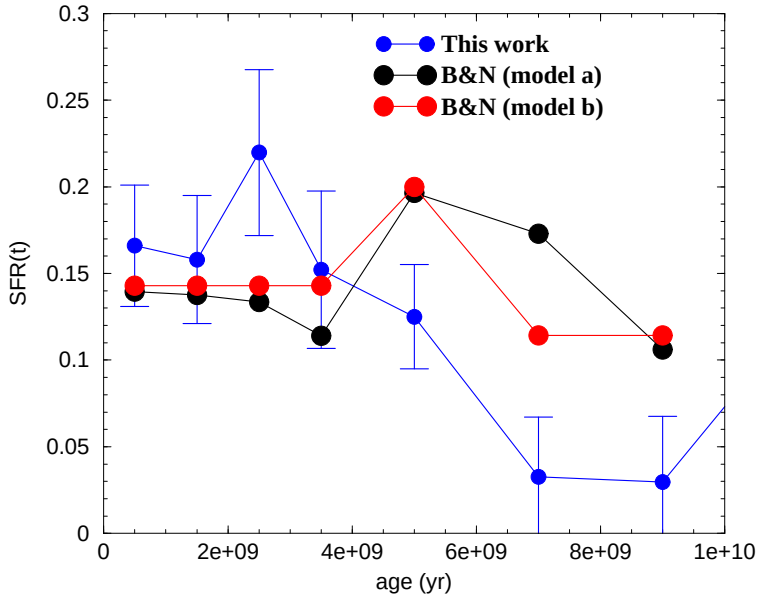

Figure 6.27: Our recovered SFR (blue curve) compared with that of Bertelli & Nasi (B&N) (two acceptable models are shown), see text.

6.15 Discussion and Outlooks

In this paragraph the results of this thesis are compared with similar works on the local available in the recent literature. In general, three approaches have been used. One is the direct comparison as in this thesis, between the data and artificial CMDs using a χ^2 statistic (even though our observational error treatment is Bayesian, the comparison is still a direct method). Examples of this approach are Bertelli & Nasi (2001) and Schröder & Pagel (2003). The second approach is the Bayesian method, followed by Hernandez et al. (2000) and Vergely et al. (2002). The third approach exploits the variation with stellar age of chromospheric activity as in Rocha-Pinto et al. (2000).

Bertelli & Nasi (2001) used a similar stellar sample (Hipparcos stars within 50 pc with a completeness limit at $M_V = 4.5$) and a method close to ours (they built artificial CMDs). From the statistical point of view, there is no treatment of the observational errors (this is partially justified by the large CMD binning). The authors found a local SFR that is independent of the chosen IMF, with the exception of low exponents (the value 1.3 is rejected). The figure 6.27 compares the SFR they recovered with our result for solar neighborhood. The recent SFR (last 4 Gyr) is quite similar, while the older one is characterized by a different slope (the Bertelli & Nasi is flat, our SFR is steep). This

disagreement can arise from many differences between the two models:

- The adopted evolutionary tracks: Bertelli & Nasi used the Padua stellar evolutionary tracks (Girardi et al. 1996) which includes overshooting with an efficency of about $0.12\,H_P$ in the mass range $1.0\,M_\odot < M < 1.4\,M_\odot$ and ≈ 0.25 for higher masses. Our code implements the Pisa stellar tracks (Cariulo et al. 2004, Castellani et al. 2003, Castellani, Degl'Innocenti, Marconi 1999). Even if the red clump region is poorly reproduced by the Pisa stellar tracks, while the Padua tracks match better (see discussion in chapter 4), I showed (see figure 6.25) that clump and giant stars have a low influence on the recovered SFR for the last 6 Gyr.

- In the Bertelli & Nasi model the stars are uniformly distributed in the metallicity range $0.008 < Z < 0.03$. In contrast, I adopted the observational AMR by Nordström et al. (2004). Thus, their mean composition (solar) is metal richer than our composition (using Grevesse & Noels 1993, the mean $[Fe/H]$ value ~ -0.15 corresponds to $Z \approx 0.012$).

- The binaries. Bertelli and Nasi adopt something between 30 and 70 percent of binaries ("decreasing from 70 percent for the more massive primaries to about 27 percent at the faint limit Mv=4.5"), while my comparisons are without binaries. In main sequence, the luminosity of a star depends on the mass, thus a binary system can mimic a different mass (and a different age); we already showed that a not huge percentage of binaries has no influence on the results, however the amount of binaries introduced by the authors could lead to some difference (see discussion in section 6.7).

However, the recovered SFR increases toward the present, that is in agreement with the present result (although our SFR is steeper).

In conclusion, our result is consistent with Bertelli & Nasi (2000), and thus the star forming history seems to be real, not an artifact of the inputs.

A similar approach is followed also in Schröder & Pagel (2003). This work used Hipparcos stars with $|z| < 25$ pc and within 100 pc in distance. Artificial CMDs were built adopting the evolutionary calculations by Eggleton (1973) for solar metallicity. The effect of different chemical composition was simulated by smearing the single metallicity

CMD with a Gaussian spread. The SFR and the IMF were inferred by comparing the artificial CMDs with the observed one up to a limiting magnitude $M_V = 4$, and matching the star counts in particular regions (upper main sequence, clump, subgiants, etc.). The recovered local SFR is slowly increasing towards recent times and the authors attribute this result to the dilution of thin disk stars as they "diffuse" into larger scale heights (by dynamical diffusion). In order to transform to a column-integrated SFR they adopted a dynamic diffusion timescale of about 6 Gyr. The final result is only slightly different from the local SFR (except the recent 1 Gyr, where the authors correct for a radial mixing). *In practice, this result confirms our finding that the dynamical diffusion of orbits has a low impact on the recent 5-6 Gyr.*

The second approach to be discussed is the Bayesian method: Hernandez et al. (2000) used an inversion method on the Hipparcos stars brighter than $M_V = 3.15$, deriving the local SFR for the last 3 Gyr. The implemented evolutionary models were the Padua isochrones (Girardi et al. 1996) with $[Fe/H] = 0$. In figure 6.28-a, it is shown our SFR against their findings for the last 3 Gyr (the higher time resolution of Hernandez et al. SFR made a rebinning necessary).

The two results are compatible, although our time resolution does not allow to resolve the SFR behavior found by the authors showing a cyclic pattern with a period of 0.5 Gyr (see figure 6.28-b). Considering that their data are essentially our data, the differences could be addressed to:

- The adopted metallicity: Hernandez et al. (2000) implemented a solar value ($[Fe/H] = 0$) without spread, while I adopt the Nordström age metallicity relation (whose mean metallicity is lower than solar);

- The stellar isochrones: they used Padua isochrones (Girardi et al. 1996), the same as Bertelli & Nasi (2001);

- The IMF: they implemented a power law with exponent 2.7 (steeper than our value 2.35).

Moreover, their technique was very different from our method, thus the good agreement between the two results seems an independent confirmation of our method.

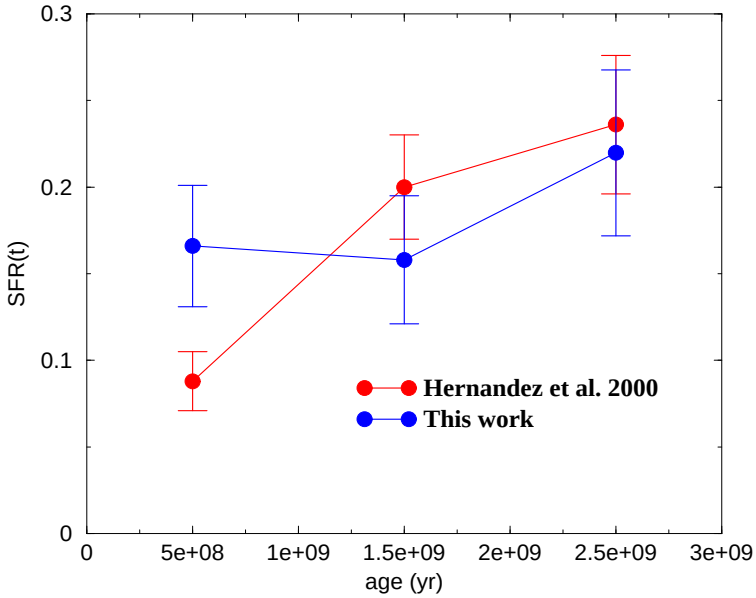

(a)

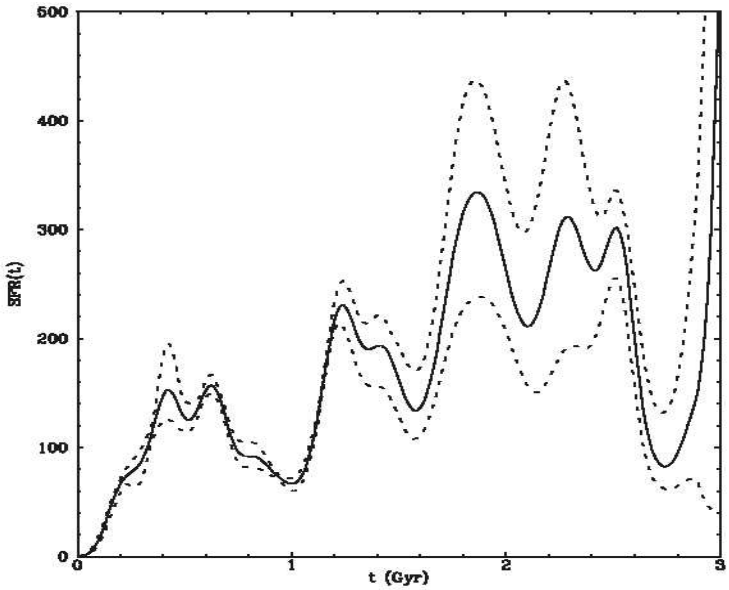

(b)

Figure 6.28: (a) Our recovered SFR (blue curve) compared with the Hernandez et al. (2000) SFR (rebinned). (b) Hernandez et al. (2000) SFR with the original resolution.

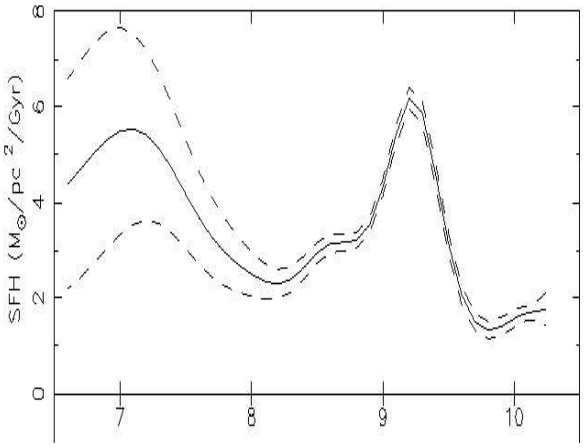

Figure 6.29: Vergely et al. (2002) recovered SFR (in abscissa it is reported the age (yr) in logarithmic units).

Vergely et al. (2002) used a similar inversion method. The authors determined simultaneously the star formation history, the AMR and the IMF from the Hipparcos stars brighter than $V = 8$. Here, the parameters have a probability density (prior information) and the comparison of the apparent CMD with the observed data is an iterative process. The authors adopt a much larger sample (not magnitude limited) and the AMR is not constrained. Their result is the column SFR. The surprising feature is the similarity between their result (not local), see figure 6.29, and our local SFR. In particular, their column-integrated SFR decreases with lookback time on a timescale of 4-5 Gyr that is essentially the same our result.

This confirms our result and it can mean:

- *the local stellar population is not depleted in the past, but the derived SFR represents a genuinely lower activity;*

- *no significant dynamical diffusion has taken place on a time scale of 4-5 Gyr.*

Rocha-Pinto et al. (2000) provided a SFR based on chromospheric emission ages for a sample of solar-like stars within 80 pc. Their result shows enhanced SFR episodes at 0-1 Gyr and 2-5 Gyr, that are approximately similar to our result, and at 7-9 Gyr (but it could be a spurious effect due to the low chromospheric emission for these ages). Also in this work, the effect of dynamical orbits diffusion is not severe and does not affect the general trend of the SFR.

Thus our result seems to represent a realistic SFR of the solar neighborhood. The recovered SFR is quite independent of the kinematical selections, suggesting that all the stellar generations (in the last 6 Gyr) are well represented and stars are not diffused in a larger volume. The SFR is consistent with other studies that used a similar sample (Bertelli & Nasi 2000) and different techniques (Hernandez et al. 2000). *The result that our local SFR is close to the column SFR (Vergely et al. 2002) is important, indicating that our result is not local but may actually represent a global variation in the star forming activity of the disk.*

Once we have checked that dynamical diffusion has not been so efficient in the last 5-6 Gyr and the internal assumptions of the model (IMF, binaries, adopted solar mixture) have a low impact on the result, we can discuss the physical implication of our results. Our SFR decreases with lookback time, on a timescale larger than 1 Gyr. This result leaves room for a Galactic triggering event. This timescale is longer than Galactic disk rotation (< 1 Gyr), essentially ruling out the possibility that this phenomenon is local. This result is also difficult to explain if the Galactic disk is a close box (see e.g. van den Bergh 1962, Schmidt 1963): the resulting SFR would be *increasing* in age (opposite to our result), following the normal exhaustion of the gas content and an increased production of inert remnants. Even if the disk is periodically in time refilled with gas, our result is difficult to explain : the resulting SFR would be quite *constant* in time (unless the infall is huge, but in this case the age-metallicity relation would change relative to observational evidence).

Thus, the recovered SFR seems to indicate some kind of *induced event*, for example by the accretion of a satellite galaxy. However, the tracks left by a such an intruder should be recognized in the age-metallicity relation, while the survey of Nordström et al. (2004) shows practically no change in mean metallicity from 1 to 12 Gyr. The probe of an accretion should be evident analyzing the kinematical properties of stars in different age bin, but the methods to obtain stellar ages are still affected by large errors (see discussion in section 6.12).

Much larger surveys of stellar ages and metallicities as a function of galactocentric distance and kinematics are needed to test our hypothesis: comparing results from different places of the Galaxy could make clear if the recovered event is really a global disk event.

6.16 Conclusions and future work

The aim of this study was to develop a method for recovering as much information as possible from binned color-magnitude diagrams (CMDs) with a newly developed method to recover the local SFR from the Hipparcos color-magnitude diagram. Therefore employing a Galactic model for solar neighborhood. Artificial stars were created by a random choice of mass and age from the assumed IMF and SFR(t), interpolated on a grid of evolutionary tracks whose metallicity is determined by the adopted age-metallicity relation (AMR) and chosen fraction of these stars were selected as binaries and coupled with another star randomly chosen with the same procedure. An artificial CMD is thus generated. The parameter space is searched for the combination of parameters giving the minimum difference, using a maximum likelihood statistic, between the theoretical and the observational CMDs.

To reduce the computational time, a set of partial CMDs was built, using them to produce each CMD; each partial CMD was generated with a step star formation, uniform in a given time interval and zero elsewhere. Thus, for each combination of IMF, binary distribution, and AMR, the CMD corresponding to any SFR was computed as a linear combination of the partial CMDs.

In order to check the importance of the different parameters (IMF, binaries, AMR), I tested the algorithm on artificial "Hipparcos" CMDs (fixing the minimum luminosity at $M_V \sim 3.5$, the completeness limit of the Hipparcos sample for stars within 80 pc). *At these luminosities, the results indicate that the recovered SFR is weakly influenced by the "correct" choice of IMF and binary fraction, but it is strongly influenced by the adopted AMR*. In particular, this result was checked assuming the observational AMR for the solar neighborhood by Nördstrom et al. (2004): in spite of the large dispersion of this relation, the simulation on the artificial CMD indicate that most of the information for the underlying SFR is still recovered. Finally, I applied the algorithm to real Hipparcos data. In contrast with artificial CMDs, the first problem was the presence of observational uncertainties (due to photometric and parallax errors). To take these uncertainties into account, I considered an innovative point of view: a CMD is an image, the intensity being the number of stars in a bin of effective temperature and luminosity, affected by a point spread function that originates from the distributions of the errors in the parallax

and in the photometry. Thus I treated the Hipparcos CMD with the same techniques that have been used for image restoration. In practice, I implemented the Richardson-Lucy algorithm to the analysis of color-magnitude diagrams affected by observational uncertainties: I converted the CMD into an image and, using a restoring point spread function function derived from the observation, "cleaned" the CMD (taking out the observational errors). Numerical experiments with artificial CMDs demonstrate good recovery of the original image and I established convergence rates for ideal cases with single Gaussian uncertainties and Poisson noise using a χ^2 statistic. Finally, this technique was applied to the Hipparcos sample of the solar neighborhood, recovering the best "cleaned" data set with which to perform analyses of the local star formation rate.

Assuming the observational AMR by Nördstrom et al. (2004), I tried to recover the SFR from this "cleaned" CMD. The resulting SFR indicates that *the recent local history of the Galactic disk is increasing from the past to the present with some irregularities*. The mean value increases very steeply from 6-7 Gyr ago up to 2 Gyr, in a way qualitatively similar to the findings of Hernandez et al. (2000) and Bertelli & Nasi (2000). In particular, this result is is quite independent against kinematic selections, suggesting that:

1. The local contamination of halo and thick disk stars is negligible and/or these populations are older than 6 Gyr (the possibility to infer the older SFR is hindered by the completeness limit in absolute magnitude);

2. In the last 5-6 Gyr, all the stellar generations are well sampled; in other words, the recovered local SFR is not biased by dynamical diffusion and the local volume is not "depleted" by old disk stars. Moreover, the recovered column-integrated SFR by Vergely et al. (2002) is very similar to our local SFR, suggesting that the dynamical diffusion was not so efficient in the last 5-6 Gyr.

The timescale of the recovered SFR seems too long (larger than the dynamical timescale) to be attributed to local events: an accretion of a satellite galaxy is suspected.

This work has developed a general method to extract information (in our case, the local SFR) from a color-magnitude diagram. The observational CMD is "cleaned" with a Richardson-Lucy algorithm, then the chosen information (SFR) is recovered. In this last process, all the parameters with a not critical influence are fixed to a given value. However, although neither the IMF nor the binary fraction are critical inputs for recovering the

SFR when $M_V \lesssim 3.5$, this is not true using fainter cutoff luminosity. In this case, new numerical experiments would be necessary in order to explore the sensitivity of the result to the adopted parameters. The method can be easily applied to the analysis of the SFR of the CMD of dwarf galaxies, for which the distance among the stars is negligible with respect to distance of the Galaxy from us but where interstellar inhomogeneities may be the principal uncertainty.

A natural extension of this method involves the analyses of not-local Galactic fields far beyond the solar neighborhood (see e.g. Ng et al. 1997, Robin et al. 2000): adopting spatial distributions for the different Galactic components, it would be possible to study the global properties of the Galaxy. The typical data for a similar analyses would be the color-apparent magnitude diagram for field observations (stars along the line of sight, with unknown distance, chemical composition, mass and age). Such an analyses however introduces a new level of complexity. Among them: 1) the dynamical diffusion of orbits, that doesn't affect the nearby sample, should be carefully treated to study the field stars; 2) the presence of associations and moving groups becomes more pronunced since without kinematical measurements they are difficult to detect and remove from field CMDs; 3) the mixing of different populations (young disk, intermediate disk, old disk, thick disk, halo) with specific scale lengths requires adopting different AMRs (or metallicity ranges); 4) Galactic fields involve masses below $1\ M_\odot$ (the minimum mass of our Hipparcos sample), thus it is necessary to explore the low mass regime of the IMF; moreover, the comparison with different fields could clear if the IMF is a real universal quantity; 5) the adoption of different Galactic populations (with specific spatial distributions, IMFs and AMRs) involves much more parameters to explore; 6) the adoption of extinction laws and dust and gas spatial distributions.

Finally, in contrast with local stars, whose the uncertainties affecting the CMD are mainly due to parallax errors, for field stars the uncertainties are mainly photometric: the modified version of the Richardson-Lucy algorithm should use a point spread function whose the width varies as function of the magnitude (increasing towards faint magnitudes where the photometric error is larger).

For Galactic field stars the open questions for future research are manifold. In general, we do not expect that the solar neighborhood SFR can be extended to the whole

Galaxy (because the oldest stars are expanded to larger scale heights). Vallenari et al. (2000) adopted the disk SFR that Bertelli et al. (1999) recovered from the Hipparcos data in a Galactic model and were unable to reproduce the observed CMDs in several directions (concluding that the solar neighborhood cannot be representative of the whole disk). Comparing the results for local and field stellar samples could give useful information. The local sample is the ideal place to study the disk stars, but it is less informative about thick disk stars. In contrast, field stars are most informative on the thick disk (see e.g. Wyse & Gilmore 1995). However, the breakthrough about those issues is linked to the future availability of the Gaia mission, with which it will make possible to study the 3D structure of the Galaxy at much further distances than it is now possible from the solar neighborhood data provided by Hipparcos.

A

Probability rules

Let A and B be propositions which can take only two values, true or false. Calling P(A) the probability that A is true, the basic rules of probability are:

1. The probability of any event A is a real number between zero and one:

$$0 \leq P(A) \leq 1 \tag{A.1}$$

2. The probability of a certain event, Ω (tautology, a proposition that is certainly true), is

$$P(\Omega) = 1 \tag{A.2}$$

3. The probability of an event which is the join (union) of the two:

$$P(A \cup B) = P(A) + P(B) - P(A \cap B) \tag{A.3}$$

where $A \cap B$ is true only when both A and B are true, while $A \cup B$ is true when at least one proposition is true.

The conditional probability $P(A|B)$ is the probability of an event A given that event B occurs or has occurred, we can get another formula for the intersection of events $A \cap B$:

$$P(A \cap B) = P(B \cap A) = P(B|A)P(A) = P(A|B)P(B) \tag{A.4}$$

which can extended to an arbitrary number of events; for three such events, for example:

$$P(A \cap B \cap C) = P(A|B \cap C)P(B \cap C) = P(A|B \cap C)P(B|C)P(C) \tag{A.5}$$

If the status of B does not change the probability of A, and vice versa around, then A and B are said to be *independent*. In that case, $P(A|B) = P(A)$, and $P(B|A) = P(B)$, which, when inserted in equation (A.7), yields

$$P(A \cap B) = P(A)\, P(B) \tag{A.6}$$

If we call $\bar{A}$ the negation of A, $A \cup \bar{A}$ is a tautology and from equations A.2 and A.3

$$P(A) + P(\bar{A}) = 1 \tag{A.7}$$

The natural generalization of this result is when we consider a complete class of hypotheses H_J that together form a tautology (they are *exhaustive*, formally $\cup_i H_i = \Omega$) and *mutually exclusive* (formally $H_j \cap H_k = 0 \ \text{if} j \neq k$), using rules A.7 and A.3 we find two properties:

$$\sum_j P(H_j) = 1 \tag{A.8}$$

$$P(A) = \sum_j P(A|H_j)P(H_j) \tag{A.9}$$

A.1 Bayes' theorem

This theorem derives from the symmetry of the equation A.9. If we have two propositions E_i and H_j, the equation A.7 gives:

$$\frac{P(H_j|E_i)}{P(H_j)} = \frac{P(E_i|H_j)}{P(E_i)} \tag{A.10}$$

The intersting feature of this equation is that the new condition E_i changes our hypothesis H_j by the same updating factor by which the condition H_j alters our "belief" about E_i. Thus:

$$P(H_j|E_i) = \frac{P(E_i|H_j)P(H_j)}{P(E_i)} \tag{A.11}$$

which is the usual way to show *Bayes' theorem*. Therefore in general:

$$P(H_j|E_i) = \frac{P(E_i|H_j)P(H_j)}{\sum_j P(E_i|H_j)P(H_j)} \tag{A.12}$$

An useful feature is that if several data sets are available, we just have to insert in the Bayes formula the *likelihood* $P(E|H)$. For one observation:

$$P(H|E_1) \propto P(E_1|H)P(H); \tag{A.13}$$

for two:

$$P(H|E_1 \cap E_2) \propto P(E_2|H \cap E_1)P(E_1|H)P(H), etc. \tag{A.14}$$

With the rule A.7 this equation can be written as:

$$P(H|E_1 \cap E_2) \propto P(E_1 \cap E_2|H)P(H) \tag{A.15}$$

From equations (A.14) and (A.15) one finds that the equation A.14 gives the same result of a single inference that takes into account both E_1 and E_2. For many independent data samples E_i we obtain for the likelihood:

$$P(E|H) = \prod_i P(E_i|H) \tag{A.16}$$

thus, the final likelihood is the product of the likelihoods.

B

Nelder Mead simplex method

A simplex $\mathcal{S}$ is defined as a geometric shape with $N+1$ vertices in an N-dimensional space $\mathbb{R}^N$ (in two dimensions, it's a triangle). For our problem the simplex is the function χ_P evaluated in $N+1$ points (each point is a point of the N-dimensional parameter space).

The Nelder Mead simplex method is an iterative algorithm starting from an initial simplex. The process is a nothing more of a set of clever strategic moves (spatial movements of three types: reflection, expansion, contraction) to reach the minimum for χ_P.

The first step is to order the $N+1$ evaluations of χ_P (vertices of the initial simplex): the point of maximum is the worst point (MAX), the minimum is the best one (MIN). Fixing the worst point, the others N points form a hyperplane (points 1,2,3 in the figure (B.1), 3-D case). The first movement consist on to apply a reflection to this worst point respect to the hyperplane and to evaluate the χ_P in the new point NEW (see figure B.1).

If $\chi_P(NEW)$ is between the second highest point and the lowest point of the initial simplex, we replace MAX with NEW in the simplex. We have a new simplex.

If $\chi_P(NEW)$ is lower than all $N+1$ points we have found the new best point, and so the algorithm try another point in the same direction (to check if χ_P decreases further). We call this point $NEW2$. The lower between NEW and $NEW2$ is the candidate to replace the point MAX. In case of $NEW2$, the new simplex has an increased volume (operation called expansion, see figure (B.2)).

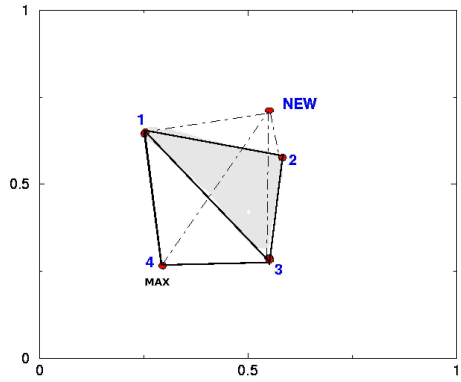

Figure B.1: Simplex in a 3-dimensional space of parameters. Points with label 1, 2, 3,4 form an initial simplex. The point labeled with NEW is the reflection of the point where χ_P is maximum (labeled with 'MAX') respect to the plane with vertices 1, 2, 3.

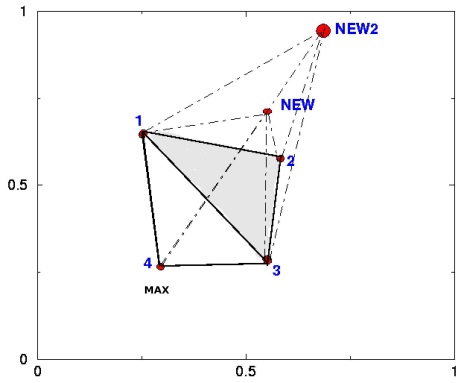

Figure B.2: The new simplex in case of expansion (point $NEW2$).

If $\chi_P(NEW)$ is greater than the second highest point, the simplex pull down in all direction until it finds a point where χ_P is lower than MAX (operation called contraction, see figure (B.3)).

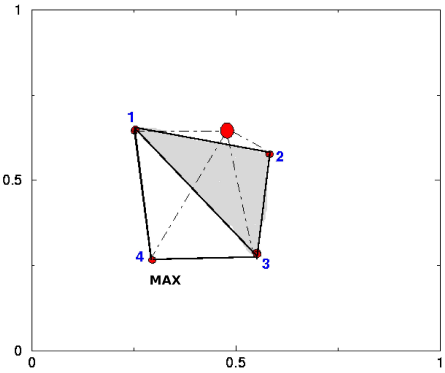

Figure B.3: The new simplex in case of contraction.

References

Allende Prieto, C., Barklem, P. S., Lambert, D. L., Cunha, K. 2004,A&A, 420, 183

Andersen, J. 1991, A&A Rev., 3, 91

Aparicio, A., Gallart, C., Bertelli, G. 1997a, AJ, 114, 669

Aparicio, A., Gallart, C., Bertelli, G. 1997b, AJ, 114, 680

Arenou F., Lindegren L., Froeschle M., et al. 1995, A&A, 304, 52

Arenou F., Luri X., 1999, "Distances and absolute magnitudes from trigonometric parallaxes", ASP Conference Series 167, D. Egret and A. Heck, p. 13

Asplund, M., Grevesse, N., & Sauval, A.J. 2005, in "Cosmic Abundances as Records of Stellar Evolution and Nucleosynthesis", eds. F.N. Bash, & T.J. Barnes, ASP Conf. Series, 336, 25

Baade, W. 1944, ApJ, 100, 137

Baraffe I., Chabrier G., Allard F., Hauschildt P. H., 1997, A&A, 327, 1054

Baraffe I., Chabrier G., Allard F., Hauschildt P. H., 1998, A&A, 357, 403

Bensby, T., Feltzing, S., Lundström, I. 2003, A&A, 410, 527

Bensby, T., Feltzing, S., Lundström, I., Ilyin, I. 2005, A&A, 433, 185

Bergeron P., Wesemael F., Beauchamp A., 1995, PASP, 107, 1047

Bertelli G., Bressan A., Chiosi C., Vallenari A., 1999, Balt. Astr. 8, 271

Bertelli G., Nasi E., 2001, AJ, 121, 1013

Bertelli, G., Nasi, E., Girardi, L., Chiosi, C., Zoccali, M.; Gallart, C., 2003, ApJ 125, 770

Bertero, M., Boccacci, P. 2005, A&A, 437, 369

Binney, J. J., Dehnen, W., Bertelli, G. 2000, MNRAS, 318, 658

Bressan A., Fagotto F., Bertelli G., Chiosi C., 1993 A&AS 100,647

Brocato, E., Castellani, V., Di Carlo, E., Raimondo, G., Walker, A. R. 2003, AJ, 125, 3111

Cariulo, P., Degl'Innocenti, S., Castellani, V. 2004, A&A, 421, 1121

Carraro, G., Chiosi, C. 1994, A&A, 287, 761

Casertano, S., Ratnatunga, K. U., Bahcall, J. N. 1990, ApJ, 357, 435

Castellani V., Degl'Innocenti S. Marconi M. 1999a, MNRAS 303, 265

Castellani, V., Chieffi, A., Pulone, L., Tornambé, A. 1985, ApJ, 296, 204

Castellani V., Degl'Innocenti S. Marconi M. 1999b, A&A 349, 834

Castellani V., Degl'Innocenti S., Girardi L., Marconi M., Prada Moroni P.G., Weiss A., 2000, A&A, 354, 350

Castellani V., Degl'Innocenti S. Prada Moroni P.G. 2001, MNRAS 320, 66

Castellani V., Degl'Innocenti S., Prada Moroni P.G., Tordiglione V. 2002, MNRAS 334, 193

Castellani V., Degl'Innocenti S., Marconi M., Prada Moroni P.G., Sestito P., 2003,A&A 404,645

Chaboyer, B., Demarque, P., Kernan, P. J., Krauss, L. M. 1998, ApJ, 494, 96

Chen, B. 1997, ApJ, 491, 181

Chen, L., Hou, J. L., Wang, J. J. 2003, AJ 125, 1397

Chiappini, C., Matteucci, F., Padoan, P. 2000, ApJ, 528, 711

Chiba, M., Beers, T. C. 2000, AJ, 119, 2843

Chiosi, C., Bertelli, G., Meylan, G., Ortolani, S. 1989, A&A, 219, 167

Chiosi, C., Bertelli, G., Bressan, A., 1992, ARA&A, 30, 305

Cyburt, R. H., 2003, Phys. Lett. B, 567, 227

Degl'Innocenti S., Dziembowski W.A, Fiorentini G., Ricci B. 1997, Astrop. Phys. 7, 77

Degl'Innocenti S., Prada Moroni P.G., Ricci B. 2005, Astrophysics and Space Science, submitted

Dehnen W., Binney J. J., 1998, MNRAS, 298, 387

Du, C., Zhou, X., Ma, J., et al., 2003, A&A, 407, 541

Edvardsson B., Andersen J., Gustafsson B., Lambert D.L., Nissen P.E., Tomkin J., 1993, A&A, 275, 101

Eggleton, P.P., 1973, MNRAS, 163, 279

Elmegreen, B. G. 1993, ApJ, 419, L29

Elmegreen, B. G., Efremov, Y. N. 1997, ApJ, 480, 235

Feltzing S, Bensby T, Lunstrom I, 2003, A&A, 397, 1

Feltzing, S., Gonzales, G. 2001, A&A, 367, 251

Feltzing, S., Gilmore, G. 2000, A&A, 355, 949

Fontaine, G., Brassard, P., Bergeron, P. 2001, PASP, 113, 409

Fuhrmann, K. 1998, A&A, 338, 161

Fuhrmann, K. 2004, Astron. Nachr., 325, 3

Gallart, C., Freedman, W., Aparicio, A., Bertelli, G., Chiosi, C. 1999, AJ, 118, 2245

Gilmore, G., Reid, N. 1983, MNRAS, 202, 1025

Gilmore, G., Wyse, R. F. G., Kuijken, K. 1989, ARA&A, 27, 555

Girardi, L., Bressan, A., Chiosi, C., Bertelli, G., Nasi, E., 1996, A&A, 117, 113

Girardi, L., Bressan, A., Bertelli, G., Chiosi, C., 2000, A&AS 141, 371

Gnedin, O. Y., Ostriker, J. P. 1997, ApJ, 474, 223

Greene, William C., Econometric Analysis, 2003, 5th Edition. New York: Prentice Hall

Grevesse N., Sauval A. J., 1998, Space Science Reviews, 85, 161

Grevesse N., Noels A., 1993 in “Origin and Evolution of the elements”, ed. N. Prantzos, E. Vangioni-Flam, M. Casse(̀Cambridge Univ. Press, Cambridge), p.15

Henry, T. D., McCarthy, D. W. 1993, AJ, 106, 773

Hansen, B. M. S., Brewer, J., Fahlman, G. G., et al. 2002, ApJ, 574, L155

Hartwick, F. D. A. 1976, ApJ, 209, 418

Hernandez, X., Valls-Gabaud, D., Gilmore, G. 2000, MNRAS, 316, 605

Herrera, L., Santos, N., O., 1995, AJ 438, 308

Høg, E., et al. 2000, A&A, 357, 367

Hurley J., Tout C. A., 1998, MNRAS, 300, 977

Ibata R.A., Gilmore G., Irwin M.J., 1994, Nature, 370, 194

Kippenhahn, R., Weigert A. 1990, Stellar Structure and Evolution (Berlin: Springer)

Kroupa, P. 2001, in ASP Conf. Ser. 228, “Dynamics of Star Clusters and the Milky Way”, ed. S. Deiters, B. Fuchs, R. Spurzem, A. Just, R. Wielen (San Francisco: ASP), 187 (a)

Kroupa, P. 2001, MNRAS, 322, 231 (b)

Kroupa, P., Tout, C. A., Gilmore, G. 1993, MNRAS, 262, 545

Jahreiss, H., Wielen, R. 1997, in Hipparcos 1997: Presentation of the Hipparcos and Tycho Catalogues and First Astrophysical Results of the Hipparcos Space Astrometry Mission, ed. B. Battrick, M. A. C. Perryman, & P. L. Bernacca (ESA SP-402; Noordwijk: ESA), 675

Kennicutt, R. C. 1990, in “Paired and interacting galaxies”, IAU Colloquium 124, eds. J. W. Sulentic, W. C. Keel, & C. M. Telesco (NASA), 269

Larson, R. B. 1981, MNRAS, 194, 809

Larsen, J. A., Humphreys, R. A. 2003, AJ, 125, 1958

Larson, R. B. 1992, MNRAS, 256, 641

Leggett, S. K., Ruiz, M. T., Bergeron, P. 1998, ApJ, 497, 294

Lindegren L., 1995, A&A, 304, 61

Liu, W. H., Chaboyer, B. 2000, ApJ, 544, 818

Lucy, L. B. 1974, AJ, 79, 745

Lucy, L. B. 1994, A&A, 289, 983

Lutz, T. E., Kelker, D. H. 1973, PASP, 85, 573

Malmquist, K.G., 1920, Medd. Lund Astron. Obs., Ser. 2, No. 22

Martinelli, A., Matteucci, F. 2000, A&A, 353, 269

Mazeh, T., Simon, M., Prato, L., Markus, B., Zucker, S. 2003, ApJ, 599, 1344

Meusinger, H., Reimann, H.G., Stecklum, B. 1991, A&A, 245, 57

Mowlavi, N., Meynet, G., Maeder, A., Schaerer, D., Charbonnel, C. 1998, A&A, 335, 573

Nelder, J. A. and Mead, R. 1965, Comput. J., 7, 308-313

Nordström, B., Mayor, M., Andersen J., Holmberg, J., Pont, F., Jorgensen, B. R., Olsen, E. H., Udry, S., Mowlavi, N. 2004, A&A, 418, 989

Ng, Y.K., Bertelli, G., Chiosi, C., Bressan, A. 1997, A&A, 324, 65

Norris, J. 1986, ApJS, 61, 667

Norris, J., Green, E. M. 1989, ApJ, 337, 272

Norris, J., Ryan, S. G. 1991, ApJ, 380, 403

Olive K. A., Skillman E. D., 2004, ApJ, 617, 29

Pace, G., Pasquini, L. 2004, A&A, 426, 1021

Pagel B.E.J., Portinari L. 1998, MNRAS 298, 747

Perryman, M. A. C. et al. 1995, A&A, 304, 69

Piatti, A. E., Claria, J. J., Abadi, M. G. 1995, AJ, 110, 2813

Pilyugin, L. S., Edmunds, M. G. 1996, A&A, 313, 783

Pols O.R., Schröeder K-P, Hurley J.R., Tout C.A., Eggleton P.P., 1998, MNRAS 298, 525

Pont, F., Eyer, L. 2004, MNRAS, 351, 487

Quillen, A. C., Garnett, D. R. 2001, ASP-CS, 230, 87

Quinn P. J., Hernquist L., Fullagar D. P. 1993, ApJ, 403, 74

Raha, N., Sellwood, J. A., James, R. A., Kahn, F. D. 1991, Nature, 352, 411

Reid, I.N., Majewski S.R. 1993, ApJ, 409, 635

Richardson, W. H. 1972, JOSA., 62, 55

Robin, A. C., Haywood, M., Créze, M., Ojha, D. K., Bienaymé, O. 1996, A&A, 305, 125

Robin, A. C., Reylé, C., Crézé, M. 2000, A&A, 359, 103

Rocha-Pinto, H. J., Maciel, W. J., Scalo, J., Flynn, C. 2000, A&A, 358, 850

Ryan, S. G., Norris, J. E. 1991, AJ, 101, 1835

Salaris M., Garcia-Berro E., Hernanz M., Isern J., Saumon D., 2000, ApJ, 544, 1036

Salaris M., Girardi L., 2002, MNRAS, 337, 332

Salpeter, E. E. 1955, ApJ, 121, 161

Sandage, A. 1987, AJ, 93, 610

Sandage, A., Lubin, L. M., VandenBerg, D. A. 2003, PASP, 115, 1187

Saumon D., Jacobson S. B., 1999, ApJ, 511, L107

Scalo, J.M. 1986, "Luminous stars and associations in galaxies", IAU Symp. no. 116, p. 451, ed. de Loore, C.W.H., Willis,A.J. & Laskarides, P., Reidel, Dordrecht, Holland.

Schmidt, M. 1959, ApJ 129, 243

Schmidt, M. 1963, ApJ 137, 758

Schröder, K. P., Pagel, B. E. J. 2003, MNRAS, 343, 1231

Searle, L., Zinn, R. 1978, ApJ, 225, 357

Siegel, M. H., Majewski, S. R., Reid, I. N., Thompson, I. B. 2002, ApJ, 578, 151

Sommer-Larsen, J., Zhen, C. 1990, MNRAS, 242, 10

Soubiran, C., Bienaymé, O., Siebert, A. 2003, A&A, 398, 141

Soubiran, C., Girard, P. 2005, A&A, 438, 139

Spagna, A. et al. 1996, A&A, 311, 758

Spitzer, L. J., Schwarzschild, M. 1951, ApJ, 114, 385

Strömgren, B. 1966, ARA&A, 4, 433

Thoul A., Bahcall J., Loeb A. 1994, ApJ 421, 828

Tinsley, B. M. 1975, ApJ, 197, 159

Tolstoy E., Saha A., 1996, ApJ, 462, 672

Twarog, B.A. 1980, ApJ, 242, 242

Vallenari, A., Bertelli, G., Schmidtobreick, L. 2000, A&A, 361, 73

Van den Bergh, S. 1962, AJ, 67, 486

Van den Hoek L. B., de Jong T., 1997, A&A, 318, 231

Vergely J.L., Köppen J., Egret D., Bienaymé O., 2002, A&A, 390, 917

Wakker, B. P. 1991, A&A, 250, 499

Weidemann V., 2000, A&A, 363, 647

Wielen, R. 1977, A&A, 60, 263

Wielen, R., Fuchs, B., Dettbarn, C. 1996, A&A, 314, 438

Wolfire, M.,G., Cassinelli, J. P., 1987, ApJ, 319, 850

Wyse, R. F. G., Gilmore, G. 1995, AJ, 110, 2771

Zheng, Z., Flynn, C., Gould, A., Bahcall, J. N., Salim, S. 2001, ApJ, 555, 393

Zoccali, M., et al. 2003, A&A, 399, 931